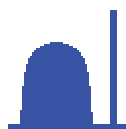


Solidification

Real-Time Investigation of Grain Nucleation and Growth
During Liquid to Solid Phase Transformation of Aluminum Alloys



The research described in this thesis was performed in the section Fundamental Aspects of Materials and Energy of the department Radiation, Radionuclides and Reactors, faculty of Applied Sciences, Delft University of Technology, Mekelweg 15, 2629 JB Delft, The Netherlands



The research described in this thesis was financially supported by the Foundation for Fundamental Research on Matter (FOM).

Solidification

Real-Time Investigation of Grain Nucleation and Growth
During Liquid to Solid Phase Transformation of Aluminum Alloys

PROEFSCHRIFT

ter verkrijging van de graad van doctor
aan de Technische Universiteit Delft,
op gezag van de Rector Magnificus Prof. dr. ir. J. T. Fokkema,
voorzitter van het College voor Promoties
in het openbaar te verdedigen op dinsdag 14 juni 2005 om 13:00 uur

door

Naveed IQBAL

Master of Science in Nuclear Engineering
Quaid-I-Azam University, Islamabad, Pakistan
geboren te Faisalabad, Pakistan

Dit proefschrift is goedgekeurd door de promotor:

Prof. dr. G. J. Kearley

Prof. ir. L. Katgerman

Samenstelling promotiecommissie:

Rector Magnificus	voorzitter
Prof. dr. G. J. Kearley	Technische Universiteit Delft, promotor
Prof. ir. L. Katgerman	Technische Universiteit Delft, promotor
Prof. dr. L. Arnberg	Norges Teknisk Naturvitenskapelige Universitet, Norway
Prof. dr. W. Petry	Technische Universiteit München, Germany
Prof. dr. R. Boom	Technische Universiteit Delft
Prof. dr. I. M. de Schepper	Technische Universiteit Delft
Dr. ir. N. H. van Dijk	Technische Universiteit Delft

Dr.ir. N.H. van Dijk heeft als begeleider in belangrijke mate aan de totstandkoming van het proefschrift bijgedragen.

Published and distributed by: DUP Science

DUP Science is an imprint of
Delft University Press
P.O. Box 98
2600 MG Delft,
The Netherlands
Telephone: +31 15 27 85 678
Telefax: +31 15 27 85 706
E-mail: info@Library.TUdelft.nl

ISBN 90-407-2589-6

Keywords: Solidification, Aluminum, nucleation, neutron scattering, x-ray diffraction

Copyright © 2005 by Naveed Iqbal

All rights reserved. No part of the material protected by this copyright notice may be reproduced or utilized in any form or by any means, electronic or mechanical, including photocopying, recording or by any information storage and retrieval system without written permission from the publisher: Delft University Press.

Printed in the Netherlands

Contents

PART I: Theory, Instruments and Methods

1. Introduction	1
References	7
2. Mechanisms of grain refinement	9
2.1 Nucleation	9
2.1.1 Homogenous nucleation	9
2.1.2 Heterogeneous nucleation	11
2.1.3 Classical nucleation theory	13
2.2 Grain growth	13
2.2.1 Grain growth in Al-Ti alloys	14
2.3 Overall transformation kinetics	15
2.4 Grain refinement models	17
2.4.1 Nucleant effects	17
2.4.2 Phase diagram theories	18
2.4.3 Peritectic hulk theory	19
2.4.4 Hypernucleation theory	19
2.4.5 Duplex nucleation theory	19
2.4.6 Solute effects	20
References	21
3. Experimental	23
3.1 Differential thermal analysis (DTA)	23
3.1.1 Setup	23
3.1.2 Method	24
3.1.3 Fraction transformed	25
3.2 Neutron scattering	26
3.2.1 Experimental neutron diffraction	26
3.2.2 Theory of neutron diffraction	27
3.2.3 Small-angle neutron scattering (SANS)	30
3.3 Three dimensional X-ray diffraction	33
3.3.1 Theory of X-ray diffraction	35
3.3.2 Experimental procedure	36
References	38

PART II: Experimental Results and Discussion

4. Review of experimental results	41
4.1 Aluminum	41
4.2 Solidification	41
4.2.1 General concept of nucleation	41
4.2.2 Grain refinement during aluminum solidification	44
4.2.3 Paradigms of grain refinement	44
4.3 Experiments and results in this thesis	45

References	49
5. DTA measurements on aluminum alloys for the investigation of the crystallization kinetics during grain refinement	51
5.1 Introduction	51
5.2 Sample preparation	52
5.3 Experimental method	52
5.4 Results and discussion	53
5.4.1 Crystallization behaviour	53
5.4.2 Melting behaviour	59
5.5 Conclusions	63
References	63
6. Solidification of aluminum alloys studied by neutron scattering	65
6.1 Experimental study of ordering kinetics in aluminum alloys during solidification	65
6.1.1 Introduction	65
6.1.2 Experimental	66
6.1.3 Results and discussion	67
6.1.3.1 Liquid structure factor	67
6.1.3.2 Liquid volume fraction	68
6.1.3.3 Transformation kinetics	71
6.1.3.4 Growth oscillations	73
6.1.4 Conclusions	74
References	75
6.2 Periodic structural fluctuations during the solidification of aluminum alloys studied by neutron diffraction	76
6.2.1 Introduction	76
6.2.2 Experimental	77
6.2.3 Results	78
6.2.3.1 Structure	78
6.2.3.2 Solidification kinetics	79
6.2.4 Discussion	81
6.2.5 Conclusions	88
References	89
6.3 The role of solute titanium and TiB ₂ particles in the liquid-solid phase transformation of aluminum alloys	90
6.3.1 Introduction	90
6.3.2 Materials and method	91
6.3.2.1 Sample preparation	91
6.3.2.2 Experimental method	91
6.3.3 Results and discussion	92
6.3.3.1 Liquid structure factor	92
6.3.3.2 Liquid volume fraction	92
6.3.3.3 Transformation kinetics	96
6.3.3.4 Intensity fluctuations	98
6.3.4 Conclusions	100
References	101
6.4 SANS investigations on the solidification of aluminum alloys	102
6.4.1 Introduction	102

6.4.2	Experimental	102
6.4.3	Results and discussion	103
	References	106
7.	Three dimensional X-ray diffraction for grain nucleation and growth	107
7.1	Microscopic view on grain nucleation and growth kinetics during solidification of aluminum alloys	107
7.1.2	Introduction	107
7.1.3	Experimental	108
7.1.4	Results and discussion	110
	7.1.4.1 Nucleation rate	110
	7.1.4.2 Grain growth	111
7.1.5	Conclusions	112
	References	113
7.2	Evolution of metastable TiAl_3 phase	114
7.3	Real-time observation of grain nucleation and growth during solidification of aluminum alloys.	115
7.3.1	Introduction	115
7.3.2	Experimental	116
	7.3.2.1 Sample preparation	116
	7.3.2.2 Experimental procedure	116
7.3.3	Results and discussion	117
	7.3.3.1 X-ray diffraction patterns	117
	7.3.3.2 Grain nucleation	118
	7.3.3.3 Grain growth	120
	7.3.3.4 Metastable TiAl_3	122
7.3.4	Conclusions	122
	References	123
7.4	Nucleation and grain growth versus cooling rate	124
	Summary	129
	Samenvatting	131
	Acknowledgements	135
	Curriculum Vitae	137
	List of publications	139

PART I

Theory, Instruments and Methods

Chapter 1

Introduction

Aluminum is widely used throughout the world economy, particularly in the transportation, packaging, and construction industries. As a lightweight, resistant to corrosion, high-strength, and recyclable structural metal, aluminum has and will continue to play an important role as applications extend to infrastructure, aerospace, and other High-Tec industries. The challenge for the aluminum industry is to improve the material properties so as to meet the growing needs for stronger and lighter materials. For instance, the auto industry is under pressure to reduce environmentally harmful emissions and improve gas mileage. Aluminum represents the best solution for developing lighter, stronger, and more fuel-efficient vehicles.

A statistical review of aluminum consumption by the leading aluminum consumers during the last decade (1992-2002) is presented in table 1.1 [1]. The "aluminum supply" comes from three basic sources: primary (domestic production from alumina); imports of ingot and semifabricated (mill) products; and recycled metal (from scrap, also known as secondary recovery). Subtracting a country's exports of ingot and mill products from its aluminum supply yields its "apparent aluminum consumption." Reflecting the worldwide trend toward greater use of aluminum, the change in world's primary aluminum production during the last decade is shown in figure 1.1 [1]. The statistics indicate that the worldwide primary aluminum production, over the period, increased at an annual rate of 2.9 percent—reaching 25.9 million metric tons in 2002. Other than North America, all of the aluminum-producing regions of the world Africa, Latin America, Asia, European Union, Other Europe, and Oceania, experienced at least modest average annual growth rates during the period.

Aluminum, when in the pure form, is generally polycrystalline with a large grain size of more than 1 mm, exhibiting poor mechanical strength, which is an important aspect of the performance in industrial applications. Strengthening of metals can be obtained in several ways, for example by solid solution hardening, work hardening, precipitation hardening or grain refinement. Grain refinement is technologically attractive because it generally does not adversely affect ductility and toughness, contrary to most other strengthening methods. The yield stress σ_y generally increases for a decreasing average grain size d , according to the Hall-Petch equation [2];

$$\sigma_y = \sigma_o + k/\sqrt{d} \quad (1.1)$$

Table 1.1: Statistical review of aluminum consumption by different countries during the last decade (1992-2002) [1]. All the quantities are in thousands of metric tons.

Aluminum consumption (Thousands of Metric Tons)

Country	1992	2002
United States	6952	8453
China	n/a	4288
Japan	3619	3561
Germany	2044	2493
Italy	1132	1645
France	989	1363
Canada	600	885
United Kingdom	800	868
Brazil	326	717
India	383	642
Netherlands	261	405

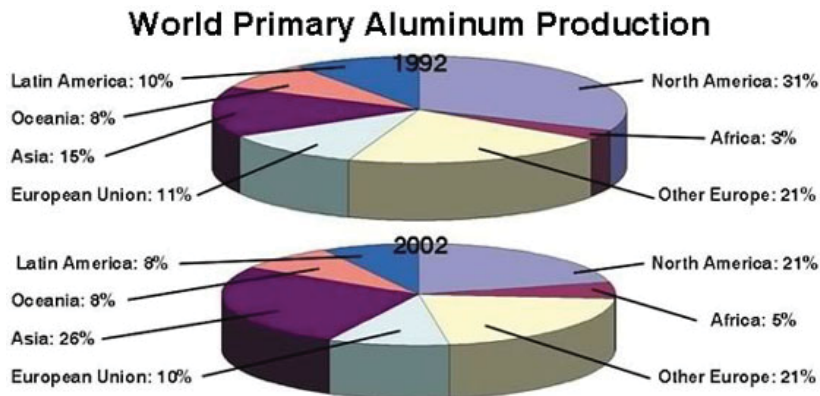


Figure 1.1: The statistical review of worldwide primary aluminum production over the last decade (1992-2002) [1].

Metals obey the Hall-Petch equation over several orders of magnitude in grain size. The average grain size changes with material and processing conditions and is estimated to be 200 μm for grain refined aluminum [3]. Figure 1.2 shows the microscopic grain structure of pure solid aluminum and a grained refined aluminum alloy. Note the drastic reduction in grain size and change in grain morphology, from columnar structure to equiaxed grains, after the addition of grain refiners.

Grain refinement is directly related to the nucleation and growth of aluminum grains during solidification. The nucleation process involves the ordering of groups of atoms in the liquid to form very small solid clusters. These fluctuations occur at temperatures both above and below the melting point T_m , but clusters formed above T_m always revert to the liquid since it is the most stable phase. However clusters formed below the melting temperature T_m can evolve to solid nuclei provided their size is sufficiently large to be stable against melting. Thermodynamically, the barrier for a nucleation event is associated to the relatively large surface energy of the solid-liquid interface with respect to the gain in energy between the solid and the liquid phase for a small cluster. This energy barrier for nucleation is of the order of

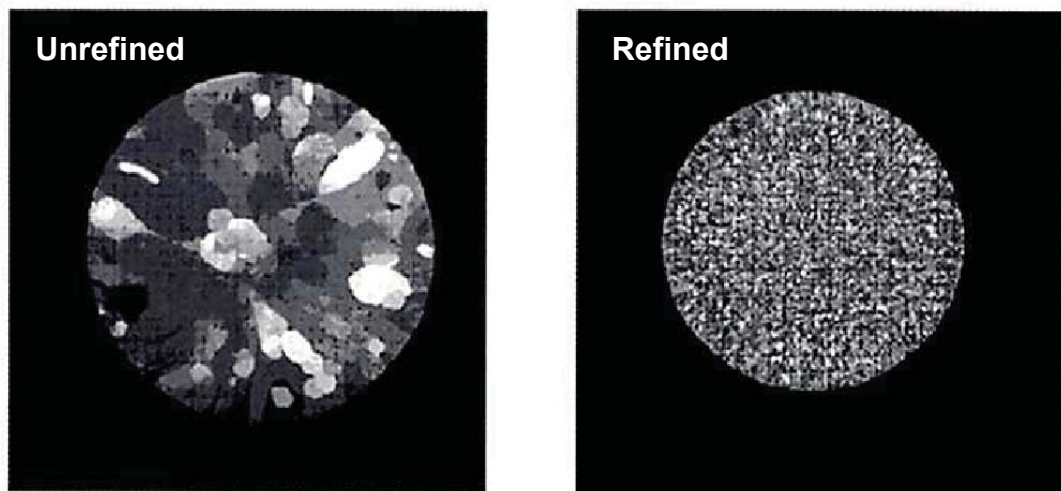


Figure 1.2: Grain structure of aluminum without and with grain refinement during solidification.

$0.2 k_B T_m$ for homogenous nucleation in pure metals [4]. The addition of foreign substrates in the melt provides nucleation sites with a reduced energy barrier for nucleation that enhances the nucleation rate. This process is known as heterogeneous nucleation. The stable nuclei formed on the foreign substrates then grow in size resulting into an equiaxed and finer grain structure. Figure 1.3 illustrates the mechanism of homogenous nucleation in pure aluminum and heterogeneous nucleation on a foreign substrate.

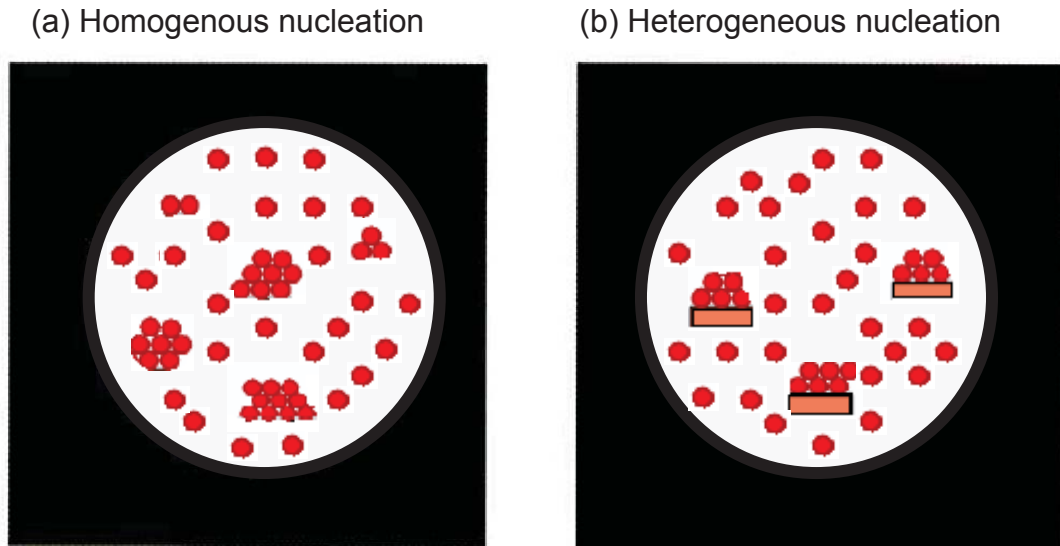


Figure 1.3: A schematic representation of (a) homogenous nucleation and (b) heterogeneous nucleation on foreign substrate during the liquid to solid phase transformation.

The use of grain refinement is widespread in the aluminum industry and is commonly achieved through the addition of small amounts of Al-Ti-B or Al-Ti-C master alloys [3, 5-7]. These alloys contain microscopic TiB_2 , TiAl_3 and TiC particles which can act as substrates for heterogeneous nucleation of aluminum grains during solidification. The Al-Ti-B master alloys are most commonly used as they are easier to prepare [8] by the reaction of Ti and B-containing salts with molten aluminum primarily due to higher solubility of boron in molten aluminum and high stability and low solubility in molten aluminum of resulting TiB_2 particles. The carbon has low solubility in aluminum while the stability of TiC particles at low concentration of titanium in aluminum is also an issue. In this thesis grain refinement by Al-Ti-B master alloys is studied. The major issue in grain refinement of Al-Ti-B alloys is the role of TiB_2 and TiAl_3 particles during solidification. Numerous studies [9] have established that there are favourable epitaxial relationships between solid aluminum and the surface of TiAl_3 particles. For example, the $\{110\}$ planes of TiAl_3 match well with the $\{112\}$ planes of solid aluminum. The lattice discrepancy between the two planes is less than two percent [3]. This means that the $\{110\}$ planes of the titanium aluminide crystal seem almost like a piece of solid aluminum and so grain can nucleate very easily there. This epitaxial relationship makes the TiAl_3 surface a better nucleation site compared to that of TiB_2 . However the stability of TiAl_3 particles in an aluminum alloy strongly depends on the concentration of solute titanium in the melt. During the production of aluminum alloys, the master alloy is added at levels, which result in solute titanium concentration below the peritectic composition (0.15 wt.% Ti). For these hypoperitectic aluminum compositions, TiAl_3 is not a stable phase [3] and apparently TiB_2 are the only nucleation sites available in the melt during solidification. Microscopic observations [10,11] for the grain refinement of pure aluminum in the presence of TiB_2 particles have however shown that the TiB_2 particles without solute titanium are poor nucleants for aluminum grains during solidification. Hence the question arises “how does the small amount of solute titanium enhances the nucleation on TiB_2 particles and improve the grain refinement process?” Figure 1.4 shows the variation in grain size of solidified aluminum for

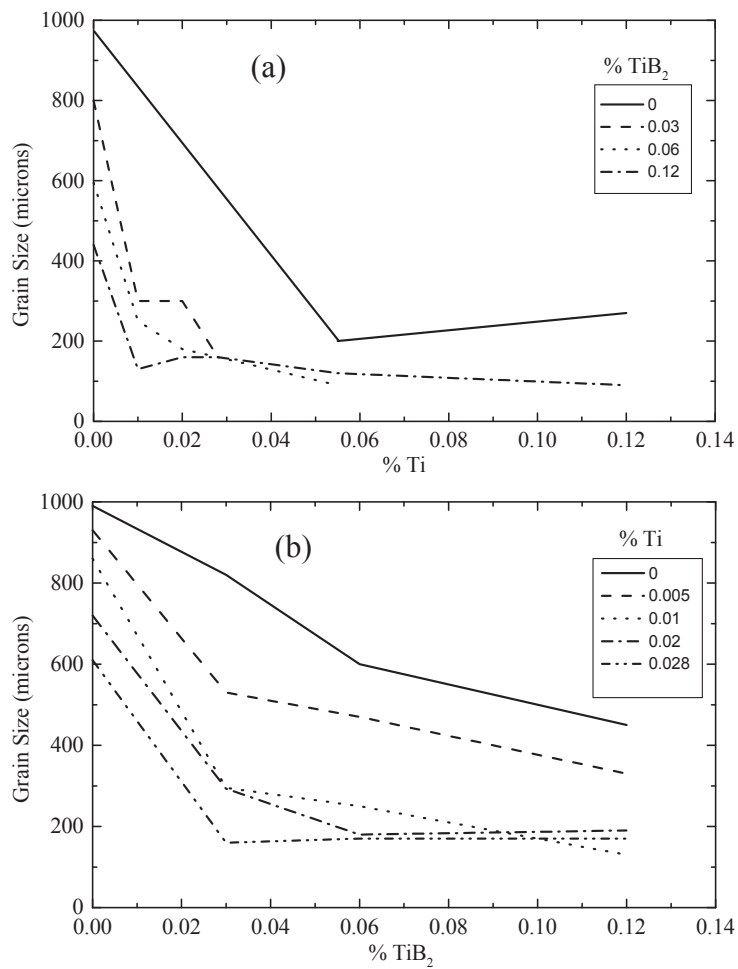


Figure 1.4: The variation in grain size of solidified aluminum for the addition of TiB₂ particles and solute Ti. (a) The effect of additional solute titanium at various TiB₂ concentrations. The insert shows the addition levels of TiB₂ (wt.%). (b) The effect of additional TiB₂ at various solute titanium concentrations. The insert shows the levels of added solute Ti (wt.%). The graphs are based on data from ref. [5].

different concentrations of TiB_2 particles and the solute titanium independently and both together. The grain size reduces significantly when solute titanium is added in the aluminum melt containing TiB_2 particles.

In order to obtain a complete understanding of the mechanism of grain refinement, detailed experimental observations of the evolving microstructure during solidification are crucial. Generally calorimetric techniques such as differential thermal analysis (DTA) probe the heat produced during solidification, which is a measure of the phase fraction transformed. This technique only provides information about the overall transformation, but does not help to give an independent determination of grain nucleation and growth. Since liquid and solid phases have different local structure, promising experimental techniques that can exploit this information to monitor the structure during solidification are neutron diffraction and synchrotron radiation. These types of radiation have the ability to penetrate several millimetres of aluminum and at the same time provide real-time information on the evolving microstructure during solidification at high temperature. For synchrotron radiation hard X-rays are needed to penetrate the bulk of the sample.

Time resolved neutron diffraction measurements during solidification of aluminum alloys provide instantaneous information about the evolution of liquid/solid fraction and the crystallization kinetics of evolving grains.

The only technique that can independently determine the nucleation rate, the growth rate of individual grains and the fraction transformed during solidification is the three dimensional X-ray diffraction technique [12]. This technique has successfully been applied for the determination of the nucleation and growth rate of individual grains during solid-state transformation in aluminum [13] and steel [14].

The research presented in this thesis aims to experimentally investigate the crystallization process during solidification of grain refined aluminum alloys and to compare these results with the physical models that describe grain nucleation and grain growth during the transformation. The investigated samples include high purity aluminum containing TiB_2 nucleating particles and solute titanium separately and both together so as to independently establish the role played by them during the grain refinement process. These alloys serve as model systems for studying the mechanism of grain nucleation and growth during the liquid to solid phase transformation. The results obtained are compared with another commercial purity grain refined aluminum alloy.

Chapter 2 reviews the theories that form the basis of the grain refinement mechanism and the physical models that explain the transformation kinetics during solidification.

The experimental techniques applied in this study are described in chapter 3. These experimental techniques involve differential thermal analysis (DTA), neutron diffraction, small angle neutron scattering and three-dimensional X-ray diffraction microscopy.

Chapter 4 presents a brief overview of the problem investigated in this thesis. It also reviews the analysis and conclusions of our experiments, which are described in detail in the upcoming chapters.

The results of differential thermal analysis (DTA) experiments, describing the over all transformation kinetics of aluminum alloys during solidification, are given in chapter 5.

In chapter 6 the experimental findings of in-situ neutron diffraction and small angle neutron scattering measurements during the crystallization of aluminum alloys are presented.

Chapter 7 presents the nucleation kinetics and the growth behaviour of individual grains during solidification, measured with the three-dimensional X-ray diffraction technique.

The thesis is finally summarised in the end.

References

- [1] The aluminum association, Inc., *Aluminum Now*, Vol. 6, No. 3, 2004.
- [2] Hall, J. P. and Petch, Z. Z., *Can. J. Metallurgy*, 26 (1954) 254.
- [3] Easton, M. and Stjohn, D. *Met. Mater. Trans.* 1999, A30, 1613.
- [4] Cottrell, A., In: *An Introduction to Metallurgy*, London, Edward Arnold (Publishers) Ltd. 1985.
- [5] Easton, M. and Stjohn, D. *Met. Mater. Trans.* 1999, A30, 1625.
- [6] McCartney, D. G., *Int. Mater. Rev.*, 1989, 34, 247.
- [7] Schumacher, P., Greer, A. L., Worth, J., Evans, P. V., Kearns, M. A., Fisher, P. and Green, A. H., *Mater. Sci. and Tech.*, 1998, 14, 394.
- [8] Sigworth, G. K., *Met. Trans. A*, 15 (1984) 277.
- [9] Guzowski, M. M., Sigworth, G. K. and Sentener, D. A., *Met. Trans. A*, 18 (1987) 603.
- [10] Mohanty, P. S. and Gruzleski, J. E. *Acta Metall. Mater.*, 1995, 43, 2001.
- [11] Mohanty, P. S., Samuel, F. H. and Gruzleski, J. E., *Metall. Mater. Trans. B* 1995, 26B, 103.
- [12] Poulsen, H. F., *Three Dimensional X-Ray Diffraction Microscopy, Mapping Polycrystals and Their Dynamics*, Springer Tracts in Modern Physics, Vol. 2005.
- [13] Lauridsen, E. M., Jensen, D. J. And Poulsen, H. F., *Scripta Mater.* 2000, 43, 561.
- [14] Offerman, S. E., van Dijk, N. H., Sietsma, J., Grigull, S., Lauridsen, E. M., Marguiles, L., Poulsen, H. F., Rekveld, M. Th. And van der Zwaag, S., *Science*, 2002, 298, 1003.

Chapter 2

Mechanisms of grain refinement

The main objective of this chapter is to review the theoretical concepts of grain nucleation and grain growth, which drive the grain refinement during solidification of aluminum alloys.

2.1 Nucleation

The process of grain refinement begins with the nucleation of the solid phase from the melt during solidification. Nucleation is a kinetic process in which a small number of atoms form a stable cluster, called nucleus, within the liquid phase at the solidification temperature. This nucleus then acts as the first building block for a growing grain. The rate of nucleation is dependent on the magnitude of the undercooling i.e. the difference between the equilibrium melting temperature T_m and the freezing (solidification) temperature T_f . In general a higher undercooling results into an enhanced nucleation rate.

Depending on the absence or presence of a nucleation substrate homogenous and heterogeneous nucleation can be identified.

2.1.1 Homogenous nucleation

According to the classical nucleation theory [1-4], the nucleation of a solid phase does not start immediately if a melt is cooled below the melting temperature. First small clusters of atoms (called embryos) of the solid phase are spontaneously formed in the melt due to thermal fluctuations. The survival of these embryos is governed by two energy differences: (a) the free energy released by the liquid to solid transformation $V\Delta g_v$, where V is the volume of the embryo and Δg_v is the difference in Gibbs free energy per unit volume between the liquid and the solid and (b) the surface energy required to form the new solid-liquid interface $A\gamma_{SL}$, where A is the surface area of the embryo and γ_{SL} is the solid-liquid interface free energy per unit area. If, for simplicity we assume a spherical embryo, then the total free energy change ΔG of an embryo of radius R is given by

$$\Delta G = \frac{4\pi R^3}{3} \Delta g_v + 4\pi R^2 \gamma_{SL}. \quad (2.1)$$

Figure 2.1 shows the variation of the surface free energy, the volume free energy, and the total free energy as a function of the size of the embryo. For an embryo of radius R such that $R < R^*$, a small increase in radius results in an increase of the total free energy. In this case the embryo will dissolve in the liquid.

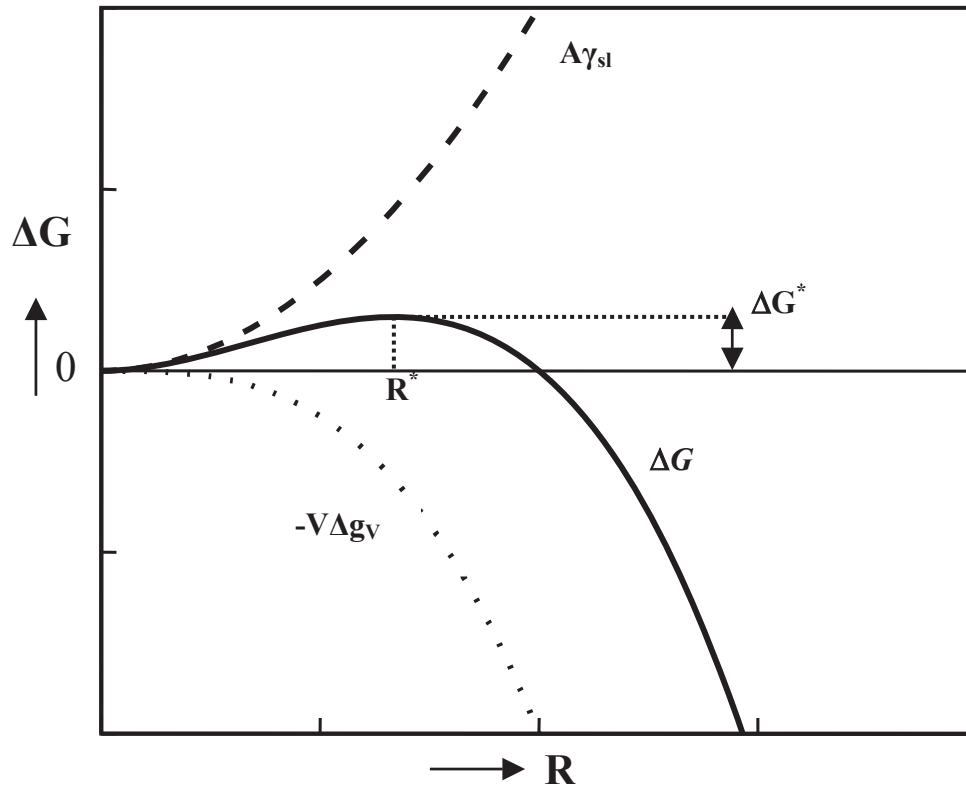


Figure 2.1. The total change in Gibbs free energy ΔG , as a function of the cluster radius R , is the sum of the interfacial energy $A\gamma_{sl}$ and the change in volume energy $V\Delta g_V$. The size of the critical nucleus R^* is determined by the maximum in ΔG , which is the activation energy for nucleation ΔG^* .

The embryo is stable only when its radius is larger than a critical radius R^* , then the growth proceeds spontaneously for $R > R^*$. When the critical radius R^* is reached, the embryo forms a “nucleus”. At the critical radius the total free energy change has a maximum ΔG^* which is known as the work of nucleus formation or the nucleation barrier. Then the critical radius for nucleation is obtained by applying the criterion $(d\Delta G/dR)_{R=R^*} = 0$ given by [4,5]

$$4\pi R^* (R^* \Delta g_V + 2\gamma_{SL}) = 0 \quad (2.2)$$

Then the equation for the critical radius of the nucleus becomes,

$$R_{\text{hom}}^* = \frac{-2\gamma_{SL}}{\Delta g_V}. \quad (2.3)$$

By substituting the value of critical radius of the nucleus R^* from the equation (2.3) into the equation (2.1), one gets the relation for critical energy barrier for the nucleation, given by

$$\Delta G_{\text{hom}}^* = \frac{16\pi}{3} \cdot \frac{\gamma_{sl}^3}{\Delta g_v^2} \quad (2.4)$$

While the free energy per unit volume Δg_v is proportional to undercooling ΔT , such that $\Delta g_v = -\Delta T \Delta s = -(\Delta h_f \Delta T)/T_m$ [5]. Where Δs and Δh_f represent the entropy and the latent heat of fusion per unit volume. Then by substituting the value of Δg_v in equation (2.4), it can be shown that the nucleation barrier is inversely related to undercooling ΔT , and given by

$$\Delta G_{\text{hom}}^* = \frac{16\pi}{3} \left(\frac{T_m^2 \gamma_{sl}^3}{\Delta h_f^2 \Delta T^2} \right) \quad (2.5)$$

At low undercoolings, the nucleation barrier is high and the rate of nucleus formation is low. A greater undercooling promotes the nucleation due to decrease in R^* and ΔG^* . Consider N_n is the number of nuclei per unit volume each of which contain n atoms and N_l represents the number of atoms per unit volume of the liquid. Then According to classical nucleation theory the rate of homogenous nucleation N_n during solidification, such that $N_n \ll N_l$, can be expressed by [5],

$$N_n = A \cdot N_l \exp\left(-\frac{\Delta G^*}{k_B T}\right) \quad (2.6)$$

Where A is a constant, T is the temperature and $k_B = 1.38 \times 10^{-23}$ J/K is the Boltzmann constant. Equation (2.6) shows that due to the exponential dependence a minor change in an undercooling ΔT can result in a change of several orders of magnitude in the nucleation rate.

2.1.2 Heterogeneous nucleation

In practice, homogenous nucleation rarely occurs in pure metals. It can be realized only under very special laboratory conditions (i.e. levitation cooling, high purity materials, etc). Nucleation usually starts on the crucible wall, on the solid nucleants (e.g. TiB_2 , TiAl_3 , or TiC particles in aluminum melt) or on oxide layers in the melt. Nucleation on a foreign substrate is known as heterogeneous nucleation. The nucleation efficiency of a foreign solid substrate depends on the interaction between the solid surface and the melt, called wetting. The wetting is characterized by the wetting angle " θ " as shown in figure (2.2).

For a cap shaped embryo of radius R wetting the substrate with a wetting angle θ , as shown in figure (2.2), by elementary geometry the lateral area, the base area and the volume of the cap is respectively, $2\pi R^2(1-\cos(\theta))$, $\pi R^2 \sin^2(\theta)$ and $(2+\cos(\theta))(1-\cos(\theta))^2 (\pi R^3)/3$. Then the total free energy change for embryo formation, taking into account the net interfacial free energy terms and the volume free energy change, is

$$\Delta G = \frac{4\pi R^3}{3} \Delta g_v \{(1/4)(2+\cos(\theta))(1-\cos(\theta))^2\} + 2\pi R^2(1-\cos(\theta)) \gamma_{sl} + \pi R^2 \sin^2(\theta) (\gamma_{ms} - \gamma_{ml}) \quad (2.7)$$

Where γ_{ms} , γ_{sl} , and γ_{ml} are respectively the interface energies of (substrate) matrix-solid, solid-liquid and matrix-liquid interfaces, as shown in figure (2.2).

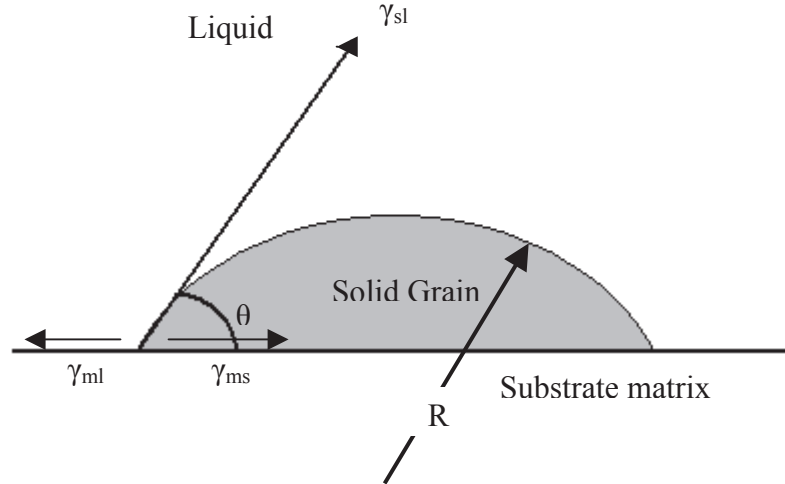


Figure 2.2. Schematic representation showing the formation of a spherical nucleus of solid phase on the surface of a foreign substrate. Where θ is the wetting angle, γ_{sl} is the solid-liquid interface free energy per unit area, γ_{ms} is the interface free energy between growing grain and the foreign substrate matrix and γ_{ml} is the interface free energy between the liquid and the substrate matrix.

Again by applying the criterion for critical radius i.e. $(d\Delta G/dR)_{R=R^*} = 0$ and using the Young equation for the wetting angle θ ,

$$\gamma_{ml} = \gamma_{ms} + \gamma_{sl} \cos(\theta) \quad (2.8)$$

one finds again the relation for critical radius to be $R^* = (-2 \gamma_{sl} / \Delta g_v)$. By substituting equation (2.8) into equation (2.7) and the value of R^* , one obtains

$$\Delta G_{het}^* = \frac{16\pi}{3} \left(\frac{\gamma_{sl}^3}{\Delta g_v^2} \right) \cdot (1/4)(2 + \cos(\theta)(1 - \cos(\theta)))^2 \quad (2.9)$$

The substitution of equation (2.4) into equation (2.9) indicates that the critical energy barrier for heterogeneous nucleation is related to that of the homogenous nucleation, given by,

$$\Delta G_{het}^* = \Delta G_{hom}^* \cdot f(\theta). \quad (2.10)$$

where $f(\theta) = (1/4)(2 + \cos(\theta)(1 - \cos(\theta)))^2$ varies between 0 and 1 depending on the wetting angle. This indicates that the heterogeneous nucleation occurs at a much lower undercooling than the homogenous nucleation. Consequently, heterogeneous nucleation can result in much larger nucleation rate than the homogenous nucleation process.

2.1.3 Classical nucleation theory

The nucleation rate \dot{N} is the number of nuclei formed in a unit volume in a unit time. According to classical nucleation theory, the expression for the time dependent nucleation rate is,

$$\dot{N} = N_o \cdot \beta \cdot Z \exp\left[-\frac{\Delta G^*}{k_B T}\right] \cdot \exp\left[-\frac{\tau}{t}\right] \quad (2.11)$$

where N_o is the density of nucleation sites, β is the frequency factor (the rate at which the atoms are added to the nucleus) and Z is the Zeldovich non-equilibrium factor (which corrects the equilibrium nucleation rate for nuclei that grow beyond the critical size) and τ is the incubation time. The Zeldovich non-equilibrium factor is determined as follows,

$$Z = \sqrt{\frac{-1}{2\pi k_B T} \left(\frac{\partial^2 \Delta G}{\partial n^2} \right)_{n^*}}, \quad (2.12)$$

where n is the number of atoms in a nucleus and n^* is the number of atoms in a critical nucleus.

2.2 Grain growth

Once a grain has nucleated, it is energetically favorable to increase its size. In pure metals the growth rate of the grain is mainly controlled by the removal of the latent heat released due to phase transformation.

For solidification of a multi-component melt like a binary alloy (e.g. Al-Ti alloy etc.), in addition to heat removal, the material transport of solute at the solid-liquid interface also plays an important role. In solidified alloys, the solute is not uniformly distributed. The equilibrium distribution of the solute elements is described by the distribution (or partition) coefficient k_0 ($k_0 = C_{IL}/C_{IS}$). Where C_{IL} and C_{IS} are the equilibrium solute concentration in the liquid and solid at the solid-liquid interface.

Table 2.1. The partition coefficient $k_0 = C_{IL}/C_{IS}$ of various solute elements in aluminum [6].

Element	k_0	Element	k_0
Ti	9	Ta	2.5
V	4.0	Hf	2.4
Mo	2.5	Zr	2.5
Nb	1.5	Si	0.11
Cr	2.0	Ni	0.007
Mg	0.51	Fe	0.02
Cu	0.17	Mn	0.94

During solidification, the solute forms a transition zone, often called boundary layer in the vicinity of the solid-liquid interface. Its width and composition depends not only on temperature but also on the mass transport in the melt (diffusion). In metal alloys the solute partitioning predominantly controls the grain growth during solidification and the final microstructure. The partition coefficient of various solute elements during solidification of aluminum is listed in Table 2.1.

2.2.1 Grain growth in Al-Ti alloys

The grain growth in Al-Ti alloys is governed by the diffusion of solute titanium [7,8] in the aluminum melt. In the case of diffusion-controlled growth, Zener [9] first predicted the parabolic growth for spherical grains. For an Al-Ti alloy, the redistribution (partition) coefficient k_0 of solute titanium in aluminum is significantly greater than one ($k_0 \approx 9$) [3]. As a consequence the solid grain is surrounded by a solute depleted region of increasing width as shown in figure 2.3. This provides the solute undercooling at the front of the aluminum grain, responsible for grain growth. The titanium diffuses into the depleted region and this forms the rate limiting process for the growth rate of the aluminum grains during the phase transformation. During the initial stages of the phase transformation, in which the growth of the individual grain is not limited by the interaction among the neighboring grains, the grain growth is given by the general solution of the diffusion equation, of the form,

$$R(t) = \lambda_s (D_s t)^{1/2} \quad (2.13)$$

where $R(t)$ is the radius of the spherical grain in an isothermal melt at time t , λ_s is the kinetic parameter and $D_s = 5 \mu\text{m}^2/\text{sec}$ [10] is the diffusion coefficient of solute titanium in liquid aluminum, which is assumed to be constant during the phase transformation. Aaron et al. [11] have investigated the kinetic parameters for different approximations applied to diffusion-controlled grain growth. Among these approximations, the invariant-size (stationary-interface) approximation is accepted to be the accurate solution for the diffusion limited grain growth [11, 12]. For a slow grain growth, the invariant size approximation assumes a stationary interface, $(dR/dt) \approx 0$. It restricts the liquid to have no memory of the past motion of the interface. That is the diffusion field around the grain is assumed to be the same as that which would exist if the solid-liquid interface had been fixed from the start and ignores the effect of interface motion on the diffusion. This approximation has been shown to give an accurate result over a widest range of growth rates [11]. For the invariant-size approximation, the kinetic parameter λ_s corresponds to [11],

$$\lambda_s = \frac{-S}{2\pi^{1/2}} + \left(\frac{S^2}{4\pi} - S \right)^{1/2} \quad (2.14)$$

while S is known as the growth parameter which is defined by the titanium solubility in the liquid and the solid phase, as given by,

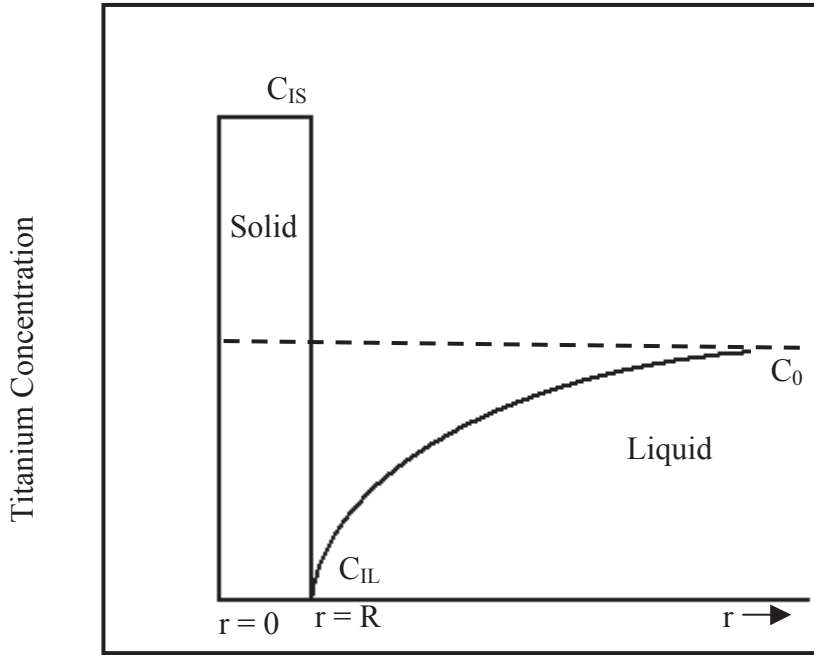


Figure 2.3. Schematic representation of the concentration profile of solute titanium in aluminum during diffusion-controlled grain growth. The solid grain ($r < R$) is surrounded by a titanium-depleted region caused by the partitioning of titanium leading to the diffusion of titanium from the melt into the solid.

$$S = 2 \cdot \frac{(C_{IL} - C_0)}{(C_{IS} - C_{IL})} \quad (2.15)$$

where C_{IL} and C_{IS} are the equilibrium concentration of titanium in the liquid and solid respectively, obtained from the phase diagram. The concentration C_0 is the bulk liquid titanium concentration in the alloy, away from the solid-liquid interface.

2.3 Overall transformation kinetics

The overall transformation is the result of simultaneously occurring grain nucleation and grain growth. The kinetic theory presented by Johnson, Mehl [13] and Avrami [14-16] (JMA) predicts the volume fraction transformed f as a function of time t during an isothermal phase transformation,

$$f(t) = 1 - \exp \left(-c \int_0^t \dot{N}(\tau) \{v(t-\tau)\}^d d\tau \right), \quad (2.16)$$

where $\dot{N}(t)$ is the nucleation rate, c is the geometry factor, v is the growth rate, d is the dimensionality of the growth. For spherical grains $d = 3$ and the corresponding geometry factor is $c = 4\pi/3$.

Within JMA theory, two cases are usually considered; (1) a fixed number of pre-existing nuclei and (2) a constant nucleation rate. For a fixed number of pre-existing nuclei per unit volume N_o , the nucleation rate corresponds to $\dot{N}(t) = N_o \delta(t)$ and equation (2.16) reduces to,

$$f(t) = 1 - \exp(-cN_o(vt)^d). \quad (2.17)$$

For a constant nucleation rate \dot{N}_o the transformed phase fraction is given by,

$$f(t) = 1 - \exp\left(\frac{-c\dot{N}_o v^d t^{d+1}}{d+1}\right). \quad (2.18)$$

The generalized form of the JMA equation can be written as [17]

$$f(t) = 1 - \exp(-kt^n), \quad (2.19)$$

where $k = \ln(2)(t_{1/2})^{-n}$ is a rate constant. The time to transform half of the volume is represented by $t_{1/2}$.

Table 2.2: Summary of the Avrami exponent n found under various transformation conditions.

(I) Polymorphic changes, discontinuous precipitation, eutectoid reactions, interface controlled growth, etc,	
Transformation conditions	n
Increasing nucleation rate	>4
Constant nucleation rate	4
Decreasing nucleation rate	3-4
Zero nucleation rate (saturation of nucleation sites)	3
Grain edge nucleation after saturation	2
Grain boundary nucleation after saturation	1
(II) Diffusion controlled growth	
Transformation conditions	n
All shapes growing from small dimensions, increasing nucleation rate	>2.5
All shapes growing from small dimensions, constant nucleation rate	2.5
All shapes growing from small dimensions, decreasing nucleation rate	1.5-2.5
All shapes growing from small dimensions, zero nucleation rate	1.5
Growth of particles of appreciable initial volume	1-1.5
Needles and plates of finite long dimensions, small in comparison with their separation.	1
Thickening of long cylinders (needles) (e.g. after impingement)	1
Thickening of very large plates (e.g. after complete end impingement)	1/2
Precipitation on dislocations (very early stages)	2/3

The Avrami exponent depends on the characteristics of the phase transformation. A summary of the Avrami exponents found under various transformation conditions is given in table 2.2 [18]. It must be emphasized that this tabulation is no way complete. Additional information (other than just the value of n) is needed in order to uniquely identify the physical processes, that govern a particular transformation. As different transformation conditions may give the same value of n , this shows that the information about the transformation mechanism may not unambiguously be determined from the Avrami exponent.

2.4 Grain refinement models

Grain nucleation and grain growth govern the solidification processing in metals and alloys. The grain nucleation in aluminum alloys can be enhanced by the addition of grain refiners. The most frequently used grain refiners, added to the aluminum melt shortly before solidification, are in the form of Al-Ti-B master alloys. The mechanism of grain refinement caused by the addition of these alloys has been debated over the last 50 years. The Al-Ti-B master alloys contain microscopic TiB_2 and TiAl_3 particles. The surface property of these particles is supposed to facilitate the nucleation of aluminum grains during solidification. This idea is known as nucleant paradigm. However confusion has been caused by number of observations. For instance TiAl_3 is known to be an excellent nucleant for aluminum, but it is unstable at titanium levels lower than 0.15 (wt.%), which is well above the level of addition typically used for grain refinement. On the other hand, TiB_2 is stable at this addition level, but excess titanium is required for effective grain refinement. With these observations the understanding has changed in recent years, emphasizing that the solute elements are vitally important in the grain-refining process. Both the partitioning of solute elements and the added nucleant particles are now thought to affect the grain refinement process. This is known as the solute paradigm.

2.4.1 Nucleant effects in grain refinement

Already in the 1950s, Crossley and Mondolfo [19] proposed the peritectic theory where TiAl_3 particles from a master alloy nucleate solid aluminum through a peritectic reaction ($\text{liquid} + \text{TiAl}_3 \rightarrow \alpha\text{-Al}$), above the melting point of pure aluminum, as shown in figure 2.4. This reaction is believed to be a powerful nucleation mechanism yielding $\alpha\text{-Al}$, when a stable substrate is available for heterogeneous nucleation.

However, when a Al-Ti-B master alloy is added so that titanium is present at hypoperitectic levels (< 0.15 Ti wt.%), often TiB_2 particles are found in the centre of grains, with titanium enriched dendrites growing out of them [20]. This evidence suggests that TiB_2 nucleate $\alpha\text{-Al}$ grains. The borides, however were thought to be poor nucleants or at least not as efficient as TiAl_3 particles [21]. Mohanty et al. [22] have recently confirmed that borides get pushed to the grain boundaries and no grain refinement is observed if no solute titanium is present, which shows that the lattice disregistry between borides and $\alpha\text{-aluminum}$ is large indicating that borides act as a poor nucleant. It is also observed by Maxwell and Hellawell [23] that borides need some undercooling while aluminides need virtually none. In comparison to the borides, TiAl_3 is known to be a powerful refiner. When present at hyperperitectic

concentrations, a dramatic grain refinement was observed [19] and also TiAl_3 was found to be at the center of grains with multiple orientation relationship [24,25] with the aluminum matrix. From this evidence, it can be concluded that TiAl_3 is a better

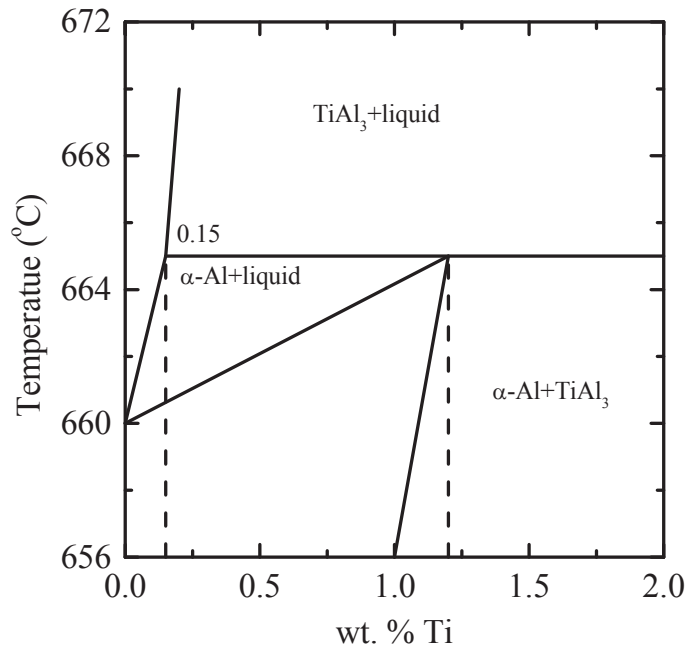


Figure 2.4: Aluminum end of the Al-Ti phase diagram. A concentration of 0.15 Ti (wt.%) corresponds to the peritectic concentration [3].

grain refiner than TiB_2 . This creates an ambiguity about the mechanism responsible for the grain refinement. Thus as an effort to explain the grain refining process, the phase diagram theories were developed.

2.4.2 Phase diagram theories

According to the phase diagram theories, the nucleant particle is taken to be TiAl_3 . The theories propose that boron additions shift the peritectic composition (0.15 wt. % Ti) to a lower levels at about 0.05 wt.% Ti [20,26]. This allows TiAl_3 to be stable at relatively low titanium levels. However, thermo dynamic calculations performed by Jones et al. [27] and Sigworth [28] have found no indications that boron does alter the Al-Ti phase diagram.

Alternatively, it has been argued that TiAl_3 crystals from the master alloy are stable at low titanium levels in the melt. Guzowski et al. [20] showed that the aluminides take about 30 minutes to dissolve at a temperature of 700 °C. This leads to the well known effect known as ‘fade’ where the average grain size increases with holding time of melt during casting.

Currently it is generally accepted that at titanium concentrations below the peritectic composition, TiAl_3 is unstable and do not act as a nucleation site for aluminum grains. As a result there are three main theories that propose how the TiB_2 particles could act to preserve the TiAl_3 phase locally.

2.4.3 Peritectic hulk theory

In the late 1980s and early 1990s, the peritectic hulk theory [29,30] was proposed as an attempt to explain the mechanism of grain refinement. This theory assumes that TiAl_3 is a more powerful nucleant than TiB_2 . To explain how the borides could slow down the dissolution rate of TiAl_3 when Al-Ti-B master alloy is added to the aluminum melt in a hypoperitectic composition, and that the more powerful nucleants remain active longer, it suggests that the borides form a shell around the aluminides. This shell slows down the dissolution of the aluminides as Ti diffusion needs to proceed through the boride shell. The aluminide finally dissolves and leaves a cell of liquid inside the boride shell of approximately the peritectic composition. A peritectic reaction then takes place to form α -aluminum and growth occurs from there. Although this theory seems to fit the experimental results, but there is strong evidence against it by Johnsson et al. [20]. They melted and resolidified a hypoperitectic alloy and found that the grain refinement does not change with the number of cycles. If the peritectic hulk mechanism was occurring, it is expected that the grain refining efficiency would decrease with the number of repetitions, as this would allow diffusion of the titanium out of the hulk and hence the peritectic reaction would cease to occur. Further the peritectic hulk theory suggests that the borides are more soluble than the TiAl_3 as the borides need to dissolve in the melt so that they can precipitate on the more slowly dissolving TiAl_3 . This is however not the case. Borides are very stable in aluminum melts compared to TiAl_3 at hypoperitectic titanium compositions [25,30]. Beside this, it is also expected that, at long holding times, a significant fade would occur, as the titanium level inside and outside the hulk gradually equilibrate. The local high titanium content inside the hulk would then disperse. Therefore, the evidence suggests that the peritectic mechanism is not operating.

2.4.4 Hypernucleation theory

This theory was proposed by Jones [31] and because of the disproportionate effect that very small amounts of titanium and boron make on the average grain size of aluminum. The theory proposes that in the melt solute segregates stably to the melt inoculant interface, and that under the right conditions stable pseudocrystals can form above the principal liquidus of the melt. Immediately below the melt liquidus these pseudocrystals allow α -aluminum to grow without undercooling. The atomic size of the segregant relative to aluminum is the key factor. Competitive segregation of solutes of mismatching size can 'poison' the otherwise hypernucleative processes. The main problem with this theory is that there is no experimental evidence.

2.4.5 Duplex nucleation theory

Of all the mechanisms proposed so far, the most recent theory is the duplex nucleation theory, proposed first by Mohanty et al. [22] and further by Schumacher and Greer [32]. Mohanty et al. added TiB_2 particles to the aluminum melt at various titanium concentrations. It was found that a TiAl_3 layer formed on the TiB_2 particles at hyperperitectic concentrations of Ti and α -aluminum was found on this TiAl_3 layer. But even at hypoperitectic Ti concentrations, there seemed to be a layer in between the TiB_2 and α -aluminum, which they concluded was TiAl_3 .

Schumacher and Greer [32] added Al-Ti-B grain refiner to an aluminum rich metallic glass of composition $\text{Al}_{85}\text{Ni}_5\text{Y}_8\text{Co}_2$ and also found that borides were surrounded by a TiAl_3 layer, which was further surrounded by α -aluminum. There is no strong evidence for this theory and it got a lot of criticism [3].

Schumacher and Greer [33] suggested that an aluminide layer forms on TiB_2 in the melt and grows at holding temperatures of 1300 °C. But there is no theoretical reason for this. They suggest that at a superheat of about 740 °C a stable aluminide layer forms on the surface of TiB_2 particles in the melt. At lower superheats of 370 °C they found a very thin layer of aluminide. The question arises, why would a higher superheat not only preserve a layer of aluminide on the borides but also grow the layer at significant holding times?

Another major problem with the duplex nucleation theory is that Johnsson and Backerud [34] measured the transformation temperatures across the Al-Ti phase diagram for various additions of Al-5Ti-1B (wt.%) master alloy and found that, at hypoperitectic composition, the transformation temperature follows the Al-Ti liquidus curve. Duplex nucleation theory is unable to explain this observation. The liquid adjacent to TiAl_3 phase needs to contain 0.15 Ti (wt.%), which means that the transformation temperature should correspond to the transformation temperature at the peritectic concentration. For an alloy containing 0.05 Ti (wt.%) this would mean a nucleation temperature of about 3 °C higher than the liquidus temperature, which the duplex nucleation theory cannot explain.

2.4.6 Solute effects

By considering only nucleant effects, for the process of grain refinement, no comprehensive and consistent theory has been developed. Therefore it was proposed that both the addition of nucleant particles and the segregation of solute elements (e.g. Ti, Si, etc), play an important role in grain refinement. The segregation power of solute elements in the aluminum melt is quantified by the growth restriction factor $\text{GRF} = mc_0(k_0-1)$, where m is the gradient of the liquidus, c_0 is the concentration of the solute in the alloy and k_0 is the partition coefficient of solute at solid-liquid interface. There are two mechanisms to explain how the solute elements effect the grain refinement. First, the segregating elements (e.g. Ti, Si, etc) act to restrict the growth rate of existing grains in the melt and thereby slow down the transformation process, so that there is more time for nucleation events to occur. Second, the segregating ability of the solute leads to a constitutionally undercooled zone in front of the growing interface with in which nucleation can occur on nucleants, thereby interrupting the growth of previous grains. This mechanism was proposed by Tondel [35] and known as the constitutional undercooling driven mechanism.

In this chapter the physical models to describe the grain nucleation and growth during the liquid to solid phase transformation are described. These models form the basis of the solidification process in aluminum alloys. Efficient nucleating substrates are found to enhance the nucleation of aluminum grains during solidification and subsequently influence the microscopic structure of the solidified material. The review of the existing grain refinement theories for aluminum alloys, shows that the mechanism of grain refinement through heterogeneous nucleation process still remains a matter of controversy. Most of the proposed theories are extrapolations of the results from the ex-situ investigation (metallography, electron microscope, etc.) of grain refined aluminum alloys and very little is known about the kinetics of grain

refinement during solidification. Therefore, in-situ experimental investigations are of great importance to provide detailed information about the evolution of microstructures during the liquid to solid phase transformation.

References:

- [1] M. Volmer and A. Weber, *Z. Phys. Chem.* 119 (1925) 277.
- [2] R. Becker and W. Doring, *Ann. Phys.* 24 (1935) 719.
- [3] J. B. Zeldovich, *Acta. Physicochim, USSR*, 18 (1943) 1.
- [4] H. I. Aaronson and J. K. Lee, in: *Lectures on the Theory of Phase Transformations*, (Met. Soc., New York, 1977).
- [5] W. Kurz and D. J. Fisher, *Fundamentals of Solidification*, (Trans Tech Publications Ltd., Switzerland, 1998).
- [6] M. A. Easton and D. J. StJohn, *Met. Mater. Trans.* A30 (1999) 1613.
- [7] I. Maxwell and A. Hellawell, *Acta Metall.* 23 (1975) 229.
- [8] M. A. Easton and D. J. StJohn, *Mater. Sci. and Tech.* 16 (2000) 993.
- [9] C. Zener, *J. Appl. Phys.* 20 (1949) 950.
- [10] G. S. Ershov, A. A. Kasatkin and A. A. Golubev, *Russian Metallurgy* 2, (1978) 62.
- [11] H. B. Aaron, D. Fainstein and G. R. Kotler, *J. Appl. Phys.* 41 (1970) 4405.
- [12] A. L. Greer, A. M. Bunn, A. Tronche, P. V. Evans and D. J. Bristow, *Acta. Mater.* 48 (2000) 2823.
- [13] W. J. Johnson and R. F. Mehl, *Trans. AIME* 145 (1939) 416.
- [14] M. Avrami, *J. Chem. Phys.* 7 (1939) 1103.
- [15] M. Avrami, *J. Chem. Phys.* 8 (1940) 212.
- [16] M. Avrami, *J. Chem. Phys.* 9 (1941) 177.
- [17] D. A. Porter and K. E. Easterling, *Phase transformations in metals and alloys*, 2nd edition, Cheltenham, Nelson Thornes, 2001.
- [18] J. W. Christian, *The theory of transformation in metals and alloys*, (2nd edition, Pergamon Press, 1975).
- [19] F. A. Crossley, L. F. Mondolfo, *Trans. AIME* 191 (1951) 1143.
- [20] M. Johnsson, *Light Metals* (Warrendale, PA: TMS) (1993) p. 769.
- [21] M. M. Guzowski, G. K. Sigworth, and D. A. Sentner, *Metal. Trans.* A18 (1987) 603.
- [22] P. S. Mohanty and J. E. Gruzleski, *Acta. Metall. Mater.* 43 (1995) 2001.
- [23] I. Maxwell and A. Hellawell, *Metall. Trans.* 3 (1972) 1487.
- [24] I. G. Davies, J. M. Dennis, and A. Hellawell, *Metall. Mater. Trans.* 1 (1970) 275.
- [25] L. Arnberg, L. Backerud, and H. Klang, *Met. Technol.* 9 (1982) 7.
- [26] L. F. Mondolfo and S. Farooq, *Solidification processing* (The Inst. of Metals, London) (1988) p. 133.
- [27] G. P. Jones, and J. pearson, *Metall. Trans.* A24 (1976) 223.
- [28] G. K. Sigworth, *Metall. Trans.*, A22 (1986) 349.
- [29] M. Vader, and J. Noordegraaf, *Light Metals* (Ed.) P. G. Cambell (Warrendale, PA: TMS) (1989) p. 937.
- [30] L. Backerud, P. Gustafson, and M. Jonsson, *Aluminum* 67 (1991) 910.
- [31] G. P. Jones, *Proc. Conf. Solidification processing* (The Inst. of Metals, London, 1988) p. 496.

- [32] P. Schumacher and A. L. Greer, Mater. Sci. and Engg. A, 178 (1994) 309.
- [33] P. Schumacher and A. L. Greer, Mater. Sci. and Engg. A, 181 (1994)1335.
- [34] M. Johnsson and L. Backerud, Z. Metallkd. 87 (1996) 216.
- [35] P. A. Tondel, PhD Thesis, (The University of Trondheim, Trondheim,1994).

Chapter 3

Experimental

In this chapter the theory and practice of differential thermal analysis (DTA), neutron diffraction, small-angle neutron scattering (SANS), and three-dimensional X-ray diffraction (3D-XRD) is presented. Calorimetric techniques such as differential thermal analysis (DTA) are widely used for the determination of the reaction kinetics during isothermal as well as non-isothermal phase transformations. It provides accurate information about the onset of the phase transformation, the time/temperature width of phase transformation, and the transformation energy of the forming phases in multi-component alloys during the phase transformation. However, this technique is limited to small sample volumes and only measures the overall phase transformation. In-situ experimental techniques like neutron diffraction and small-angle neutron scattering (SANS) can probe relatively large sample volumes due to the charge neutrality of neutrons. Neutron diffraction is an ideal probe to investigate the structure of different microscopic phases like liquids and solids simultaneously within the bulk of the sample during solidification. For long wavelength neutrons, small-angle neutron scattering (SANS) can yield information about the size of the grains on length scales ranging from nanometres to micrometers during the phase transformation. The diffraction of hard X-rays produced by a synchrotron source, further provides an excellent probe to investigate the nucleation of individual solid grains and to monitor their growth during the liquid to solid phase transformation.

3.1 Differential thermal analysis (DTA)

3.1.1 Setup

Differential thermal analysis (DTA) is a technique, which measures the temperature difference between the investigated sample and a reference material, as a function of time or temperature, during continuous cooling (or heating). The sample and the reference material are placed symmetrically in a furnace. A schematic diagram of DTA set-up is shown in figure 3.1. Two aluminum oxide (Al_2O_3) cups connected to a thermocouple are placed symmetrically with respect to the furnace. One cup contains the reference material, with the same thermal mass as the sample, which undergoes no transformation in the temperature range of interest. The other cup contains the sample. Both cups contain a small amount of Al_2O_3 powder and are covered with caps to minimize the heat loss due to radiation. The instrument is calibrated for all the applied cooling rates using a high purity zinc and aluminum.

Assuming that the heat transfer between the reference and the cup and between the sample and the cup is instantaneous, the thermocouples measure the sample temperature T_s and the reference temperature T_r . The recorded signal is the temperature difference between sample and reference, $\Delta T = T_s - T_r$, as a function of the reference temperature.

When a sample undergoes a phase transformation, it will either absorb (endothermic process) or release (exothermic process) heat as a function of time or reference temperature. The integrated temperature difference as a function of time is a measure of the amount of heat that is absorbed or released during the phase transformation.

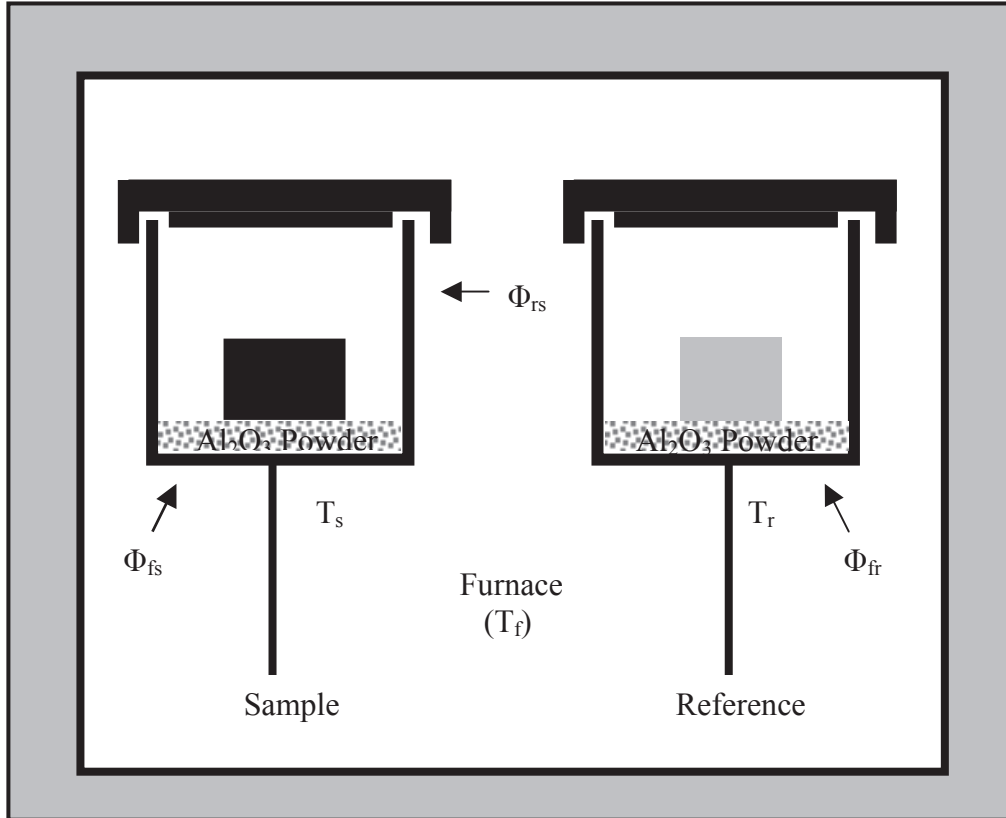


Figure 3.1. Schematic representation of the experimental DTA set-up and the heat fluxes within the furnace.

3.1.2 Method

Figure 3.1 shows the heat fluxes in the DTA experiment assuming that there is no temperature gradient inside the cups. The total heat flux to the sample Φ_s is given by [1]

$$\Phi_s = \Phi_{fs} + \Phi_{rs} = K_{fs}(T_f - T_s) + K_{rs}(T_r - T_s) \quad (3.1)$$

where Φ_{fs} is the heat flux from the furnace to the sample, Φ_{rs} is the heat flux from the reference to the sample, K_{fs} is the heat transfer coefficient between the furnace and the sample, and K_{rs} is the heat transfer coefficient between the reference and the sample. The heat flux to the sample is balanced by the change in temperature and the released/absorbed transformation heat of the sample [2]:

$$\Phi_s = C_{s+c} \frac{dT_s}{dt} + \frac{dH_s}{dt} \quad (3.2)$$

where C_{s+c} is the total heat capacity of the sample and the cup, H_s is the enthalpy of the sample, and t is the time. The same equations can be given for the reference material with the only difference that in the reference material, no transformation takes place. Therefore $(dH_r/dt)=0$, and the total heat flow to the reference Φ_r is given by,

$$\Phi_r = K_{fr} (T_f - T_r) + K_{sr} (T_s - T_r) = C_{r+s} \frac{dT_r}{dt} \quad (3.3)$$

where C_{r+s} is the total heat capacity of reference material and the cup. Assuming that the heat transfer takes place by conduction only and that the holders are identical, it holds that $K_{fs} = K_{fr} = K_1$ and $K_{rs} = K_{sr} = K_2$. Then by combining equations (3.1) to (3.3) and using $-(K_1 + 2 K_2) = K$, $\Delta T_m = T_s - T_r$ and $C_{s+c} = C_s + C_c$, where C_s , C_c is the heat capacity of the sample and the cup, one finds [3];

$$\Delta T_m = \frac{C_s}{K} \frac{dT_s}{dt} + \frac{(C_c - C_r)}{K} \frac{dT_r}{dt} + \frac{C_c}{K} \frac{d\Delta T_m}{dt} + \frac{1}{K} \frac{dH_s}{dt} \quad (3.4)$$

The total temperature difference, ΔT , can be divided into two terms: The temperature difference generated by the sample and the temperature difference due to instrument conditions (furnace, cups etc.). The second term is called base line and can be measured separately, without sample in the sample cup. During this measurement all the conditions are same as that of sample measurement, except (dH_s/dt) is zero, as there is no transformation. Assuming that K_1 and K_2 are independent of the presence of a sample, the temperature difference for the base line, ΔT_{bl} , is given by

$$\Delta T_{bl} = \frac{(C_c - C_r)}{K} \frac{dT_r}{dt} + \frac{C_c}{K} \frac{d\Delta T_{bl}}{dt} \quad (3.5)$$

If the baseline signal ΔT_{bl} (equation (3.5)) is subtracted from the measured ΔT_m (equation (3.4)), the result is the temperature difference generated by the sample only ΔT_{sample} (excluding the effects caused by the sample cup and the system),

$$\Delta T_{sample} = \frac{C_s}{K} \frac{dT_s}{dt} + \frac{C_c}{K} \frac{d\Delta T_m}{dt} - \frac{C_c}{K} \frac{d\Delta T_{bl}}{dt} + \frac{1}{K} \frac{dH_s}{dt} \quad (3.6)$$

Assuming [3] that $C_c \left\{ \frac{d\Delta T_m}{dt} - \frac{d\Delta T_{bl}}{dt} \right\} \ll C_s \frac{dT_s}{dt} + \frac{dH_s}{dt}$, it follows that

$$\Delta T_{sample} = \frac{1}{K} \left\{ C_s \frac{dT_s}{dt} + \frac{dH_s}{dt} \right\} = \frac{1}{K} C_{tot} \frac{dT_s}{dt} \quad (3.7)$$

$$\text{where } C_{tot} = C_s + \frac{dH_s}{dT_s} \quad (3.8)$$

3.1.3 Fraction transformed

The previous two sections describe how to get the temperature dependence of the specific heat for the transformation, C_{tot} . Converting this into the fraction transformed provides insight about the kinetics of the phase transformation. When two phases, solid and liquid, are present in a sample, the total specific heat C_{tot} is the weighted average of the heat capacity of the two phases,

$$C_{tot} = X^l C^l + X^s C^s + \frac{dH_s}{dT} \quad (3.9)$$

Where C^l and C^s be the liquid and solid heat capacity. X^l and X^s represent the liquid and solid fraction for liquid to solid phase transformation during solidification, such that

$$X^l + X^s = 1 \quad (3.10)$$

while dH_s/dT is the additional amount of heat dissipated or generated by the sample during the phase transformation, such that [4]

$$\frac{dH_s}{dT} = \Delta H^{l/s} \frac{dX^s}{dT} \quad (3.11)$$

The term $\Delta H^{l/s}$ is the enthalpy difference between both phases. Rewriting the extended form of equation (3.9) yields,

$$\frac{dX^s}{dT} = \frac{C^l - C^s}{\Delta H^{l/s}} X^s - \frac{C^l - C_{tot}}{\Delta H^{l/s}} \quad (3.12)$$

When C^l and C^s is known, equation (3.12) gives the variation of solid fraction X^s as a function of temperature. The evolution of total solid fraction during solidification is obtained by numerically integrating the equation (3.12).

3.2 Neutron scattering

The neutron is a subatomic particle with zero charge, which makes it an effective probe of bulk samples due to its large penetration power. Thermal neutrons for scattering experiments are usually obtained by slowing down energetic neutrons, produced by nuclear reactors. Most of the neutrons thus produced have the wavelength λ of the order of atomic distances. Neutrons are therefore ideally suited to studies of the atomic structure of condensed matter in diffraction studies [5]. Using a cold source, the average wavelength of the neutrons can be increased by an order of magnitude. These cold neutrons with long wavelength are suitable for small-angle scattering, which can probe relatively large-scale structures in materials.

3.2.1 Experimental neutron diffraction

The neutron diffraction experiments described in this thesis were performed on the diffractometer D20 at the Institut Laue-Langevin (ILL) in Grenoble, France. D20 is a

high intensity 2-axis diffractometer with a flux of the order of 10^7 neutron/cm².s at the sample position. This high neutron flux is sufficient to investigate the liquid to solid phase transformation on a time scale of minutes. A schematic set-up of the diffractometer D20 is shown in figure (3.2). We used a Cu (200) monochromator to select a neutron beam with wavelengths of 0.82 and 0.94 Å. The diffractometer is equipped with a micro-strip detection system that results in a homogeneous response and a very high stability. The detector efficiency during our neutron diffraction experiments was calibrated by a cylindrical vanadium rod. The data collected during measurements was corrected for the scattering by the empty sample container in order to get a accurate value of the measured structure factor.

As liquid aluminum is very corrosive for conventional sample container materials (like e.g. vanadium), single crystal sapphire (Al₂O₃) containers were specially prepared for our neutron diffraction experiments. No reaction between the liquid aluminum and the sapphire was observed, even for long holding times in the liquid state and after many repetitions of the solidification process. The sapphire containers had cylindrical dimensions, with a container height of 60 mm, an inner diameter of 10 mm and a wall thickness of 1 mm. A schematic picture of the sample container is shown in figure (3.3). The single crystal sapphire containers were found to show strong Bragg peaks. However by choosing an appropriate angular orientation of the sample container with respect to the incident beam, it was possible to avoid the presence of Bragg peaks in the angular range of interest. In order to achieve a better temperature stability ($\Delta T < 50$ mK) and reduce the temperature gradients in the sample during solidification experiments, a specially designed furnace insert (figure 3.3), similar to the one used in reference [6], was used. The insert consisted of a nickel block, which was heated symmetrically by cartridge heaters. The furnace insert was placed in a standard ILL radiation furnace that provided bulk heating. The design specifications, the control system and operational details of cooling during the neutron diffraction experiments will be discussed in chapter 5.

3.2.2 Theory of neutron diffraction

The basic equations of the neutron diffraction theory, which are necessary to understand the results of neutron diffraction experiments, are described in this section. Details of the neutron diffraction theory are given elsewhere [7, 8]. Consider a collimated, mono-energetic neutron beam, so that every neutron has the same energy E_0 , wavelength λ_0 and wave-vector $\mathbf{k}_0 = 2\pi/\lambda_0$. Then the differential scattering cross-section of neutrons from a bulk sample that constitutes an ensemble of N atoms, is given by,

$$\left(\frac{d\sigma}{d\Omega} \right) = \left\langle \sum_{i,j}^N b_i b_j e^{-i\mathbf{Q} \cdot (\mathbf{r}_i - \mathbf{r}_j)} \right\rangle \quad (3.13)$$

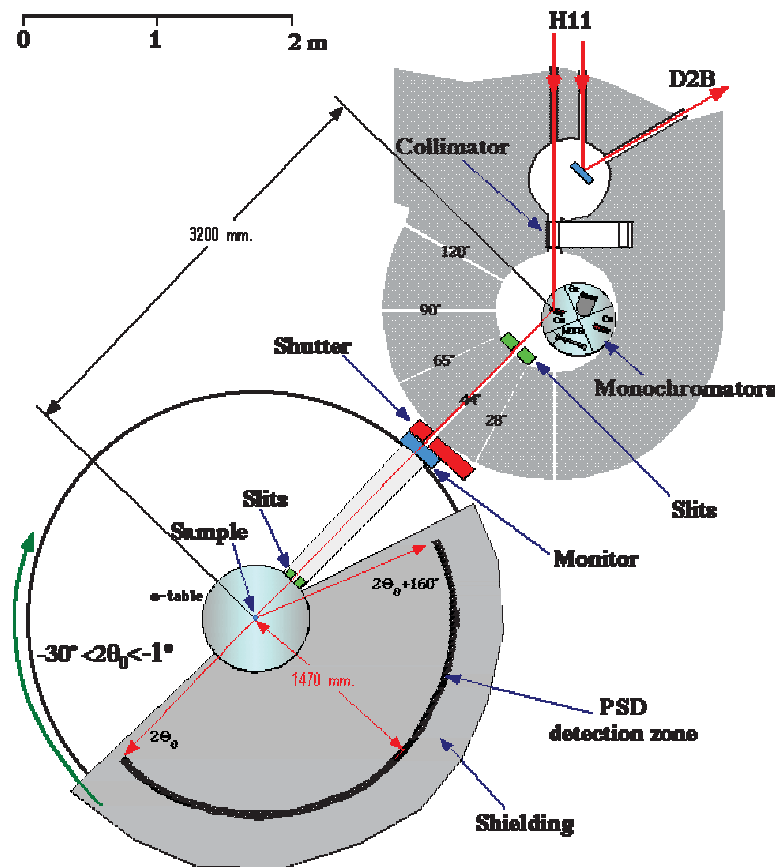


Figure 3.2 Schematic setup of the neutron diffractometer D20 at the Institut Laue-Langevin (ILL) in Grenoble, France.

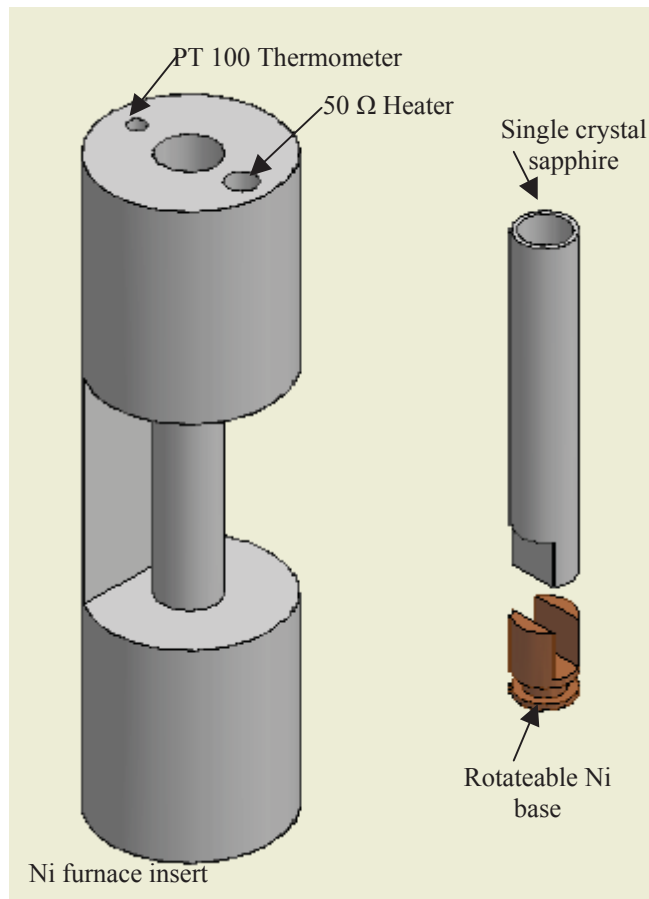


Figure 3.3 Schematic picture of the furnace insert used for the high stability of the sample temperature during the liquid to solid phase transformation.

where b_i represent the scattering length of the atomic nucleus at position \mathbf{r}_i , $\mathbf{Q} = \mathbf{k}_o - \mathbf{k}$ is the wave vector transfer. The absolute value amounts to $|\mathbf{Q}| = Q = 2|\mathbf{k}_o| \sin(\theta) = 4\pi \sin(\theta)/\lambda_o$, where the scattering angle of the neutrons is defined as 2θ . Here the brackets $\langle \dots \rangle$ indicate the ensemble average. For an ensemble of atoms, even chemically identical, the total scattering is the sum of coherent $\sigma_c = 4\pi \langle b \rangle^2$ and incoherent $\sigma_i = 4\pi (\langle b^2 \rangle - \langle b \rangle^2)$ scattering such that

$$\frac{1}{N} \left(\frac{d\sigma}{d\Omega} \right) = \frac{\sigma_c}{4\pi} S(\mathbf{Q}) + \frac{\sigma_i}{4\pi} \quad (3.14)$$

where $S(\mathbf{Q})$ represent the structure factor of ensemble atoms, given by

$$S(\mathbf{Q}) = \frac{1}{N} \left\langle \sum_{i,j} e^{-i\mathbf{Q} \cdot (\mathbf{r}_i - \mathbf{r}_j)} \right\rangle \quad (3.15)$$

The distribution of atoms in real space, with number density ρ_o , can be described by a pair distribution function $g(\mathbf{r})$ such that \mathbf{r} is the distance from the center of an atom,

$$g(\mathbf{r}) - 1 = \frac{1}{(2\pi)^3 \rho_o} \int d\mathbf{Q} (S(\mathbf{Q}) - 1) e^{-i\mathbf{Q} \cdot \mathbf{r}} \quad (3.16)$$

For a crystal consisting of N unit cells and with n atoms in a unit cell, the differential scattering cross section can be written as,

$$\left(\frac{d\sigma}{d\Omega} \right) = N \frac{(2\pi)^3}{v_a} |F_N(\mathbf{Q})|^2 \sum_{\Gamma} \delta(\mathbf{Q} - 2\pi\Gamma) \quad (3.17)$$

where v_a is the unit cell volume, $F_N(\mathbf{Q})$ is the nuclear unit cell structure factor, Γ is a reciprocal vector defined as $\Gamma = h\mathbf{b}_1 + k\mathbf{b}_2 + l\mathbf{b}_3$. Here h, k, l are integers and $\mathbf{b}_1, \mathbf{b}_2$, and \mathbf{b}_3 define the reciprocal lattice of unit cell. The nuclear structure factor $F_N(\mathbf{Q})$ is given by,

$$F_N(\mathbf{Q}) = \sum_{j=1}^n \langle b_j \rangle e^{i\mathbf{Q} \cdot \mathbf{r}_j} \cdot e^{-M} \quad (3.18)$$

The Debye-Waller factor e^{-2M} takes into account the thermal motion of the nuclei. The intensity of the scattered neutrons in a diffraction experiment is directly proportional to the differential scattering cross-section ($d\sigma/d\Omega$) of the ensemble atoms.

3.2.3 Small-angle neutron scattering (SANS)

Small angle neutron scattering (SANS) is a powerful technique to investigate the size, shape, and orientation of the constituent particles in a structurally inhomogeneous sample. When the particle size is relatively large compared to the neutron wavelength λ (typically of the order of 4 to 10 Å), the scattering is

predominantly found at small scattering angles 2θ . The scattered intensity $I(\mathbf{Q})$ as a function of wave vector transfer $\mathbf{Q}=(4\pi/\lambda)\sin(\theta)$, can generally be described as:

$$I(\mathbf{Q}) = I_o \Delta\Omega \eta T V \left(\frac{d\Sigma}{d\Omega} \right) (\mathbf{Q}) \quad (3.19)$$

where I_o is the in coming neutron flux, $\Delta\Omega$ the probed solid angle, η the detector efficiency, T the sample transmission, V the sample volume in the neutron beam. The macroscopic differential scattering cross section $(d\Sigma/d\Omega)(\mathbf{Q})$ is related to microscopic cross section by $(d\Sigma/d\Omega)(\mathbf{Q}) = N(d\sigma/d\Omega)(\mathbf{Q})$, where N is the concentration of scattering particles. A schematic layout of a small-angle neutron scattering experiment is shown in figure (3.4).

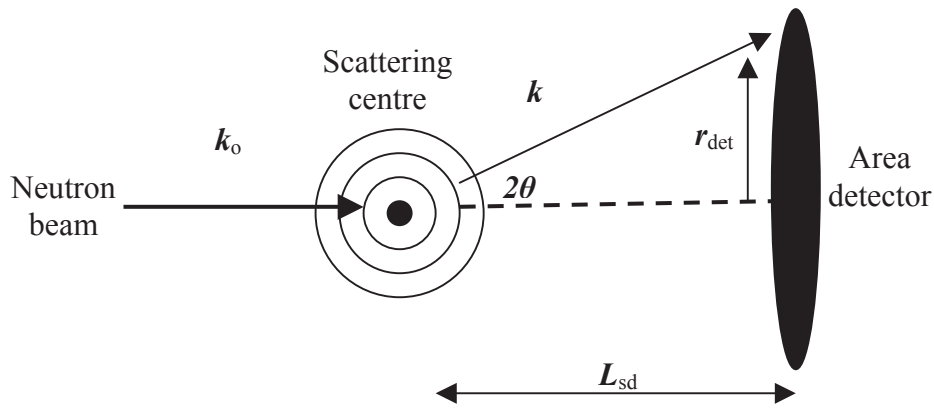


Figure 3.4 Schematic layout of a small-angle neutron scattering (SANS) experiment. The incident neutron beam is scattered by the scattering objects in the sample. A fraction of the neutrons scattered by an angle 2θ are recorded on a two dimensional detector at a distance L_{sd} from the sample at a radial distance r_{det} . k_0 and k are the wave vectors of the incident and scattered neutrons, respectively.

In small-angle neutron scattering experiments, the modulus of \mathbf{Q} probes the characteristic length scales in reciprocal space. Its magnitude for small angles is given by:

$$\mathbf{Q} = (4\pi/\lambda)\sin(\theta) \approx (2\pi/\lambda)(r_{det}/L_{sd}) \quad (\text{for small } \theta) \quad (3.20)$$

The equation (3.20) allows one to configure an instrument and insure that its \mathbf{Q} range will cover the length scales of interest.

For a two phase system with a sharp interface and no density fluctuations within the phases, the scattered intensity at high \mathbf{Q} is described by the Porod law [9] and decreases asymptotically with \mathbf{Q}^{-4} :

$$\frac{d\Sigma}{d\Omega}(\mathbf{Q}) = \frac{K_P}{\mathbf{Q}^4} + B \quad (3.21)$$

where B is the incoherent background, $K_P = 2\pi (\Delta\rho)^2 S_V$ is the Porod constant, S_V is the interface area per unit volume, between the two phases, and $\Delta\rho$ is the scattering contrast,

$$\Delta\rho = (\rho_p - \rho_m) \quad (3.22)$$

where ρ_p and ρ_m be the scattering length density of the particle and the matrix, respectively. The scattering length density is given by,

$$\rho = d N_A (\Sigma b_i / \Sigma W_i) \quad (3.23)$$

where d is the mass density, N_A is Avogadro's number, b_i is the coherent scattering length of element i , and W_i is the atomic weight of the element. The specific surface S_V can be extracted from the scattering data [9, 10] (even when the scale of the particles is much larger than the reciprocal of the minimum obtainable Q).

The small-angle neutron scattering (SANS) experiments described in this thesis were performed at the instrument D11 at the Institut Laue-Langevin (ILL) in Grenoble, France. The principle benefit of conducting SANS experiments at D11 is that the sample to detector distance L_{SD} can be changed between 1.1 and 36.7 meters, giving an accessible Q range from 5×10^{-4} to 0.44 \AA^{-1} .

3.3 Three dimensional X-ray diffraction

The three dimensional X-ray diffraction experiments described in this thesis were performed at the instrument ID11 at the European Synchrotron Radiation Facility (ESRF), Grenoble, France. A schematic layout of three-dimensional X-ray diffraction set-up [11-13], is shown in Fig. (3.5). A monochromatic X-ray beam with an energy of 70 keV and a photon flux of $\sim 1.3 \times 10^{11}$ cps was used to illuminate the sample. In our experiments an X-ray beams with a beam size of $200 \times 200 \text{ \mu m}^2$ and $300 \times 300 \text{ \mu m}^2$, were used. Images of the diffracted beam were acquired in transmission geometry by a CCD camera. The samples were placed in a cylindrical container. The special sample container was constructed from a glassy carbon rod (Goodfellows), with a container height of 25 mm, an inner diameter of 5 mm, and a wall thickness of 1 mm. The sample container was placed into a vertically aligned Quartz tube inside an X-ray transparent furnace. The furnace was fixed to a rotation table enabling sample rotation around the vertical axis.

For illustration, raw images acquired during the liquid to solid phase transformation of an Al-0.3Ti-0.02B alloy are shown in Fig. (3.6). The diffraction pattern from the molten sample (a) displays two characteristic liquid rings L_1 and L_2 associated with the short-range order in the molten aluminum before solidification. The inner most spurious ring is due to the scattering from the glassy structure of the Quartz sample container. The subsequent diffraction patterns (b-f) comprises of diffraction spots from aluminum grains, which nucleate and grow till virtually no intensity is left in the liquid rings, indicating that the phase transformation is complete.

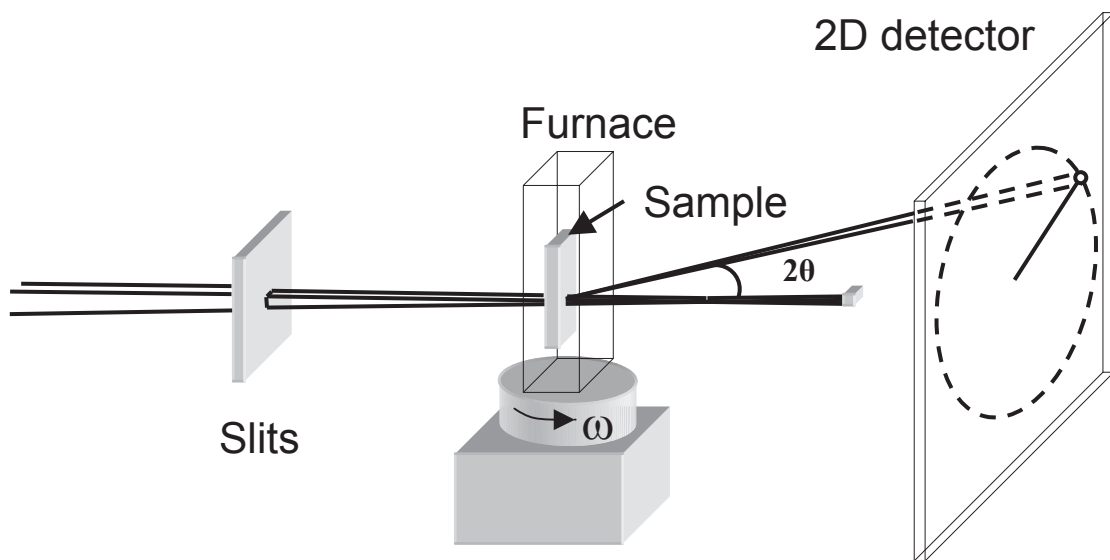


Figure 3.5 Schematic layout of the experimental X-ray diffraction set-up. A monochromatic beam of hard X-rays defined by slits illuminates the sample mounted in a vacuum furnace. The diffracted intensity, scattered over an angle 2θ , is monitored by a two dimensional detector while the sample is rotated over an angle ω around the vertical axis. The direct beam is shielded from the detector by a beam stop.

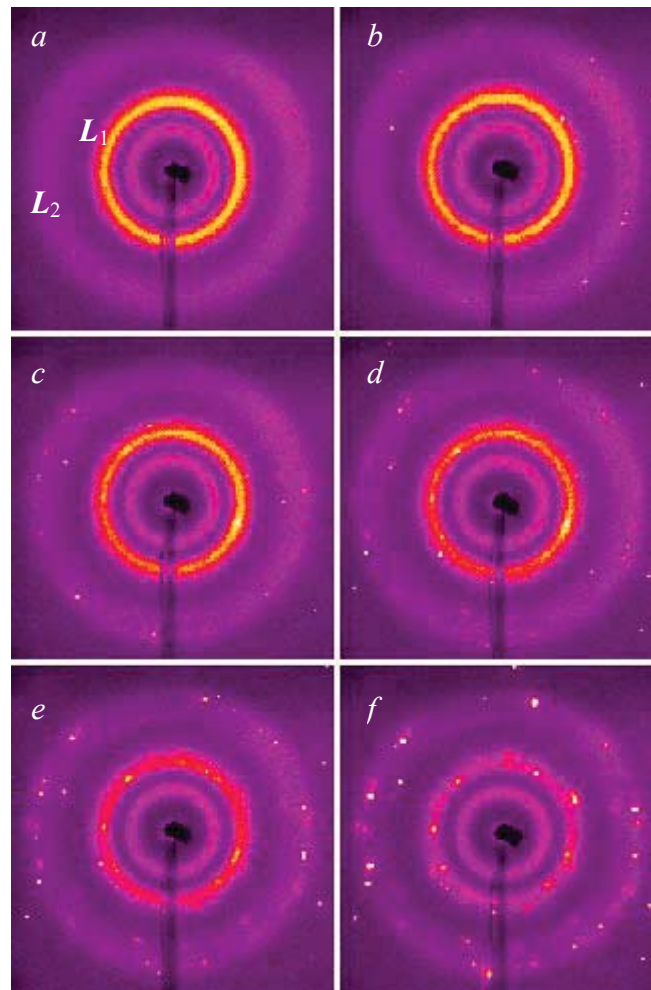


Figure 3.6 X-ray diffraction patterns measured for an Al-0.3Ti-0.02B (wt.%) alloy showing liquid to solid (*a*) to (*f*) phase transformation during solidification. The exposures are taken for a beam size of $300 \times 300 \mu\text{m}^2$ and the time interval between each exposure is 14 seconds. The two broad outer rings L_1 and L_2 in (*a*) correspond to first and second peaks in the liquid structure factor of molten aluminum, just before solidification. The bright spots are due to diffraction from individual grains that nucleate in the early stage of the phase transformation and grow until the phase transformation is complete (*f*). The innermost ring with constant intensity during phase transformation is due to diffuse scattering from the glassy structure of the quartz in the vacuum furnace.

3.3.1 Theory of X-ray diffraction

For each of the diffraction spot, the integrated intensity I_g is related to the volume of the grain V_g by the following equation [14, 15],

$$I_g = \Phi_0 r_0^2 \frac{\lambda^3 |F_{hkl}|^2 V_g(t)}{\Delta\omega |\sin \eta| v^2} L_g P T_r \exp(-2M). \quad (3.24)$$

Where Φ_0 is the incident flux of photons, F_{hkl} is the structure factor of the {hkl} reflection, λ is the photon wavelength, $\Delta\omega$ is the angular range over which the grain is rotated, v is the volume of the unit cell, P is the polarization factor, and T_r is the transmission factor. The Lorentz factor of the grain is given by $L_g = 1/\sin(2\theta)$, where 2θ is the scattering angle. The angles η and ω are shown in figure 3.5. The Thomson scattering length r_0 is given by

$$r_0 = \frac{e^2}{4\pi\epsilon_0 m_e c^2} = 2.82 \times 10^{-15} \text{ m}, \quad (3.25)$$

where $e = 1.602 \times 10^{-19}$ C is the electron charge, $m_e = 9.1094 \times 10^{-31}$ kg is the electronic mass, $c = 2.9979 \times 10^8$ m/s is the velocity of light, and $\epsilon_0 = 8.85419 \times 10^{-12}$ F/m is the permittivity of vacuum. The Debye-Waller factor $\exp(-2M)$ accounts for the thermal vibrations of the atoms [16],

$$M = \frac{6h^2 T}{mk_B \Theta^2} \left[\phi(x) + \frac{x}{4} \right] \left(\frac{\sin \theta}{\lambda} \right)^2 \quad (3.26)$$

where $h = 6.62608 \times 10^{-34}$ Js is the plank constant, m is the mass of the vibrating atom, $k_B = 1.381 \times 10^{-23}$ J/K is the Boltzmann constant, Θ is the Debye temperature ($\Theta_{Al} = 394$ K), $x = \Theta/T$ is the relative temperature, T is the temperature, and

$$\phi(x) = \frac{1}{x} \int_0^x \frac{\zeta}{\exp(\zeta) - 1} d\zeta. \quad (3.27)$$

The $\sin(\eta)$ term in equation (3.24) accounts for the fact that the scattering vector does not necessarily lie in the plane of rotation. The integrated intensity I_l per unit time of a segment of the liquid ring is given by

$$I_l = \Phi_0 r_0^2 N_0 V_L P T_r f^2(\mathbf{Q}) \left(\int_{\Delta\Omega} S(\mathbf{Q}) d\Omega \right) \quad (3.28)$$

Where $\mathbf{Q} = (4\pi/\lambda)\sin(\theta)$, N_0 is the number density of atoms in the liquid state, V_L is the illuminated volume of the liquid, $S(\mathbf{Q})$ is the liquid structure factor and Ω is the solid angle and f is the atomic scattering factor. The considered segment probed on the 2D

detector defines $\Delta\Omega$. The volume of an individual grain is calculated from the measured Bragg peak intensity of a grain I_g normalized by the liquid intensity I_l of the first liquid ring at the start of the transformation. Combining equations (3.24-3.28) gives

$$V_g = \frac{N_0 V_L \left(\int_{\Delta\Omega} S(Q) d\Omega \right) f^2(\mathbf{Q}) \Delta\omega |\sin(\eta)| v^2}{\lambda^3 |F_{hkl}|^2 L_g \exp(-2M)} \frac{I_g}{I_l}. \quad (3.29)$$

3.3.2 Experimental procedure

The nucleation rate and the size of the grains was determined by measuring the number and integrated intensity of the diffraction spots respectively. In order to measure the nucleation rate of α -aluminum grains, the beam size was set to $200 \times 200 \mu\text{m}^2$, thereby defining a gauge volume of $V_{\text{gauge}} = 200 \times 200 \times 5000 \mu\text{m}^3$, and the sample was rotated over an angle of $\Delta\omega = 1$ degree during exposure. So-called validation tests were made after every exposure by increasing the beam size to $300 \times 300 \mu\text{m}^2$. With these settings subsequent exposures were recorded during the transformation with a time resolution of 7 seconds. By comparing the integrated intensities of the diffraction spots for these two different beam sizes, it was tested whether the associated grain had in fact nucleated into the illuminated gauge volume and did not grow into the gauge volume from its neighbourhood. The time of nucleation of a grain corresponds to the moment when the integrated intensity of a reflection from a single grain I_g is $I_g > I_b + 2\sigma$, where I_b is the background liquid intensity and σ the corresponding standard deviation of the statistical noise. Then by counting number of, instantaneously nucleated diffraction spots during the liquid to solid phase transformation provided a quantitative measure of nucleation rate during solidification.

In order to measure the growth of individual grains a slightly different route was adopted. The same beam sizes of $200 \times 200 \mu\text{m}^2$ and $300 \times 300 \mu\text{m}^2$ were used alternatively to take four consecutive exposures. During each exposure the sample was rotated over an angle of $\Delta\omega = 1$ degree, covering a complete rotation of four degrees for each beam size. The diffraction spots that were found to be fully illuminated in the two central exposures were taken as valid spots. The diffraction spots mostly appear at scattering angles that overlap with the liquid peaks. As the intensity of liquid peaks decreases during solidification, a time dependent background correction was applied for each of the diffraction spots. An area of interest was defined for each of the diffraction spot, as shown in figure 3.7. A raw integrated intensity of the diffraction spot I_R was obtained by,

$$I_R = \sum_{\eta=\eta_1}^{\eta_2} \sum_{2\theta=2\theta_1}^{2\theta_2} I_i(\eta, 2\theta) \quad \text{where} \quad \left\{ \begin{array}{l} \eta_1 < \eta < \eta_2 \\ 2\theta_1 < 2\theta < 2\theta_2 \end{array} \right\} \quad (3.30)$$

where I_i is the intensity of each pixel i and the angles η and 2θ are defined in Fig. 3.7. The background intensity I_B corresponds the integrated intensity over an area of interest of the same size, located next to the diffraction spot,

$$I_B = \sum_{\eta=\eta_2}^{\eta_3} \sum_{2\theta=2\theta_1}^{2\theta_2} I_i(\eta, 2\theta) \text{ where } \begin{cases} \eta_2 < \eta < \eta_3 \\ 2\theta_1 < 2\theta < 2\theta_2 \end{cases} \quad (3.31)$$

where $\eta_3 - \eta_2 = \eta_2 - \eta_1$. The absolute scattered intensity from the aluminum grain at the time t is,

$$I_g(t) = I_R(t) - I_B(t) \quad (3.32)$$

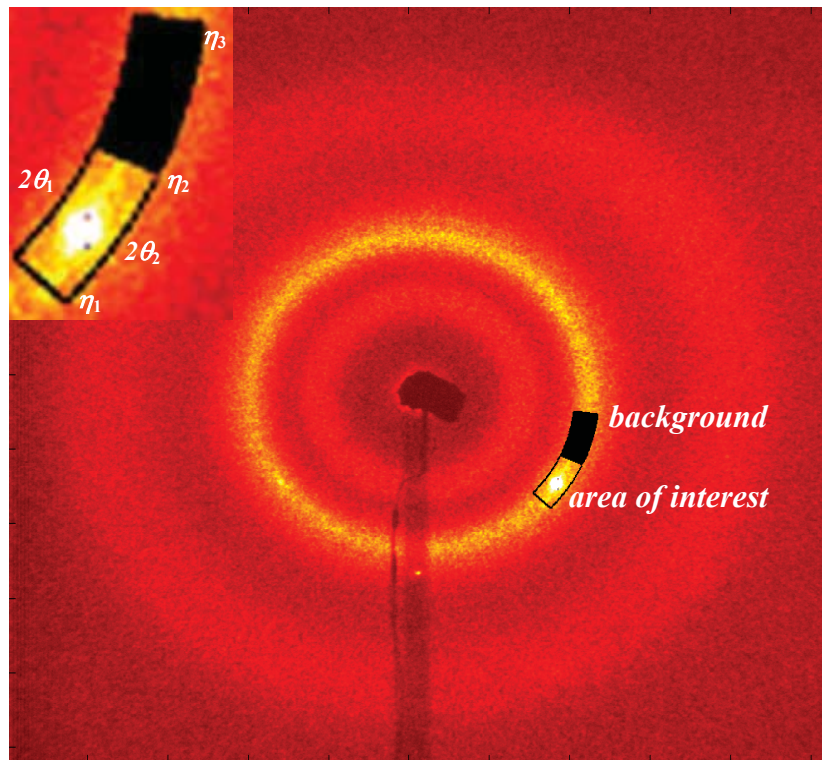


Figure 3.7 Area of interest defined by the scattering angles $2\theta_1$ to $2\theta_2$ and the azimuthal angles η_1 to η_2 , containing a diffraction spot (see insert). The corresponding background is the integrated intensity over the an area of the same size, located next to the area of interest. The time dependent absolute intensity of each diffraction spot during solidification is obtained by a subtraction of the background from the integrated intensity in the area of interest.

References:

- [1] G. Hakvoort, Ph.D. Thesis, Delft University of Technology, 1978.
- [2] A. P. Gray, *Analytical Calorimetry*, R. F. Porter ed., Plenum, New York, 1968, 209.
- [3] P. G. W. Remijn, Master Thesis, Delft University of Technology, 1997.
- [4] H. J. Borcherd and F. Daniels, *J. Am. Chem. Soc.* 79 (1957) 41.
- [5] D. L. Price and K. Skold, *Methods of experimental physics*, Vol. 23, Part A, Editors: Academic Press, New York (1987).
- [6] V. M. Niels, D. A. Keen, W. Hayes, and R. L. McGreevy, *J. Phys. Condens. Matter.* 4 (1992) 6703.
- [7] S. W. Lovesey, *Theory of neutron scattering from condensed matter*, Vol. 1, Oxford University Press, Oxford (1984).
- [8] G. L. Squires, *Introduction to the theory of thermal neutron scattering*, Cambridge University Press, Cambridge, (1978).
- [9] G. Porod, *Z. Kolloid.* 124 (1951) 83.
- [10] R. A. van Nordstrand and K. M. Hach: *Small Angle X-ray Scattering of Silica and Alumina Gels* (Am. Chem. Soc. Meeting Chicago, Sept. 1953) p. 61.
- [11] H. F. Poulsen, S. Garbe, T. Lorentzen, D. J. Jensen, F. W. Poulsen, N. H. Andersen, T. Frello, R. Feidenhans, and H. Graafsma, *J. Synchrotron Rad.* 4 (1997) 147.
- [12] U. Lienert, H. F. Poulsen, and A. Kvik, Proceedings of the 40th conference of the AIAA on Structures, Structural dynamics and Materials, St. Louis, MO, April 1999.
- [13] Poulsen, H. F., *Three Dimensional X-Ray Diffraction Microscopy, Mapping Polycrystals and Their Dynamics*, Springer Tracts in Modern Physics, Vol. 205, Springer, Berlin, (2004).
- [14] J. Als-Nielsen and D. McMorrow, *Elements of Modern X-ray Physics*, Wiley, West Sussex, 2001.
- [15] B. E. Warren, *X-ray Diffraction*, Dover Publications, New York, 1990.
- [16] B. D. Cullity and S. R. Stock, *Elements of X-ray Diffraction*, Prentice-Hall, New Jersey, 2001.

PART II

Experimental Results and Discussion

Chapter 4

Review of experimental results

4.1 Aluminum

Aluminum is the most common metallic element in the earth's crust but metallic aluminum does not exist in the natural state. It has to be extracted from an ore, most commonly bauxite. Pure aluminum is too soft to be used for technological applications. But mixed with small amounts of other metal to form alloys, it can provide the strength of steel, but with only half the weight. The aluminum alloys show excellent mechanical properties among the existing structural materials and are of great practical value for modern day technological applications [1]. It makes a key contribution to commercial air travel, fuel-efficient engines in cars and trucks as well as to high speed rail and sea travel. It facilitates the construction of corrosion-resistant and low maintenance cost buildings. Aluminum in packaging preserves food quality and avoids waste, and its low weight reduces fuel consumption and emissions during transportation. Around the world, most high voltage overhead transmission and distribution lines over long distances are made of aluminum.

4.2 Solidification

4.2.1 General concept of nucleation

Once extracted from ore, solidification from liquid into solid, is the most important phase transformation in the development of aluminum products. Once the liquid temperature is below melting during cooling, the creation of a solid phase from a metastable (undercooled) liquid phase occurs via embryos of the solid phase (see section 2.1). Embryos are small, transient clusters of the forming solid phase, which exist in various sizes, dispersed in the liquid phase. These clusters are too small to be seen by the naked eye, even using optical microscopes. Continuous fluctuations in the size of these clusters, via the attachment of additional atoms and the detachment of others, may result in a cluster growing large enough to become stable, i.e. for growth to become overwhelmingly more probable than decay. This is expressed as reaching the critical size of stability and hence nucleation of the forming solid phase, as shown in figure 4.1(a). As the temperature decreases, these nuclei continuously grow in size (called grains) until all the liquid is consumed. A schematic layout illustrating nucleation and grain growth during solidification of pure aluminum is shown in figure 4.1. Having solidified the pure aluminum, grains can be of the order of 10 mm in size. Such a grain size would give poor strength and surface properties and make casting difficult without cracking. Therefore, a special processing route is needed to reduce the grain size in aluminum during solidification, in order to tailor its mechanical properties. This is achieved by increasing the nucleation rate of aluminum grains through the heterogeneous nucleation process upon solidification.

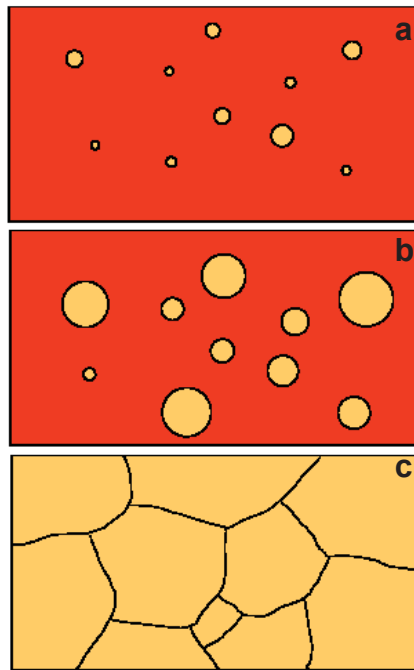


Figure 4.1 Schematic illustrations of grain nucleation and growth (a to c) during solidification of pure aluminum. (The dark gray represents the liquid phase while the light gray represents the solid phase)

In addition to the above picture, in which embryos are viewed as isolated clusters dispersed in the liquid phase, the situation needs to be considered in which the embryos are attached to some pre-existing structure, most likely a solid surface, in such a way that the likelihood of the embryo to reach stability is increased. This is called heterogeneous nucleation, compared to the previously considered homogenous nucleation process. By definition (section 2.2), homogenous nucleation requires a greater degree of metastability or undercooling, than heterogeneous nucleation. Therefore the nucleation rate increases during solidification once the substrate particles are present in the melt. A number of possibilities illustrating the heterogeneous nucleation on substrate during solidification are shown in figure 4.2.

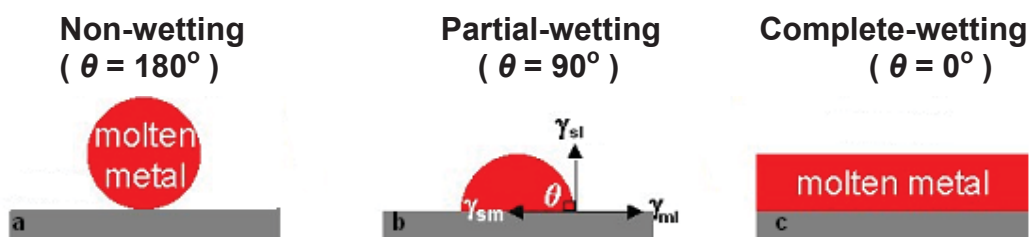


Figure 4.2 Some simple shapes of heterogeneous nucleation on a substrate upon solidification.

The simplest and most fundamental notion for viewing heterogeneous nucleation of aluminum grains on the substrates derives from the phenomenon of wettability and its reflection in the contact angle. On an insoluble substrate the embryo of the solid phase is assumed to have a spherical cap shape with the contact angle characterizing the relationship between the three interfacial energies involved, shown in Figure 4.2b. From the balance of forces, the contact angle, θ , relation can be derived (for details see section 2.1.2).

The energy barrier to nucleation of spherical nucleus on the substrate can be related to the energy barrier for homogenous nucleation as,

$$\Delta G_{het}^* = f(\theta)\Delta G_{hom}^* \quad (4.1)$$

where $f(\theta) = (1/4)(2 + \cos(\theta))(1 - \cos(\theta))^2$ is a monotonic function varying between 0 and 1. Starting from this general picture the nucleation rate on the substrate can be deduced. The main factor to introduce is the appropriate form of $f(\theta)$. The most difficult parameter to evaluate wetting angle is the interfacial energy between the embryo and the substrate. The interface energy may depend on the type of atoms, the lattice parameters and the specific surface features of the substrate. Therefore, the microscopic significance of nucleation needs to be considered.

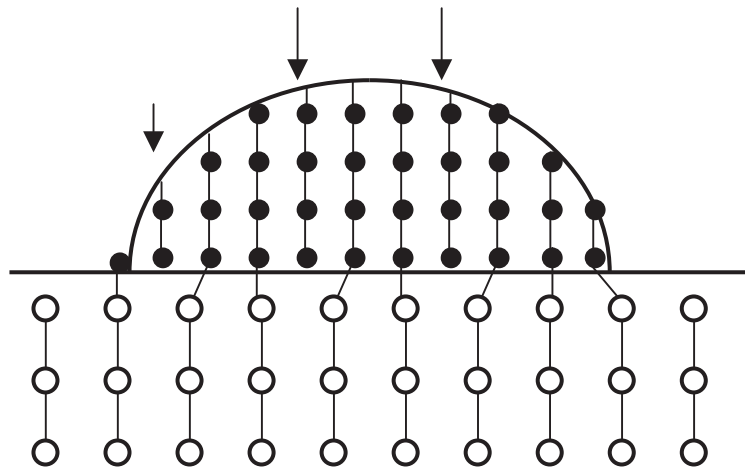


Figure 4.3 An embryo growing on a crystalline substrate with a misfit. The interface is dislocated, dislocations being indicated by arrows. In the case of a coherent epitaxy, the embryo would be deformed elastically to eliminate the dislocations.

Figure 4.3 illustrates the lattice misfit between embryo and the substrate and shows the two rather distinct ways in which an embryo can grow on the substrate. First the embryonic lattice may retain its normal lattice dimensions right to the interface. In this case there is said to be dislocation between the sheet of atoms in the surface layer between the embryo and the substrate. Second if the dislocation is small, the embryonic lattice may deform to join coherently to the substrate lattice. Which is known as elastic deformation. Clearly one can expect a dislocated boundary when the substrate differs greatly from embryo in lattice structure while elastic deformation will occur when the substrate is similar to embryo in lattice structure. In general, a

combination of these two, dislocation plus elastic deformation, is expected. Dislocations have the general affect of increasing γ_{sm} and hence increasing the contact angle. The elastic deformation (strain) raises the bulk thermodynamic energy of the embryo. Both of these effects lower the nucleating efficiency of the substrate. One can conclude that the best nucleating substrate must have a lattice structure like or very nearly like the embryo itself.

4.2.2 Grain refinement during aluminum solidification

The grain refinement is the science of practicing heterogeneous nucleation during solidification, thereby making aluminum alloys with smaller grains (grain size reduces to a fraction of a mm) [2,3]. During the industrial practice of grain refinement, a small fraction of Al-Ti-B (~0.02 wt. %) master alloy is added in molten aluminum before solidification. These master alloys when mixed in pure aluminum, contain micrometer size intermetallic particles (e.g. TiB_2 etc) along with some solute titanium. The surface of these particles is supposed to enhance the nucleation of aluminum grains upon solidification, while the diffusion of solute titanium restricts the grain growth during solidification. These two processes are thought to be fundamental during grain refinement, leading to reduced grain size in solid aluminum [4,5].

While the grain refinement is being practiced in industry since the last 50 years, a comprehensive understanding of this process is still lacking [5]. Experimental observations have shown that the presence of TiB_2 particles alone, without solute titanium, does not activate the nucleation of aluminum grains upon solidification. The questions of most importance are related to grain genesis. How does a grain begin its life upon solidification of grain refined aluminum alloys containing solute titanium and TiB_2 substrates? Why solute elements are essential for grain refinement? A large part of the problem comes from the difficulty of characterizing the embryonic formation on substrate surfaces and the specific features of these surfaces that serve as catalysts for grain nucleation upon solidification. Needless to say, many attempts have been made to deal with the problem, and there is a rich body of literature to attest to it. Even so, it is fair to say that the experiments and the theories serve more as a synthesis of ideas and a frame of reference for further studies than a basis for quantitative results on heterogeneous nucleation of aluminum grains.

4.2.3 Paradigms of grain refinement

The available grain refinement theories are arbitrarily divided into the so-called nucleant and solute paradigms. The solute paradigm mainly focuses on constitutional undercooling caused by the partitioning of solute elements. According to this paradigm the nucleation of aluminum grains starts first at the container wall. The development of constitutional undercooling at the interface of the first grains activates nucleation on the nucleant particles present there. This starts a wave of nucleation events through the bulk of the liquid. The authors who uphold the former line of investigation consider the nucleant particles to be responsible for the enhanced nucleation of aluminum grains in the melt during solidification. However, as stated earlier the surface of TiB_2 substrates exhibits poor nucleation ability for aluminum grains upon solidification. The TiB_2 substrate has a hexagonal lattice structure, which is different from face-centered cubic structure of the aluminum grains. This crystallographic incompatibility has been concluded to be the reason for the poor

nucleation efficiency of TiB_2 . However, in the Al-Ti-B master alloys, in addition to TiB_2 particles, TiAl_3 particles are also present. These aluminide particles are of particular interest because of a strong chemical interaction between TiAl_3 and the liquid to form solid aluminum via a peritectic reaction. In addition, there is a better degree of lattice matching between aluminum and the tetragonal structure of TiAl_3 , making it a better nucleant for aluminum. The aluminide particles are however usually large in size (30-40 μm) and in the cast microstructure after solidification; do have undesirable effects in the subsequent rolling and recrystallisation. Therefore, when mixed in pure aluminum during grain refinement, the titanium concentration is restricted to be much less than 0.15 wt.%. Thus, although excess titanium insures that TiAl_3 is present in master the alloys, the titanium content of the final melt is so low that TiAl_3 particles cannot survive [3,5]. None the less, it is observed that only a small fraction of excess titanium content is necessary for grain refinement and the higher titanium contents, sufficient to insure TiAl_3 survival in the melt do not give an improved performance.

On the basis of much research [4,5], it appears that grain refinement results from a combined action of TiAl_3 and TiB_2 , even when TiAl_3 is not stable in melts with the usual titanium contents much less than 0.15 wt.%. Excess titanium in the form of TiAl_3 is somehow preserved in nearly pure aluminum melts in the presence of TiB_2 particles. Various suggestions, illustrated in figure 4.4, have been made concerning how the TiB_2 could act to preserve the TiAl_3 locally. (a) A shell of TiB_2 particles surrounds the aluminide particles and does not let these particles dissolve [6,7]. (b) The aluminides survive in the edges and cavities present in TiB_2 particles [8]. (c) The aluminides are formed as adsorbed layers on the TiB_2 particles [9,10]. All these suggestions are based on the studies of solidified microstructures of grain refined aluminum alloys and do not permit much progress beyond this point. The detailed microstructure of the nucleation process is obscured by subsequent growth. The nucleating particles eventually become surrounded by solid aluminum. Critical amounts of TiAl_3 may be removed by its peritectic reaction with the liquid. A method is therefore required that can probe the solidification at the nucleation stage, so that nucleation mechanism can be studied microscopically.

4.3 Experiments and Results in this thesis

As demonstrated in the previous chapter, modern day experimental techniques have entered a new phase of development. It has made possible the real time investigation of nucleation process and the growth kinetics of individual grains during solidification. This opens up possibilities for revising the mechanism(s) involved in grain nucleation on specific substrates and the statements made by grain refinement theories. The practical use of these experimental techniques is employed in upcoming chapters in order to reveal the secrets of grain refinement during solidification of grain refined aluminum alloys. Particular attention has been paid to elucidate the role of excess titanium in combination with TiB_2 particles. By using titanium metal and TiB_2 particles in powder form, we prepared high purity Al-0.15TiB₂, Al-0.1Ti, and Al-0.1Ti-0.1TiB₂ (wt.%) model alloys. In this way the prior existence of TiAl_3 phase is avoided, that is otherwise present in master alloys. A comparison of these three samples sheds light on the role of solute titanium in the grain nucleation on the TiB_2 substrates. Another sample prepared by using an Al-5Ti-0.2B master alloy has a composition Al-0.3Ti-0.02B (wt.%), with iron as a major impurity (0.2 wt.%). The boron is present in the form of TiB_2 .

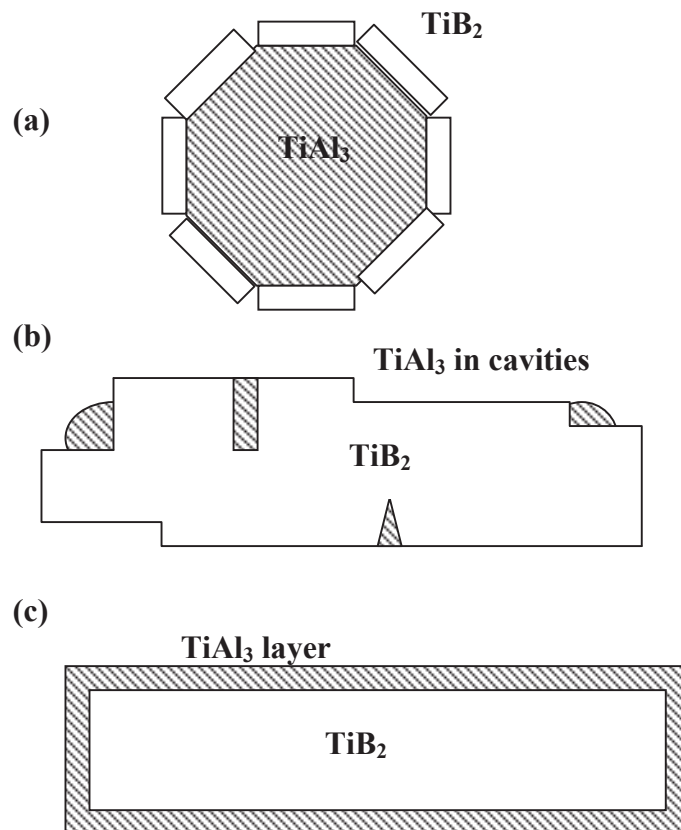


Figure 4.4 Schematic illustration of possible mechanisms by which TiB₂ particles could preserve TiAl₃ for melt compositions outside the concentration range for its bulk stability [2].

Differential thermal analysis (DTA) serves as a reliable experimental method for studying the liquid to solid phase transformation during solidification. In this thesis, the solidification process of pure aluminum along with grain refined aluminum alloys is studied by using DTA. The poor efficiency of TiB_2 particles for the nucleation of aluminum grains upon solidification has been supported by DTA curves. The results shown in chapter 5 indicate that the Al-0.15TiB₂ and Al-0.1Ti alloys exhibit a higher undercooling upon solidification, compared to the Al-0.1Ti-0.1TiB₂ alloy. It suggests that the excess titanium reduces the energy barrier to nucleation and plays an important role to activate nucleation on the TiB_2 substrate. How a small amount of solute titanium increases the nucleation efficiency of TiB_2 particles, still remains a secret.

The analysis of DTA curves during solidification of the Al-0.3Ti-0.02B alloy, exhibits characteristic peaks especially at slow cooling. When compared with the calculations obtained using the thermodynamic data base MTDATA, it suggests the formation of a TiAl_3 phase prior to solidification while $\text{Fe}_4\text{Al}_{13}$ at the end of solidification of aluminum. As mentioned in the previous section, the TiAl_3 is known to act as an efficient nucleant for aluminum grains upon solidification. It can activate nucleation of aluminum grains either by a peritectic reaction or through the formation of a TiAl_3 layer on the surface of TiB_2 particles. However, the onset temperature of the Al-0.1Ti-0.1TiB₂ alloy, upon solidification, is found to be quite close to that of the Al-0.3Ti-0.02B alloy. A comparison of DTA curves during slow cooling of both alloys also seems to exhibit a kinetic similarity at the onset of solidification. This implies that the same nucleation mechanism may be applicable during grain nucleation upon solidification in both alloys.

The detailed analysis of each DTA curves exhibits a phenomenological asymmetry during the solidification process. This behaviour is more pronounced in aluminum containing solute titanium and TiB_2 particles. This can be (a) due to the effect of latent heat that influences the nucleation rate, (b) the grain growth restriction by solute titanium during solidification. As, nucleation is an exponential function of undercooling. When nucleation rate is higher in grain refined aluminum alloys, the release of latent heat might eliminate the nucleation process soon after the solidification starts. Also, due to its large partition coefficient, the solute titanium has more affiliation for solid grains than liquid during solidification. As the solidification proceeds, the liquid aluminum becomes deficient with solute titanium. As a consequence this can result in the gradual increase of grain growth. These variations in intrinsic mechanism influence the transition rate, which is reflected in the DTA curves.

Differential thermal analysis, though quite accurate in predicting the energy barrier to nucleation in terms of undercooling, only provides information about the overall kinetics of the phase transformation during solidification. However neutrons can probe the bulk of the samples, and reveal information simultaneously about the liquid and the solid during solidification. Neutrons, once scattered from a mixture of liquid and solid, exhibit two distinct spectra. When solidification starts, the neutrons scattered from the liquid phase constitute a spectrum of broad peaks reflected in the structure factor $S(Q)$, inferring the short range order among the liquid atoms. While the neutrons scattered from the solid grains, exhibit sharp Bragg peaks in the structure factor, as shown in chapter 6. When the grains grow in size during solidification, the intensity of the liquid peak decreases due to decrease in liquid fraction while that of the Bragg peaks increases. It is interesting to explore whether the grain refiners

influence the short range order of the liquid atoms in aluminum. A deduction may be drawn about the link between the short range order of the liquid atoms and the nucleation process. In this thesis the liquid structure of pure aluminum and that of grain refined aluminum alloys is investigated, prior to solidification. The results indicate that the structure factor $S(Q)$ of pure aluminum before solidification is quite similar to that of grain refined aluminum alloys. It is suggested that the presence of grain refiners does not significantly alter the short-range order of liquid aluminum before solidification [11,12].

The role of grain refiners during crystallization behaviour of aluminum upon solidification is also studied. The Johnson-Mehl-Avrami model is applied to approximate the kinetic parameters like Avrami exponent n and the rate constant k for the evolution of solid fraction f_s during solidification. Using reasonable values for the adjustable constants, it is shown that the rate constant k is almost the same order of magnitude for pure aluminum and the Al-0.15TiB₂ alloy at a given cooling rate. This shows a little influence of TiB₂ particles on crystallization of aluminum and a fair agreement with the previous findings. However the presence of solute titanium strongly affects the crystallization kinetics. The rate constant k is found to decrease by an order of magnitude during solidification of the Al-0.1Ti and Al-0.3Ti-0.02B alloy. At first instance it seems that solute titanium predominantly controls the crystallization behaviour during solidification. But a comparison of the microscopic images of two samples showed a reduced grain size only for the Al-0.3Ti-0.02B alloy, which also contains TiB₂ particles. This signifies the fact that the kinetic parameters obtained from the Johnson-Mehl-Avrami model may not unambiguously characterise the phase transformation kinetics.

Once the solidification of the Al-0.3Ti-0.02B alloy starts, anomalous temporal fluctuations are observed in the Bragg-peak intensity of the solid grains during cooling [13]. A statistical analysis indicates that a possible movement of solid crystals in the liquid cannot simply explain these fluctuations during solidification. The nature of these fluctuations is not well known, and can have number of explanations such as grain deformation due to an unstable surface, partial dissolution, or grain ripening. The intensity fluctuations are analysed by a time-correlation function to extract the frequency and correlation time of the fluctuations. The frequency of these fluctuations seems to decrease during cooling.

In the preceding paragraphs, we have discussed notions rather than quantitative theory. It seems unlikely that a general theory could be formulated to cover the large number of factors involved in grain refinement during solidification. An avenue of interest may lie to quantitatively correlate the grain size as a function of cooling rate for different samples. This is achieved by small-angle neutron scattering (SANS) measurements during solidification of pure Al and of the Al-0.3Ti-0.02B (wt.%) alloy, for different cooling rates [14]. As the grain size decreases with increasing cooling rates, the surface area of grain boundary increases. The experimental data are fitted to the Porod law where the increase in Porod constant K_p during solidification is expected to be proportional to the specific surface S_V of the grain boundaries [15]. A comparison of both samples illustrates the variation in grain size of aluminum grains with and without grain refiners as a function of cooling rate.

Although the neutron scattering experiments provide distinct information about the liquid to solid phase transformation in aluminum alloys. It is still unable to predict the origin of grain genesis and quantitatively resolve the nucleation rate of aluminum grains during solidification, from the subsequent growth of these nuclei. Thanks to the three-dimensional X-ray diffraction microscope [16], which can

observe the nucleation of individual aluminum grains and monitor the size of each grain during solidification, as shown in section 3.3. Our time-resolved X-ray diffraction investigations shown in chapter 7, exhibit for the first time the nucleation profile during solidification and indicate how the nucleation rate increases with cooling rate. The results show that for all the samples, the nucleation process is complete for solid fraction below 30 %, irrespective of the cooling rate and sample composition [17,18]. This can be explained in terms of the release of latent heat upon solidification, which removes the undercooling required for further nucleation during solidification. A quantitative comparison of the nucleation profile for different samples at a given cooling rate, provides direct evidence that the nucleation rate is enhanced in the presence of both solute titanium and TiB_2 particles. Prior to the grain nucleation in such grain refined aluminum alloys, weak reflections of a metastable TiAl_3 phase are detected [18]. These TiAl_3 particles are formed roughly 10 K prior to the solidification of aluminum and gradually grow in size until the nucleation of aluminum grains starts. Once solidification starts, these TiAl_3 particles appear to dissolve again. This observation supports the highly debated mechanism proposed by the duplex nucleation theory [9-10] so as to enhance the grain nucleation. The nucleation rate significantly increases with increasing cooling rates. The growth of individual aluminum grains during solidification is experimentally observed and compared to model predictions for diffusion limited grain growth. The experimental results are in agreement with the theory in the first stage of the transformation. The release and distribution of latent heat again seems to play a significant role in restricting the grain growth, especially during slow cooling. This emerges a possible source of deviation between experiment and theoretical model based on titanium diffusion. A comparison of the experimental curves show that the grain growth behavior is alike for the Al-0.1Ti, and Al-0.1Ti-0.1 TiB_2 alloys, although the nucleation rate is rather different in both samples during solidification. This signifies the fact that the nucleation potency of the substrate particle is the limiting factor for grain refinement rather than the grain growth. An abnormal grain growth is observed during solidification of the Al-0.3Ti-0.02B alloy [19]. This behavior supports our earlier findings of the temporal fluctuations in Bragg-peak intensity during the neutron diffraction experiments.

References

- [1] J. G. Kaufman, Properties of aluminum alloys, Publisher: Materials Park: ASM International, 1999.
- [2] P. Schumacher, A. L. Greer, J. Worth, P. V. Evans, M. A. Kearns, P. Fisher, and A. H. Green, *Mater. Sci. and Tech.*, 14 (1998) 394.
- [3] D. G. McCartney, *Int. Mater. Rev.*, 34 (1989) 247.
- [4] M. Easton, and D. Stjohn, *Met. Mater. Trans.*, A30 (1999) 1613.
- [5] M. Easton, and D. Stjohn, *Met. Mater. Trans.*, A30 (1999) 1625.
- [6] M. Johnson, and L. Backerud, *Z. Metallkd.*, 83 (1992) 774
- [7] M. Vader, and J. Noordegraaf, *Proc. Light Metals*, (1989) 937.
- [8] D. Turnbull, *J. Chem. Phys.*, 18 (1950) 198.
- [9] P. S. Mohanty and J. E. Gruzleski, *Acta. Metall. Mater.* 43 (1995) 2001.
- [10] P. Schumacher and A. L. Greer, *Mater. Sci. and Engg. A*, 178 (1994) 309
- [11] N. Iqbal, N. H. van Dijk, V. W. J. Verhoeven, W. Montfrooij, T. Hansen, L. Katgerman, and G. J. Kearley, *Acta. Mater.* 51 (2003), 4497.

-
- [12] N. Iqbal, N. H. van Dijk, T. Hansen, L. Katgerman, and G. J. Kearley, *Mater. Science and Eng. A* 386 (2004) 20.
- [13] N. Iqbal, N. H. van Dijk, V. W. J. Verhoeven, T. Hansen, L. Katgerman, and G. J. Kearley, *Mater. Science and Eng. A* 367 (2004) 82.
- [14] N. Iqbal, N. H. van Dijk, C. D. Dewhurst, L. Katgerman, and G. J. Kearley, *Physica B*, 350 (2004) 1011.
- [15] G. Porod, *Z. Kolloid.* 124 (1951) 83.
- [16] H. F. Poulsen, *Three Dimensional X-Ray Diffraction Microscopy, Mapping Polycrystals and Their Dynamics*, Springer Tracts in Modern Physics, Vol. 205, Springer, Berlin, (2004).
- [17] N. Iqbal, N. H. van Dijk, S. E. Offerman, M. P. Moret, L. Katgerman , and G. J. Kearley, *J. of non crystalline solids* . (*Article submitted*).
- [18] N. Iqbal, N. H. van Dijk, S. E. Offerman, M. P. Moret, L. Katgerman , and G. J. Kearley, *Acta. Mater.* (*Article in press*).
- [19] N. Iqbal, N. H. van Dijk, S. E. Offerman, M. P. Moret, L. Katgerman , and G. J. Kearley, *Mater. Res. Soc. Symp. Proc., Vol.840* (2005) Q7.12.

Chapter 5

DTA measurements on aluminum alloys for the investigation of the crystallization kinetics during grain refinement

N. Iqbal, N. H. van Dijk, L. Katgerman, and G. J. Kearley. (to be submitted).

Abstract

The crystallization kinetics during solidification of high purity aluminum, Al-0.15TiB₂, Al-0.1Ti, Al-0.1Ti-0.1TiB₂ alloys, and a commercial purity Al-0.3Ti-0.02B alloy is investigated by differential thermal analysis (DTA) at various cooling rates ranging from 0.5 to 20 K/min and during melting with a heating rate of 10 K/min. The cooling rate dependence of the onset temperature T_o , the crystallization peak temperature T_p , and the latent heat ΔH are evaluated and compared for all samples. A reduced undercooling to activate nucleation of aluminum grains is observed when both solute titanium and TiB₂ particles are present in the liquid. The results illustrate a phenomenological asymmetry during first and second half of the phase transformation during solidification of grain refined aluminum alloys. This suggests a variation in intrinsic transition mechanism responsible for phase transformation during solidification. At slow cooling, an aluminide phase (TiAl₃) is found to form during solidification of Al-0.3Ti-0.02B alloy. A comparison of DTA curves during slow cooling of the Al-0.1Ti-0.1TiB₂ and the Al-0.3Ti-0.02B alloys seems to exhibit a kinetic similarity at the onset of the solidification. This implies that the same nucleation mechanism may be applicable for the understanding of grain nucleation upon solidification of these alloys.

5.1 Introduction

Grain refinement plays an important role in the liquid to solid phase transformation of aluminum alloys [1,2]. Generally Al-Ti-B master alloys are added to the aluminum alloys to refine the grain size of the solidified product. These alloys contain microscopic TiB₂ and TiAl₃ nucleating particles. Although various theories regarding the grain refining mechanisms are proposed [3-8], such as the particle theory, the phase diagram theory, the duplex nucleation theory, and the peritectic hulk theory, the mechanism of grain refinement remains a problem of considerable controversy in the scientific literature. The nucleant effects, i.e. which particle nucleates α -Al grains and what are its characteristics, has been the subject of intensive research. Lately, the solute effects, i.e. the effect of dissolved titanium on grain refinement, has become into forefront of grain refinement research. Therefore, a great interest exists to determine the kinetics of the liquid to solid phase transformation of aluminum alloys in order to determine the role of microscopic grain refining particles and solute titanium.

The present chapter describes differential thermal analysis (DTA) measurements on high purity aluminum, Al-0.15TiB₂, Al-0.1Ti, Al-0.1Ti-0.1TiB₂

(wt. %) alloys, and a commercial purity Al-0.3Ti-0.02B (wt. %) alloy during solidification at different cooling rates, to ascertain the mechanism of crystallization and to separate the effects of nucleating particle from that of the solute titanium.

5.2 Sample preparation

The studied samples were laboratory prepared from high purity aluminum, titanium, and TiB₂ particles. The pure aluminum (99.999 %) and titanium (99.99 %) were purchased from Goodfellow. The TiB₂ (99.99 %) powder with a particle size distribution ranging from 3 to 6 μm and a maximum around 4.4 micrometer was purchased from Advanced Ceramics.

The Al-0.15TiB₂ (wt. %) sample was prepared by melting together aluminum lumps with a total mass of 35 gram and the TiB₂ particles into an aluminum oxide crucible. The sample was heated to the temperature of $T = 1023$ K. After holding at this temperature for 30 minutes, the crucible was removed from the furnace and the liquid alloy was homogenized by stirring using an aluminum oxide rod. After solidification the sample was remelted and the above mentioned process was repeated three times to ensure that the TiB₂ particles were homogeneously distributed in the Al-0.15TiB₂ (wt. %) sample.

In order to prepare the Al-0.1Ti (wt. %) sample, a different route was adopted. First, Al-1Ti (wt. %) master alloy samples, of 5 gram each, were prepared by melting together the appropriate amounts of aluminum and titanium in an electric arc furnace in a high purity argon atmosphere. The molten samples were stirred by using the arc flame for homogenization. Then the samples were solidified, rotated by changing the top and bottom positions, and remelted. This process was repeated five times to ensure that titanium is homogeneously distributed in the sample. Having prepared the Al-1Ti (wt. %) master alloy samples, the Al-0.1Ti and Al-0.1Ti-0.1TiB₂ (wt. %) samples were prepared by melting the master alloy together with an appropriate amount of high purity aluminum and TiB₂ particles into it, by the method described for the Al-0.15TiB₂ sample. The chemical composition of these aluminum alloys was confirmed by using X-ray fluorescence spectroscopy (XRF).

The Al-0.3Ti-0.02B (wt.%) alloy was prepared from an Al-5Ti-0.2B (wt.%) commercial master alloy (KBM AFFILIPS). The particle size distribution of TiB₂ precipitates in the Al-0.3Ti-0.02B alloy was determined by optical microscopy and showed a particle size distribution in the range from 0.6 to 2.2 μm with a maximum around 1.2 μm. Iron was observed to be the main impurity (0.2 wt. %) present in this sample.

5.3 Experimental method

A Perkin-Elmer DTA instrument was used for measuring the nonisothermal crystallization kinetics during continuous cooling and heating. The temperature was calibrated using high purity zinc and aluminum samples for each of the applied cooling rate used in the measurements. All measurements were carried out in a helium atmosphere. From all materials, solid samples with a cubic shape and with dimensions of $2 \times 2 \times 2$ mm³ were used. For the crystallization experiment, the samples were heated to 973 K and kept for 5 min at that temperature to ensure that the sample is completely molten. Then the samples were cooled at constant rates of 0.5, 1, 5, 10,

and 20 K/min. The exothermic crystallization peak was recorded as a function of temperature. In order to investigate the corresponding melting behaviour, a sample of each material composition was also heated with a heating rate of 10 K/min. The corresponding endothermic peak was recorded as a function of temperature.

5.4 Results and discussion

5.4.1 Crystallization behaviour

Figure 5.1 shows the typical DTA curves obtained for pure aluminum, Al-0.15TiB₂, Al-0.1Ti, Al-0.1Ti-0.1TiB₂, and Al-0.3Ti-0.02B (wt.%) alloys during solidification at a constant cooling rate of 20 K/min. Two characteristic phenomena are resolved in the studied temperature range at this cooling rate. The first one corresponds to the variation in onset temperature of crystallization (T_o) and the second to the peak temperature of crystallization (T_p).

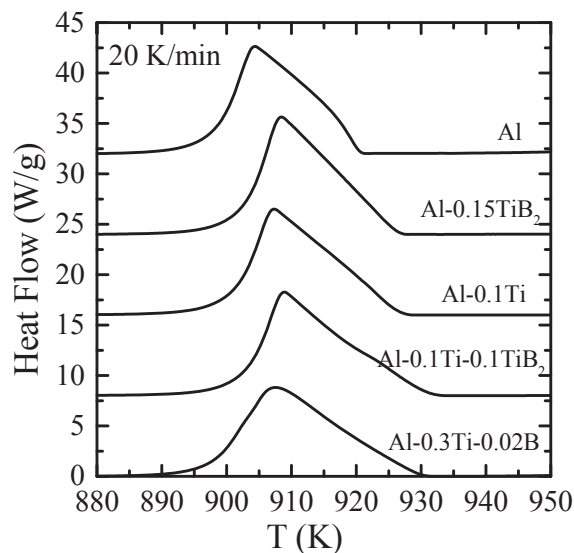


Figure. 5.1 Crystallization curves of the liquid to solid phase transformation for pure aluminum, Al-0.15TiB₂, Al-0.1Ti, Al-0.1Ti-0.1TiB₂ and Al-0.3Ti-0.02B alloys at a cooling rate of 20 K/min (for clarity each curve is shifted from the previous one by adding eight).

A complete set of DTA thermograms, measured for all sample compositions and at different cooling rates from 0.5 to 10 K/min is shown in figure 5.2. It is clear that the exothermic curves become wider and the characteristic temperatures shift to the lower values as the cooling rate increases. Table 5.1 summarizes the characteristic data of the crystallization exotherms for all the samples studied. A relatively low undercooling is found to activate the nucleation of aluminum grains upon solidification when both solute titanium and TiB₂ particles are present as observed for Al-0.1Ti-0.1TiB₂ and Al-0.3Ti-0.02B alloys. While, a higher undercooling is observed during solidification of the Al-0.15TiB₂ alloy, which confirms the poor surface properties of TiB₂ particles to activate the nucleation of solid aluminum.

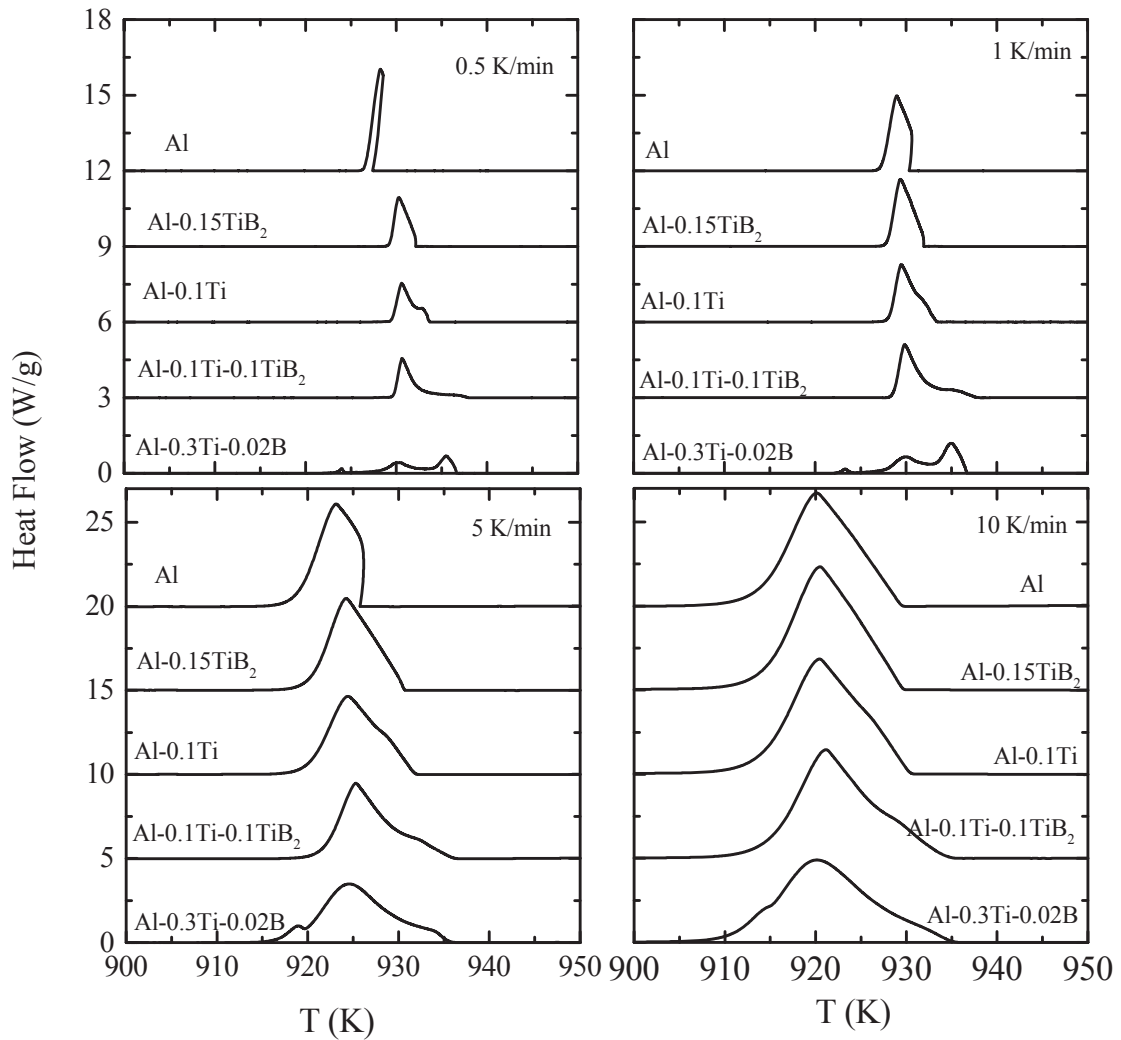


Figure. 5.2 Crystallization curves of the liquid to solid phase transformation at pure aluminum, Al-0.15TiB₂, Al-0.1Ti, Al-0.1Ti-0.1TiB₂ and Al-0.3Ti-0.02B alloys for cooling rates of 0.5, 1, 5 and 10 K/min. (for clarity each curve for 0.5 and 1K/min is shifted by adding three while for 5 and 10 K/min is shifted by adding five).

Table 5.1 Characteristic temperatures T_{on} and T_p and the heat released ΔH for the crystallization of aluminum alloys during continuous cooling at different cooling rates.

Cooling rate (K/min)		0.5	1.0	5.0	10.0	20.0
Al	T_{on} (K)	927.5	930.4	925.8	929.4	922.8
	T_p (K)	928.3	928.9	923.1	920.1	912.3
	ΔH (J/g)	425.7	423.2	381.3	348.8	404.1
Al-0.15TiB ₂	T_{on} (K)	932.1	931.9	930.6	929.6	927.5
	T_p (K)	930.2	929.4	924.2	920.5	913.2
	ΔH (J/g)	426.4	422.3	386.1	373.1	435.4
Al-0.1Ti	T_{on} (K)	933.6	933.5	931.8	930.4	928.0
	T_p (K)	930.6	929.5	924.4	920.4	912.9
	ΔH (J/g)	405.1	404.0	373.8	364.3	423.0
Al-0.1Ti-0.1TiB ₂	T_{on} (K)	937.8	938.3	936.7	935.3	933.3
	T_p (K)	930.7	929.8	925.3	921.2	913.7
	ΔH (J/g)	408.8	421.4	374.1	364.4	425.1
Al-0.3Ti-0.02B	T_{on} (K)	936.6	936.7	935.6	935.1	931.9
	T_p (K)	930.0	929.4	924.7	920.2	913.0
	ΔH (J/g)	438.1	347.6	383.6	343.1	425.9

The question of fundamental interest is how a small amount of titanium enhances the nucleation efficiency of TiB_2 particles. From the curves shown in Fig. 5.2, it is apparent that the DTA exotherms for the Al-0.3Ti-0.02B (wt. %) sample exhibit distinct peaks upon freezing at a temperature above ($T > T_p$), and below ($T < T_p$) the crystallization peak temperature, with size and sharpness being dependent on the cooling rate. The equilibrium phase diagram calculations using the thermo dynamical database MTDATA suggest that the two additional peaks present in the commercial purity Al-0.3Ti-0.02B sample at low cooling correspond to the formation of two additional phases, which are most probably TiAl_3 ($T > T_p$) and $\text{Fe}_4\text{Al}_{13}$ ($T < T_p$).

The formation of a TiAl_3 phase in the hyperperitectic Al-0.3Ti-0.02B alloy favours an enhanced nucleation in this sample. The experimental results of Mohanty et al. [9] and Schumacher et al. [10] have suggested that TiAl_3 layers are formed on the surface of TiB_2 particles, which makes it a better nucleation site for aluminum grains upon solidification. A comparison of DTA curves during solidification of the Al-0.1Ti-0.1 TiB_2 and Al-0.3Ti-0.02B alloys seems to exhibit a kinetic similarity and close resemblance in the undercooling before solidification. This similarity in freezing behaviour suggests that the same nucleation mechanism might be responsible for enhanced nucleation during grain refinement in hypoperitectic Al-0.1Ti-0.1 TiB_2 alloy.

A phenomenological asymmetry is observed at the right and left hand side of the DTA curves during the liquid to solid phase transformation. During slow cooling of pure aluminum the peak temperature of exothermal curve is even higher than then onset temperature. This indicates that the exothermal rate, due to latent heat, during freezing is larger than the heat removal due to cooling, and it can elevate the sample temperature. At the beginning of solidification, the exothermal rate seems to decrease with the addition of solute titanium, which in fact reduces the growth of aluminum grains and hence the solid fraction. When both solute titanium and TiB_2 particles are present, then in addition to growth reduction, the nucleation starts at low undercooling as shown in figure 5.2. The variation in slope at the right hand side of the DTA curves might be associated with the variation in nucleation behaviour caused by the release of latent heat. As shown in section 2.1, the nucleation is an exponential function of the melt undercooling. A slight decrease in melt undercooling e.g. due to release of latent heat, can abruptly cease the nucleation process. At the onset of solidification the evolution of solid fraction is controlled by both nucleation and growth. Soon after the nucleation starts, the release of latent heat stops the nucleation process. Finally, the solid fraction is controlled only by grain growth.

The difference in crystallization kinetics for different investigated samples during solidification can also be observed by comparing the relative crystallinity as a function of temperature $X(T)$ deduced directly from the heat flow (dH_C/dT) by using,

$$X(T) = \frac{\int_{T_o}^T \left(\frac{dH_C}{dT}\right) dT}{\int_{T_o}^{T_\infty} \left(\frac{dH_C}{dT}\right) dT} \quad (5.1)$$

where T_o , and T_∞ represent the crystallization onset temperature and end temperature, respectively and H_C be the enthalpy of crystallization. Figure 5.3 shows the relative

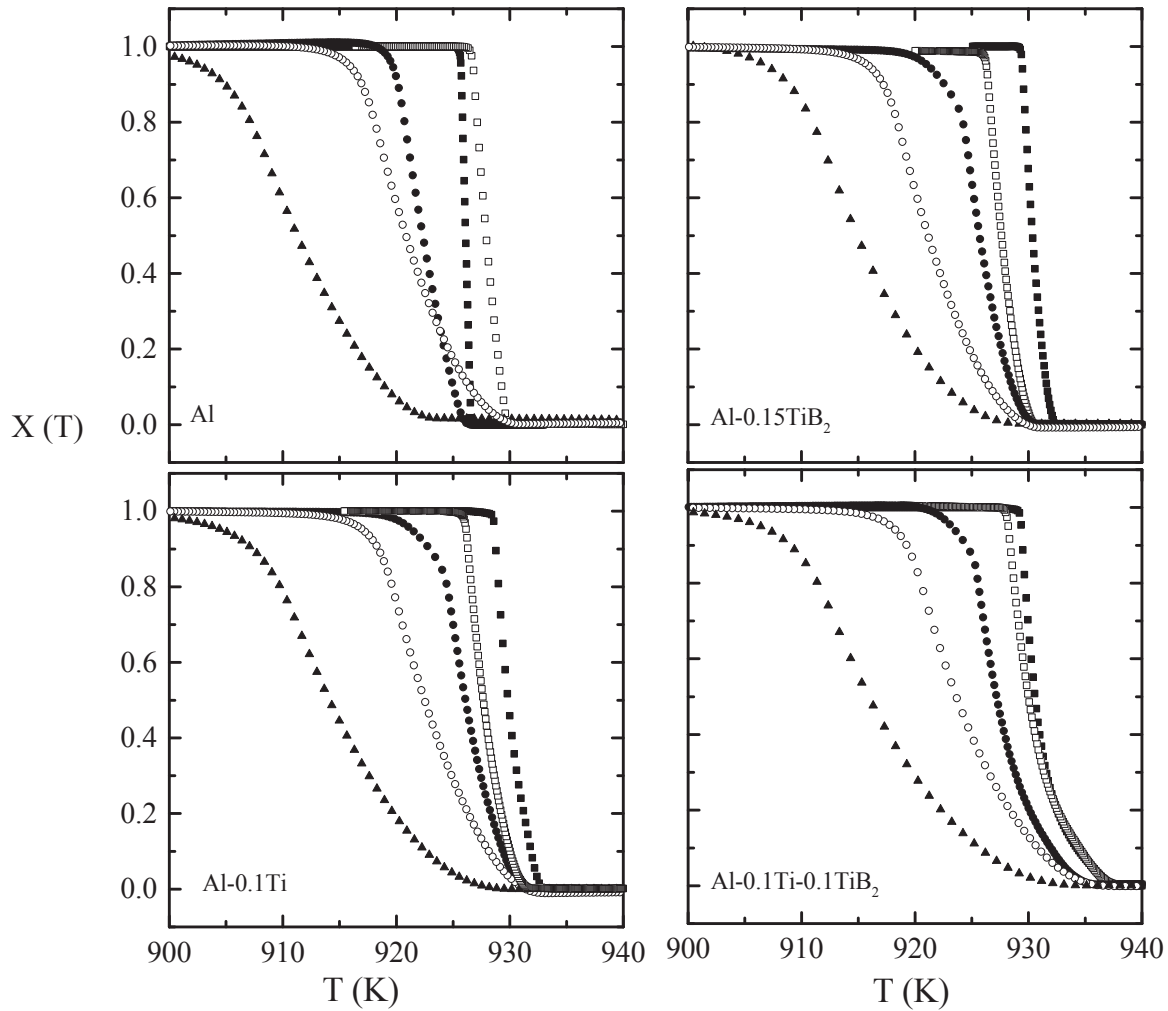


Figure. 5.3 Relative crystallinity $X(T)$ as a function of temperature for pure aluminum, Al-0.15TiB₂, Al-0.1Ti and Al-0.1Ti-0.1TiB₂ alloys at a cooling rate of (■) 0.5 K/min, (□) 1 K/min, (●) 5 K/min, (○) 10 K/min, and (▲) 20 K/min cooling rates.

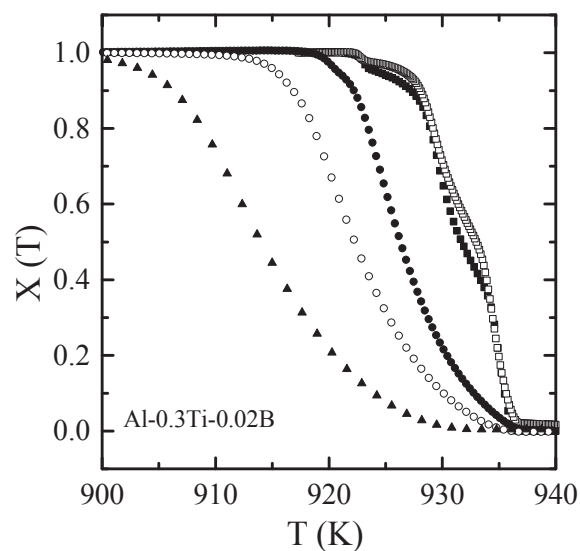


Figure. 5.4 Relative crystallinity $X(T)$ as a function of temperature for the Al-0.3Ti-0.02B alloy at a cooling rate of (■) 0.5 K/min, (□) 1 K/min, (●) 5 K/min, (○) 10 K/min, and (▲) 20 K/min cooling rates.

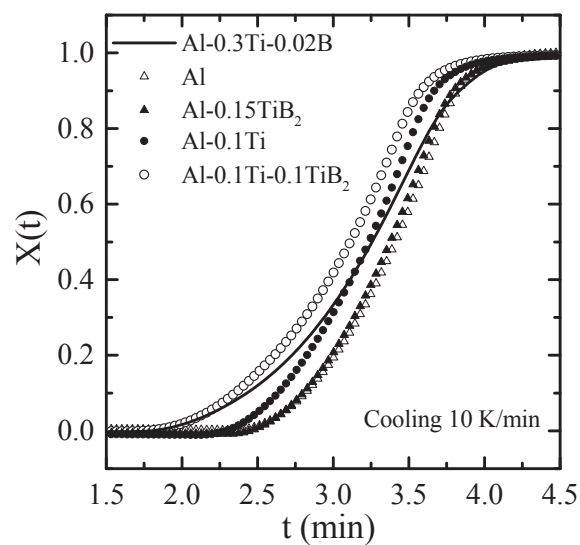


Figure. 5.5 Relative crystallinity $X(t)$ as a function of time for pure aluminum, Al-0.15TiB₂, Al-0.1Ti, Al-0.1Ti-0.1TiB₂, and Al-0.3Ti-0.02B alloys at a cooling rate of 10 K/min.

degree of crystallinity $X(T)$, as a function of temperature for all the high purity samples studied at various cooling rates. All the crystallization curves exhibit the traditional sigmoidal shape for the liquid to solid phase transformation. The transition temperature and transition rate changes significantly with cooling rate and sample composition. Figure 5.4 shows the evolution of the relative crystallinity $X(T)$ as a function of temperature during solidification for the commercial purity Al-0.3Ti-0.02B alloy. The results indicate that for higher cooling rates, the crystallization curves are analogous to those in figure 5.3 but change a lot for slow cooling. During slow cooling of the Al-0.3Ti-0.02B alloy, the freezing behaviour is altered by the segregation of titanium and iron present in the melt

The plots of the relative crystallinity as a function of time $X(t)$ for all the samples at a cooling rate of 10 K/min are illustrated in figure 5.5. It is clear from the plots that for the same cooling rate, the time evolution of the crystallization process during the liquid to solid phase transformation of pure aluminum and Al-0.1TiB₂ is almost identical. The nucleation starts earlier in time, at low undercooling, when both TiB₂ nucleating particles and the solute titanium is present as observed in the Al-0.1Ti-0.1TiB₂ and Al-0.3Ti-0.02B alloys. The addition of solute titanium, even at a hypoperitectic composition, enhances the nucleation potential of TiB₂ grain refining particles as illustrated by the Al-0.1Ti-0.1TiB₂ crystallization curve.

5.4.2 Melting behaviour

In order to investigate the effects of grain refining particles on the melting behaviour of aluminum, the samples were also heated with a constant heating rate of 10 K/min. An example of the endothermic curves and the corresponding change in crystallization fraction with temperature is shown in figure 5.6. The temperature range was chosen to be sufficiently wide to ensure that the melting was complete. The values of the heat absorbed during melting are given in Table 5.2 for each sample. The experimental results, for the variation in crystal fraction with temperature, for pure aluminum and the TiB₂ particles embedded in an Al matrix (Al-0.15TiB₂ alloy) indicate that the presence of TiB₂ impurities does not significantly change the melting kinetics in Al-0.15TiB₂ sample, compared to pure aluminum. The presence of solute titanium in aluminum, as observed in Al-0.1Ti alloy, is found to make a slight increase in super heating. The presence of Fe₄Al₁₃ due to the iron impurities in the commercial purity Al-0.3Ti-0.02B alloy constitutes a needle-like second phase particles with a low melting point. By using optical microscopy, these particles were found to be distributed along the grain boundaries, as shown in figure 5.7. The melting of Fe₄Al₁₃ starts earlier and results in a significant decrease in superheating of the sample, as observed in figure 5.6(b).

Figure 5.8. illustrates a phenomenological symmetry during melting and freezing of the Al-0.3Ti-0.02B alloy. The melting/freezing transition exhibits a thermal hysteresis and confirms the first order character of phase transformation. The width $\Delta T_{1/2}$ of the transformed fraction $X(T)$ versus T at $X(T) = 0.5$ is a useful quantitative measure of the thermal hysteresis. The corresponding values of $\Delta T_{1/2}$ for all the samples at a cooling/heating rate of 10 K/min are listed in Table 5.2 and decreases with the addition of grain refiners in aluminum. A comparison of the freezing curves with the equilibrium solidification temperature of aluminum (broken line at $T = 933$ K) in figure 5.9, clearly demonstrates the presence of significant undercooling during solidification of pure aluminum and Al-0.15TiB₂ alloys, while almost no undercooling is observed for Al-0.1Ti and Al-0.1Ti-0.1TiB₂ alloys.

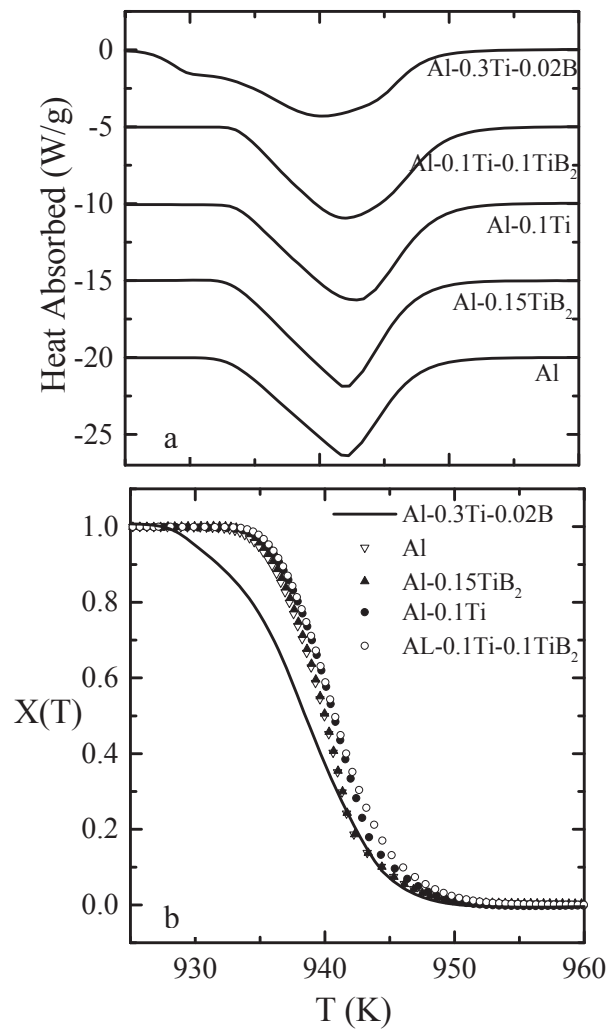


Figure 5.6 (a) Crystallization curves for pure aluminum, Al-0.15TiB₂, Al-0.1Ti, Al-0.1Ti-0.1TiB₂ and Al-0.3Ti-0.02B alloys (for clarity each curve is shifted from the previous one by subtracting five) and (b) relative crystallinity as a function of temperature for a heating rate of 10 K/min during the liquid to solid phase transformation.



Figure. 5.7 Optical microscopy image of the commercial purity Al-0.3Ti-0.02B (wt.%) alloy, at the room temperature. The needles like particles are observed at the grain boundary and correspond to the $\text{Fe}_4\text{Al}_{13}$ phase, formed during solidification.

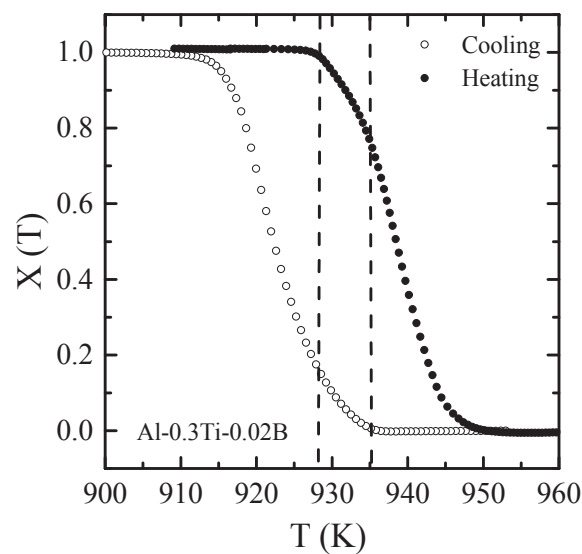


Figure. 5.8 Temperature dependence of the relative crystallinity for the Al-0.3Ti-0.02B alloy as a function of temperature during cooling and heating for a rate of 10 K/min. (The broken lines indicate the onset of freezing at $T=935.1$ K and melting at $T=928.5$ K).

Table 5.2 Heat absorbed ΔH during melting of aluminum alloys for a heating rate of 10 K/min, and the corresponding melting/freezing transformation width $\Delta T_{1/2}$.

Sample	Al	Al-0.15TiB ₂	Al-0.1Ti	Al-0.1Ti-0.1TiB ₂	Al-0.3Ti-0.02B
$\Delta T_{1/2}$ (K)	19.1	18.8	18.3	17.2	16.1
ΔH (J/g)	338.5	361.1	350.3	375.4	317.2

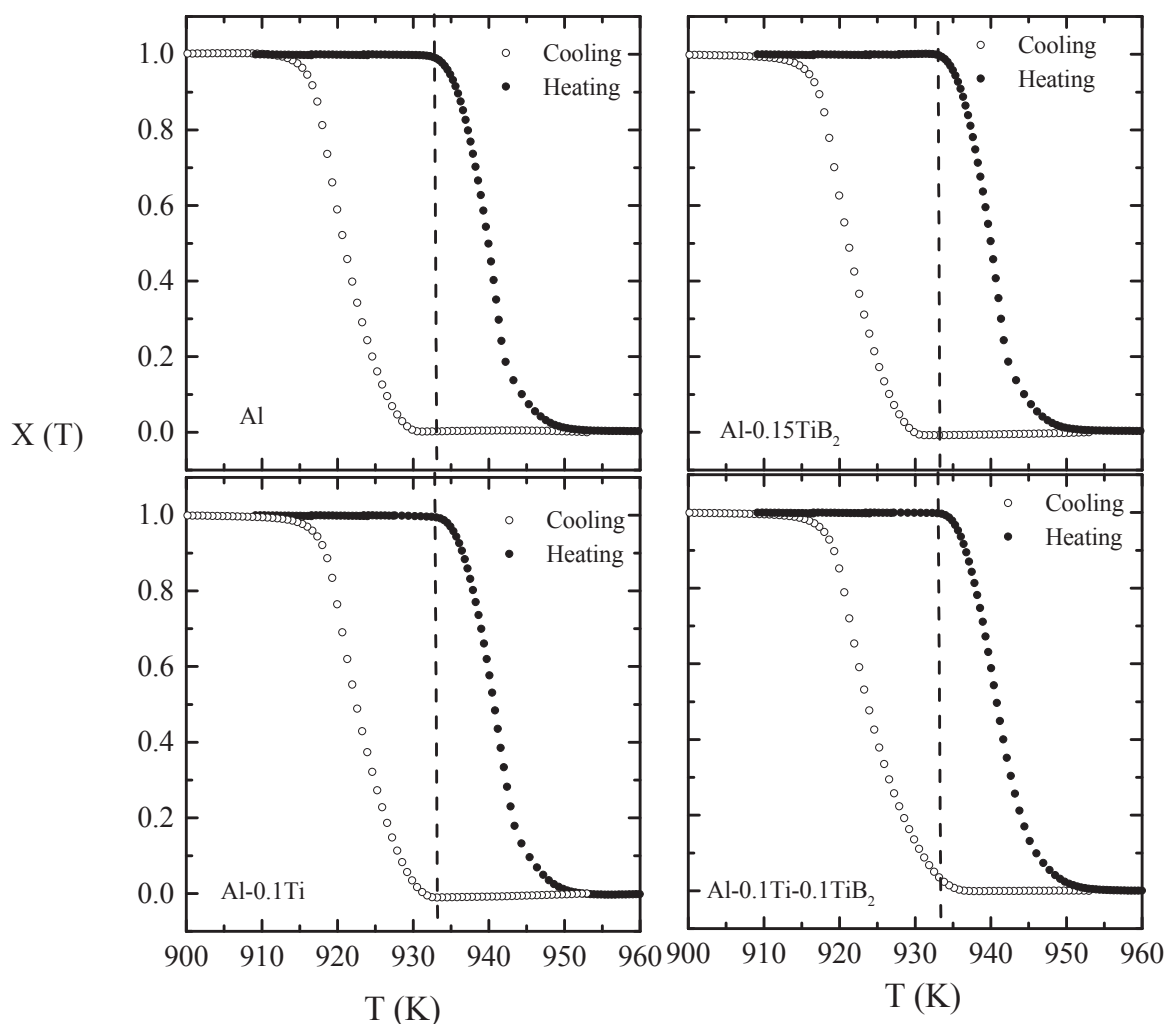


Figure. 5.9 Temperature dependence of the relative crystallinity for pure aluminum, Al-0.15TiB₂, Al-0.1Ti and Al-0.1Ti-0.1TiB₂ alloys as a function of temperature during cooling and heating for a rate of 10 K/min. (The broken line indicates the solidification temperature of pure aluminum at T=933 K).

5.5 Conclusions

We have performed DTA measurements to study the crystallization kinetics of the liquid to solid phase transformation of aluminum alloys, with TiB_2 nucleating particles and solute titanium, separately and both together. These measurements provide important information regarding the mechanism of nucleation and growth during grain refinement. The formation of a $TiAl_3$ phase is observed upon solidification and responsible for grain refinement in hyperperitectic aluminum alloy. The close resemblance in freezing of hyperperitectic and hypoperitectic grain refined aluminum alloys suggest the existence of same mechanism to activate nucleation for both compositions. In addition to presence of grain refiners in aluminum, the release of latent heat appears to be crucial in governing the transformation kinetics during solidification..

Acknowledgements

We are grateful to L. Zhao for assistance in thermodynamical calculations using MTDATA. We are also thankful to N. Geerlofs for providing technical support during DTA measurements. This work was financed in part by the Netherlands Foundation for Fundamental Research of Matter (FOM) and the Netherlands Institute for Metals Research (NIMR).

References

- [1] M. Easton, D. Stjohn, *Met. Mater. Trans. A* 30 (1999) 1613.
- [2] M. Easton, D. Stjohn, *Met. Mater. Trans. A* 30 (1999) 1625.
- [3] A. Cibula, *J. of the institute of Metals* 1951, 80, 1.
- [4] A. Marcantonio, and L. F. Mondolfo, *Metal. Trans.* 971, 2, 465.
- [5] I. Maxwell, and A. Hellawell, *Acta Metal.* 1974, 23, 229.
- [6] L. Backerud, *Light Metal Age.* 1983, 41, 6.
- [7] G. K. Sigworth, *Metal. Trans.* 1984, A15, 277.
- [8] A. L. Greer, A. M. Bunn, A. Tronche, P. V. Evans, and D. Bristow, *J. Acta. Mater.* 2000, 48, 2823.
- [9] P. S. Mohanty and J. E. Gruzleski, *Acta. Metall. Mater.* 43 (1995) 2001.
- [10] P. Schumacher and A. L. Greer, *Mater. Sci. and Engg. A*, 178 (1994) 309

Chapter 6

Solidification of aluminum alloys studied by neutron scattering

6.1 Experimental study of ordering kinetics in aluminum alloys during solidification

N. Iqbal, N. H. van Dijk, V. W. J. Verhoeven, T. Hansen, W. Montfrooij, L. Katgerman, and G. J. Kearley, Acta Mater. 51 (2003) 4497

Abstract

The microscopic structure and crystallization behavior of liquid Al and Al-0.3Ti-0.02B (wt.%) are studied by time-resolved neutron diffraction measurements during the liquid-solid phase transformation for continuous cooling. A specially developed furnace insert was used to obtain a temperature stability of 40 mK in the vicinity of the solidification temperature of $T_0 = 933$ K. The evolution of the static structure factor $S(Q)$ has been monitored during the liquid to solid phase transformation as a function of the cooling rate. The evolution of the liquid fraction f_L during the transformation is determined from the value of the first peak in the liquid structure factor. The evolution of the solid volume fraction $f_S = 1 - f_L$ is analyzed in terms of the Johnson-Mehl-Avrami model. The Avrami exponent n is found to change for pure Al as well as for Al-0.3Ti-0.02B alloy with cooling rate and the rate constant k decreases by an order of magnitude for Al-0.3Ti-0.02B alloy compared to pure Al. Anomalous temporal oscillations were observed in the Bragg-peak intensity of the solid grains during the solidification of the Al-0.3Ti-0.02B alloy.

6.1.1. Introduction

The understanding and control of the microstructure evolution during the liquid to solid phase transformation in aluminum alloys is of major importance in the modern production process of tailor-made aluminum for specific applications. Accurate investigations of the liquid structure near the liquid-solid phase transformation can therefore provide useful information for the influence of the process parameters during the production process, such as cooling rate and the effect of impurities or added particles on the solidification behavior [1-3]. A significant improvement of the mechanical properties of aluminum can be obtained by the addition of small amounts of TiB_2 particles and excess titanium due to a drastic refinement of the average grain size [4,5]. Although the effect of these added grain refiners is extensively studied, the physical mechanism responsible for this grain refinement process is still not well established. It is clear from both experimental and theoretical studies [5] that micron-size TiB_2 particles strongly enhance the nucleation process of solid grains in undercooled melts. The subsequent growth of nuclei is controlled by diffusion of solute titanium and latent heat. A better understanding of

the effects of solute titanium and added TiB_2 particles in the liquid-solid phase transformation of aluminum alloys is therefore highly desirable.

In the present paper we report on time-dependent neutron diffraction measurements on the microstructure evolution of pure aluminum and Al-0.3Ti-0.02B (wt.%) alloy during the crystallization process for different continuous cooling rates.

6.1.2 Experimental

The samples used in this study were 99.999 % pure aluminum (Goodfellows) and an Al-0.3Ti-0.02B (wt.%) alloy prepared from an Al-5Ti-0.2B (wt.%) commercial master alloy (KBM AFFILIPS). The particle size distribution of TiB_2 precipitates in the Al-0.3Ti-0.02B alloy was determined by optical microscopy and showed a particle size distribution in the range from 0.6 to 2.2 μm with a maximum around 1.2 μm . The pure aluminum and Al-0.3Ti-0.02B alloy samples with a mass of 10.6 g were placed in a cylindrical single-crystalline sapphire container with a height of 60 mm, an inner diameter of 10 mm, and a wall thickness of 1 mm.

The in-situ neutron diffraction measurements were performed on the high-flux powder diffractometer D20 at the Institute Laue-Langevin (ILL) following a feasibility study on the disordered materials diffractometer SLAD at the Studsvik Neutron Research Laboratory (NFL). A monochromatic neutron beam with wavelength of $\lambda = 0.82 \text{ \AA}$ and a beam height of 45 mm was used for all neutron diffraction experiments. For the high-temperature neutron diffraction measurements a dedicated vacuum furnace (7×10^{-4} mbar) was used with a vanadium heater element and a temperature stability of about 1 K.

In order to achieve the required temperature stability ($\Delta T < 50 \text{ mK}$) for our solidification experiments the specially designed furnace insert of Fig. 6.1 was used.

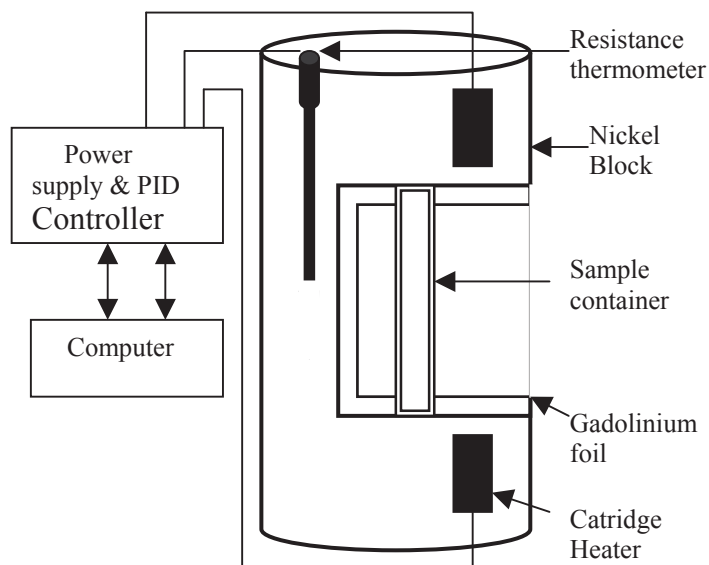


Figure 6.1 Furnace insert and temperature control system for the high-stability temperature regulation close to the melting point.

The furnace insert consisted of a nickel cylinder with a mass of 884 g, a height of 144 mm, and a diameter of 37 mm. The mass of the insert effectively dampens the temperature fluctuations of the main furnace and strongly improves the temperature stability. In the central part of the furnace insert a section has been cut out in order to allow a free passage of the incoming and scattered neutrons from the sample. The walls of the nickel block around the sample were covered by gadolinium in order to prevent secondary scattering. Two cartridge heaters were placed into the top and bottom part of the nickel block in order to regulate the temperature of the insert with an additional PID controller (Lake Shore model 340). The temperature of the furnace insert was monitored by a PT100 platinum resistance thermometer. By operating the main furnace in constant power mode and regulating the temperature of the furnace insert, a temperature stability of about $\Delta T \approx 40$ mK was obtained at a temperature of $T = 933$ K. The thermal response time of the furnace insert was estimated at $\tau_{\text{ins}} \sim 2$ min. For our sample geometry the expected time constant for thermal equilibrium of the sample is estimated at $\tau_{\text{sam}} \approx 5$ min.

6.1.3 Results and discussion

6.1.3.1 Liquid structure factor

In Fig. 6.2 the measured liquid structure factor $S(Q)$ as a function of the wave-vector transfer Q is shown for pure aluminum and Al-0.3Ti-0.02B alloy at a temperature of $T = 936$ K ($T > T_0$). The first peak in the liquid structure factor of pure aluminum is observed at $Q = 2.68 \text{ \AA}^{-1}$ and has a height of $S(Q) = 2.44$.

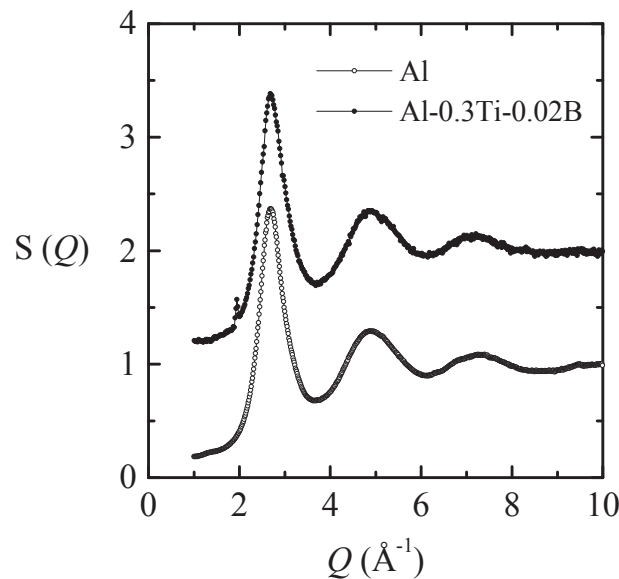


Figure 6.2 Liquid structure factor $S(Q)$ as a function of the wave-vector transfer Q for pure aluminum (open circles) and Al-0.3Ti-0.02B alloy (solid circles) at a temperature of $T = 936$ K. For clarity $S(Q)$ of the Al-0.3Ti-0.02B alloy is vertically displaced by 1.

The observed structure factor is in reasonable agreement with previous neutron [6,7] and X-ray diffraction [8,9] studies of liquid aluminum in the vicinity of the solidification temperature. The measured structure factor of liquid Al-0.3Ti-0.02B alloy closely resembles the curve of pure aluminum indicating a weak influence of the alloying elements on the short-range order in the liquid. The main difference is observed in the vicinity of the first peak in the liquid structure factor. Although no significant shift in the position is observed, the height is somewhat reduced to a value of $S(Q) = 2.39$. In addition, a small peak in the structure factor of Al-0.3Ti-0.02B alloy is observed below the first liquid peak. This additional peak at $Q = 1.95 \text{ \AA}^{-1}$ corresponds to a (001) Bragg reflection of the solid TiB_2 particles with a hexagonal crystal lattice structure in the liquid alloy.

6.1.3.2 Liquid volume fraction

In order to study the influence of grain refiners on the crystallization behavior of aluminum systematic time-dependent neutron diffraction measurements of the structure factor in pure aluminum and Al-0.3Ti-0.02B alloy were performed. For each of the measurements the sample was heated to a temperature of 943 K for one hour to obtain a homogeneous liquid phase, followed by a continuous cooling with rates of 0.06 and 0.6 K/min. During the continuous cooling the structure factor was continuously monitored by neutron diffraction in time steps of 1 min. During the liquid to solid phase transformation the liquid peaks in the structure factor (Fig. 6.2) gradually decrease while Bragg peaks from the solid phase emerge and grow. As the observed Bragg peak intensity strongly depends on texture in the solid phase, we use scattering from the liquid phase to determine the liquid and solid volume fractions.

Fig. 6.3 shows the behavior of liquid volume fraction of pure aluminum as a function of temperature for cooling rates of 0.06 and 0.6 K/min determined from the normalized variation in the structure factor $S(Q)$ at the maximum of the first liquid peak at $Q = 2.68 \text{ \AA}^{-1}$. For both cooling rates the transformation starts at an undercooling of about 10 K compared to the thermodynamic solidification temperature of $T_0 = 933 \text{ K}$. For a higher cooling rate the transformation however, extends over a wider temperature range. As a consequence, the temperature where half of the liquid volume of pure aluminum is transformed to solid ($T_{1/2}$) decreases by 4 K for a tenfold increase in the cooling rate.

In Fig. 6.4 the liquid volume fraction of the Al-0.3Ti-0.02B alloy is shown as a function of temperature for cooling rates of 0.06 and 0.6 K/min. Again the transformation start temperature is relatively insensitive to the cooling rate, but the transformation extends to lower temperatures at a higher cooling rate. Compared to the pure aluminum sample the liquid/solid phase transformation of the Al-0.3Ti-0.02B alloy occurs over a wider temperature range regardless of the cooling rate. In Table 1 a summary of the experimental transformation temperatures as a function of cooling rate is given for both samples.

As expected for a phase transformation that involves latent heat, the melting/freezing transition exhibits thermal hysteresis [10]. In Fig. 6.5 this thermal hysteresis is clearly demonstrated in the combined heating and cooling experiments on the liquid volume fraction of the Al-0.3Ti-0.02B alloy for a heating/cooling rate of 0.6 K/min. The thermal hysteresis of the temperatures halfway the transformation is $\Delta T_{1/2} = 27 \text{ K}$. The corresponding hysteresis in time amounts to $\Delta t_{1/2} = 45 \text{ min}$, which is far too large to be caused by a weak thermal link between furnace insert and the

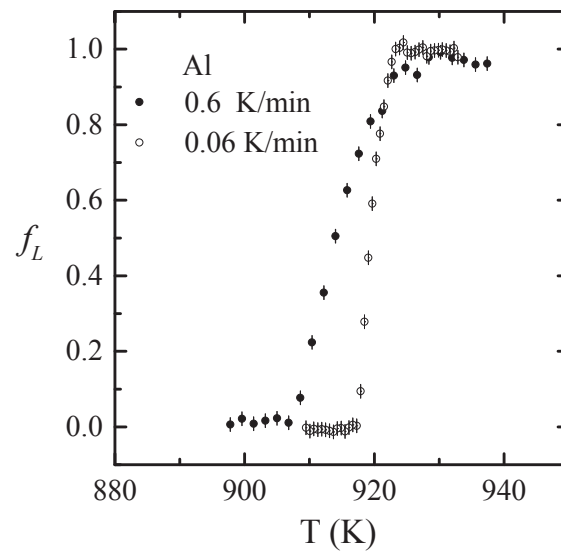


Figure 6.3 Liquid volume fraction f_L of pure aluminum as a function of temperature for cooling rates of 0.06 K/min (open circles) and 0.6 K/min (solid circles). The liquid volume fraction f_L is deduced from the normalized variation in the first liquid peak in $S(Q)$ at $Q = 2.68 \text{ \AA}^{-1}$.

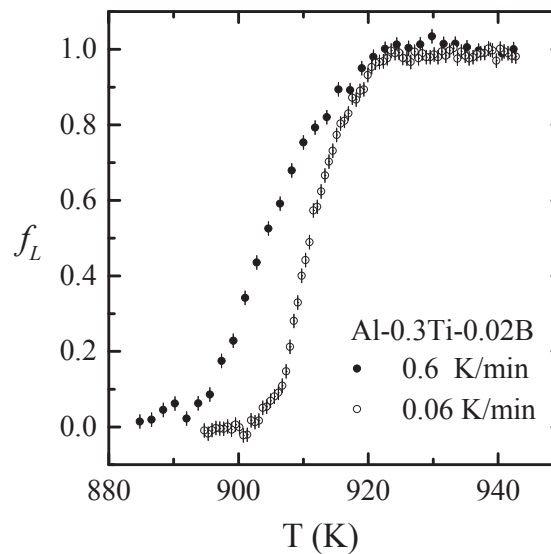


Figure 6.4 Liquid volume fraction f_L of Al-0.3Ti-0.02B alloy as a function of temperature for cooling rates of 0.06 K/min (open circles) and 0.6 K/min (solid circles). The liquid volume fraction f_L is deduced from the normalized variation in the first liquid peak in $S(Q)$ at $Q = 2.68 \text{ \AA}^{-1}$.

sample for these low cooling rates as estimated response time of the sample amounts to $\tau_{\text{sam}} \approx 5$ min.

Table 6.1. Transformation temperatures of pure aluminum and Al-0.3Ti-0.02B alloy at two different cooling rates, where T_s is the transformation start temperature, T_f the transformation finish temperature, $T_{1/2}$ the temperature halfway the transformation. In addition, the temperature width of the transformation $\Delta T = T_s - T_f$ and the average undercooling $T_0 - T_{1/2}$ with respect to the crystallization temperature of $T_0 = 933$ K are listed.

Sample	Cooling rate (K/min)	T_s (K)	T_f (K)	$T_{1/2}$ (K)	ΔT (K)	$T_0 - T_{1/2}$ (K)
Al	0.06	923	918	918	5	15
	0.60	925	907	914	18	19
Al-0.3Ti-0.02B	0.06	923	904	911	19	22
	0.60	923	894	905	29	28

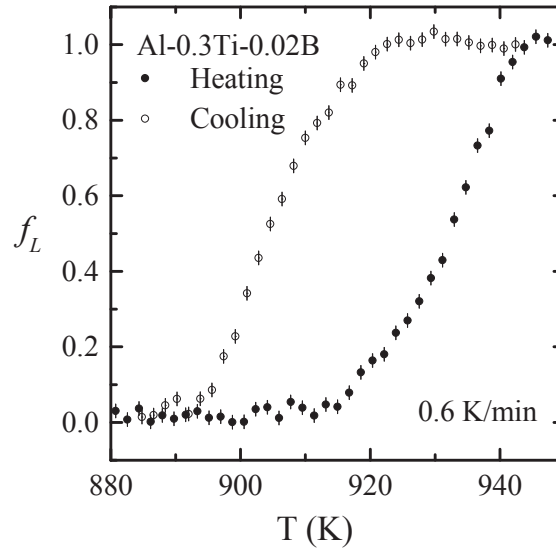


Figure 6.5 Liquid volume fraction f_L of Al-0.3Ti-0.02B alloy as a function of temperature for cooling (open circles) and heating (solid circles) at a cooling rate of 0.6 K/min. The liquid volume fraction f_L is deduced from the normalized variation in the first liquid peak in $S(Q)$ at $Q = 2.68 \text{ \AA}^{-1}$.

6.1.3.3 Transformation kinetics

The Johnson-Mehl-Avrami (JMA) model [11-14] has been widely used to describe the kinetics of isothermal phase transformations with examples in glasses [15,16], gels [17,18], polymers [19], steels [20], and metal alloys [21,22]. According to this model the fraction transformed f as a function of time t is described by the JMA equation:

$$f(t) = 1 - \exp\{-k(t - t_0)^n\}, \quad (6.1)$$

where k is the rate constant, t_0 is the incubation time, and n the Avrami exponent. The value of the exponent n is expected to vary between 1 and 4 depending on the nucleation mechanism and the growth dimensionality [23]. For continuous cooling the transformation time t in the JMA equation can be set to zero at the time the temperature falls below the crystallization temperature $T_0 = 933$ K [19]. Under the assumption that the transformation kinetics depend purely on the transformation time and independent of temperature, we can now fit the experimental data to the JMA model of Eq. (1). Provided that there is no change in the nucleation and growth mechanism during the phase transformation, the Avrami exponent n is expected to be constant [24].

In Figs. 6.6 and 6.7 the solid volume fraction $f_s(t)$, deduced from the liquid fraction $f_L(t)$, is shown as a function of time for pure aluminum and Al-0.3Ti-0.02B alloy for cooling rates of 0.06 and 0.6 K/min. The results of a fit of the JMA equation to the experimental data are listed in Table 6.2. The corresponding fitting curves are shown in Figs. 6.6 and 6.7.

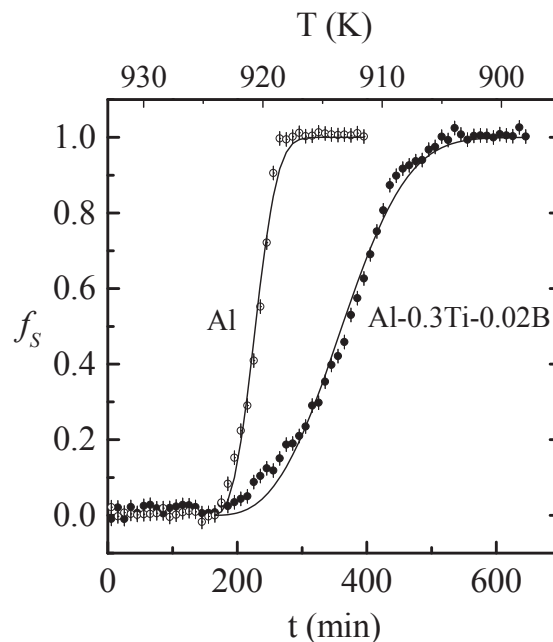


Figure 6.6 Time evolution of the solid volume fraction $f_s = 1 - f_L$ for pure aluminum (open circles) and Al-0.3Ti-0.02B alloy (solid circles) at a cooling rate of 0.06 K/min. The solid line indicates a fit to the data with the Johnson-Mehl-Avrami model (see text).

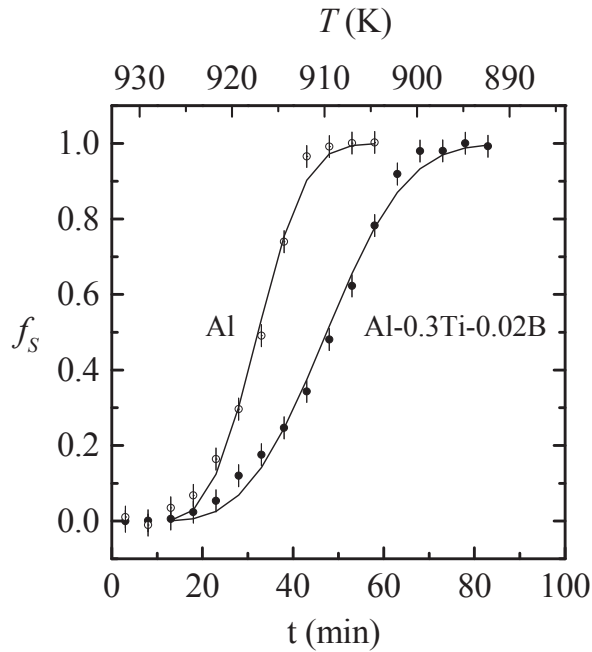


Figure 6.7 Time evolution of the solid volume fraction $f_s = 1 - f_L$ for pure aluminum (open circles) and Al-0.3Ti-0.02B alloy (solid circles) at a cooling rate of 0.6 K/min. The solid line indicates a fit to the data with the Jonson-Mehl-Avrami model (see text).

For the Al-0.3Ti-0.02B alloy fitting resulted in values of $n = 2.7$ and 3.1 for cooling rates of 0.06 and 0.6 K/min respectively. For pure aluminum values $n = 2.9$ and 3.1 were obtained for cooling rates of 0.06 and 0.6 K/min, respectively. The rate constant, k , of the Al-0.3Ti-0.02B alloy is decreased by an order of magnitude compared to that of pure aluminum. The presence of grain refiners in the Al-0.3Ti-0.02B alloy promotes nucleation on the micron-sized substrate particles and the presence of excess titanium in the aluminum melt of the Al-0.3Ti-0.02B alloy is expected to reduce the growth rate of the crystallites with respect to pure aluminum. Our observations are in qualitative agreement with the expected behavior of the rate constant k . The observed value of $t_{1/2}$ for pure aluminum is lower than that of Al-0.3Ti-0.02B alloy for both cooling rates confirming the relatively slow growth in Al-0.3Ti-0.02B alloy.

Table 6.2. Transformation parameters of pure aluminum and Al-0.3Ti-0.02B alloy at two different cooling rates obtained from a fit of the experimental liquid volume fraction to the JMA model, where n is the Avrami exponent, k is the rate constant, t_0 is the transformation start time, and $t_{1/2} - t_0 = [\ln(2)/k]^{1/n}$ is the time halfway the transformation after the start of the transformation. The time when the temperature falls below the crystallization temperature $T_0 = 933$ K is chosen as $t = 0$.

Sample	Cooling rate (K/min)	n	k (min^{-n})	t_0 (min)	$t_{1/2} - t_0$ (min)
Al	0.06	2.9(3)	$3.3(4) \times 10^{-6}$	160	67.6
	0.60	3.1(0)	$5.0(5) \times 10^{-5}$	10	21.9
Al-0.3Ti-0.02B	0.06	2.7(0)	$5.0(4) \times 10^{-7}$	160	197.4
	0.60	3.1(0)	$9.1(2) \times 10^{-6}$	10	37.4

6.1.3.4 Growth oscillations

During the measurements of the transition kinetics of the crystallization in the Al-0.3Ti-0.02B alloy unexpected variations in the Bragg peak intensity from the crystallites were observed as a function of time. This behavior is demonstrated in Fig. 6.8 where the normalized Bragg peak intensity of the (111), (200), (220), and (311) reflections are shown for a continuous cooling at a rate of 0.06 K/min. For comparison the corresponding solid fraction $f_S = 1 - f_L$ calculated from first liquid peak in $S(Q)$ is shown as a function of time. The observed variations in the Bragg peak intensity are found to be less pronounced for the higher cooling rate of 0.6 K/min. From Fig. 6.8 it is clear that no correlation in the Bragg peak intensity of the different reflections is observed. In fact, the oscillations are observed only in the Bragg peak intensity of the crystal reflections and not in the solid volume fraction, which shows a continuous increase. This behavior has not been seen in successive measurements on pure aluminum.

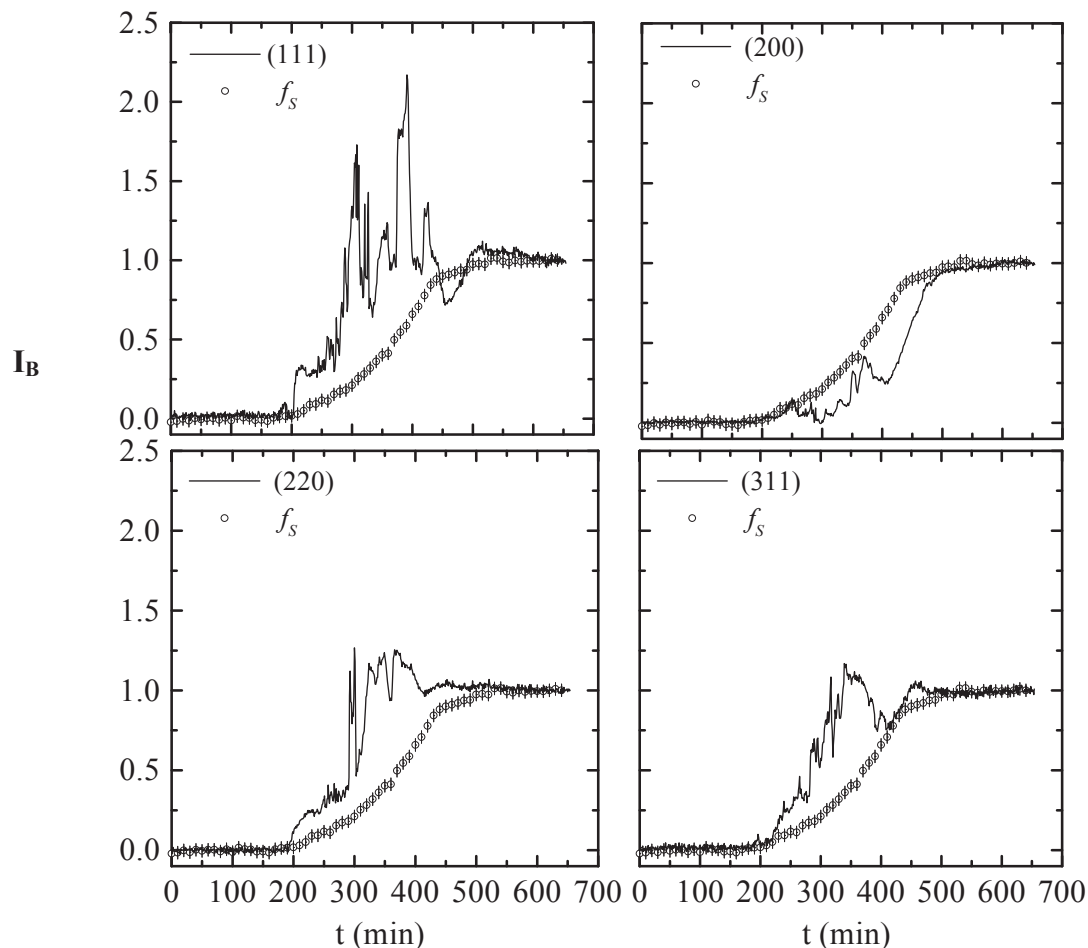


Figure 6.8 Normalized integrated Bragg peak intensity I_B for the (111), (200), (220), and (311) reflections of fcc aluminum of Al-0.3Ti-0.02B alloy as a function of the time t for a cooling rate of 0.06 K/min. For comparison the time evolution of the solid volume fraction $f_S = 1 - f_L$ deduced from the variation in the first liquid peak in $S(Q)$ is shown. The temporal fluctuations observed in the Bragg peak intensities of the grains are not reflected in the volume fraction of the solid phase.

The observed oscillatory behavior cannot be due to mechanical vibrations of the sample cell or to fluctuations in the sample temperature, which is controlled to within 40 mK. It is probable, that the fluctuations observed in the Bragg peak intensity are intrinsic to the growth kinetics of the crystallites in the Al-0.3Ti-0.02B alloy itself. One interpretation of these observations is that the crystal growth in the Al-0.3Ti-0.02B alloy is diffusion limited due to the latent heat released by the crystallization. The subsequent increase in the local sample temperature is expected to have a strong effect on the growth rate (recalescence).

In the absence of a true powder average, the fluctuations in Bragg peak intensity may however, also be due to a random motion of individual crystallites. For rotating crystallites the reflection condition in the scattering plane of the detector is only fulfilled for short periods of time. This interpretation seems unlikely given the quasi-periodic nature of oscillations. Also the relative size of the oscillations seems too large for the expected number of grains in reflection. For an illuminated sample volume of about 3 cm³ and a final grain diameter of about 500 μm the number of crystallites present during the transformation is of the order of 5×10^4 . From the size of the (111) Bragg-peak intensity relative to the main liquid peak an average number of $N \approx 300$ grains was estimated to be in reflection for a cooling rate of 0.06 K/min. As a result the relative fluctuations in Bragg intensity are expected to be of the order of $1/\sqrt{N} \approx 6\%$, which is much smaller than the observed oscillations.

6.1.4 Conclusions

The paper presents the structural and kinetic features of the crystallization kinetics in pure aluminum and an Al-0.3Ti-0.02B alloy with TiB₂ grain refiners. The results can be summarized as follows:

- (1) The short-range order in pure aluminum and Al-0.3Ti-0.02B alloy is continuous at the freezing transition. The transformation process is spread over several degrees in temperature. The dynamic freezing range was observed to increase with the addition of nucleating agents.
- (2) The kinetics of the liquid to solid phase transformation is found to be strongly dependent on the presence of TiB₂ grain refiners and the excess titanium. For Al-0.3Ti-0.02B alloy grain growth is three-dimensional and the growth rate is observed to decrease by an order of magnitude compared to the growth rate observed for pure aluminum.
- (3) Although the liquid fraction varies continuously during solidification, the Bragg peak intensity of the crystal reflections shows remarkable temporal fluctuations for the Al-0.3Ti-0.02B alloy. This phenomenon appears to be intrinsic to the material under study.

Acknowledgements

We thank R. Delaplane and R. McGreevy for their assistance during the preliminary measurements at the Studsvik Neutron Research Laboratory. The Institute Laue-Langevin is gratefully acknowledged for the beam time to perform these neutron diffraction experiments. We thank P. van der Ende for the design of the furnace insert. This work was financed in part by the Netherlands Foundation for Fundamental Research of Matter (FOM) and the Netherlands Institute for Metals Research (NIMR).

References

- [1] Shannon, R. F., Glavicic, M. G., and Singh, M. A., *J. Macromol. Sci.* 1994, B33, 357.
- [2] Allen, C. M., O'Reilly, K. A. Q., Cantor, B. and Evans, P. V., *Mat. Sci. Eng.* 1997, A226-228, 784.
- [3] Xing, L. Q., Hufnagel, T. C., Eckert, J., Loser, W. and Schulz, L. *Appl. Phys. Lett.* 2000, 77, 1970.
- [4] Cisse, J., Kerr, H. W., and Bolling, G. F. *Metal. Trans.* 1974, 5, 633.
- [5] Easton, M. and Stjohn, D. *Met. Mater. Trans.* 1999, A30, 1625.
- [6] Takeda, S., Kawakita, Y., Inu, M., Maruyama, K., Tamaki, S. and Waseda, Y. *J. Non-Crys. Sol.* 1996, 205-207, 365.
- [7] Takeda, S., Harada, S., Tamaki, S. and Waseda, Y. *J. Phys. Soc. Jpn.* 1991, 60, 2241.
- [8] Waseda, Y. *The structure of Non-Crystalline Materials*, (McGraw-Hill, New York, 1980).
- [9] IAMP database of SCM-LIQ, Tohoku University.
URL: <http://www.iamp.tohoku.ac.jp/database/scm/LIQ/sq.html>
- [10] Herhold, A. B., King, H. E. and Sirota, E. B. *J. Chem. Phys.* 2002, 116, 9036.
- [11] Johnson, J. and Mehl, R. *Trans. A.I.M.E.* 1939, 135, 416.
- [12] Avrami, M. *J. Chem. Phys.* 1939, 7, 1103.
- [13] Avrami, M. *J. Chem. Phys.* 1940, 8, 212.
- [14] Avrami, M. *J. Chem. Phys.* 1941, 9, 177.
- [15] Sung, Y. M. and Kim, S. *J. Mater. Sci.* 2000, 35, 4293.
- [16] Gualtieri, A. F., Mazzucato, E., Tang, C. C. and Cernik, R. *J. Mater. Sci. Forum*, 2000, 312, 224.
- [17] Fogg, A. M., Price, S. J., Francis, J. J., O'Brien, S. and O'Hare, D. *J. Mater. Chem.* 2000, 10, 2355.
- [18] Malek, J. *Thermochem. Acta* 2000, 355, 239.
- [19] Supaphol, P. *J. Appl. Pol. Sci.* 2000, 78, 338.
- [20] Louzguine, D. V. and Inoue, A. *J. Mater. Sci.* 2000, 35, 4159.
- [21] Lee, J. K., Choi, G., Kim, D. H. and Kim, W. T. *Appl. Phys. Lett.* 2000, 77, 978.
- [22] Imbert, C. A. C. and MacQueen, H. J. *Mater. Sci. Technol.* 2000, 16, 532.
- [23] Henderson, D. W. *J. Thermal. Anal.* 1979, 15, 325.
- [24] Porter, D. A. and Easterling, k. E. *Phase Transformation in Metals and Alloys* (Champan & Hall, London, 1993)

6.2 Periodic structural fluctuations during the solidification of aluminum alloys studied by neutron diffraction

N. Iqbal, N. H. van Dijk, V. W. J. Verhoeven, T. Hansen, L. Katgerman, and G. J. Kearley; Materials Science and Eng. A 367 (2004) 82

Abstract

Time-resolved neutron diffraction measurements have been carried out to study the crystallization dynamics during the liquid-solid phase transformation in an Al-0.3Ti-0.02B (wt.%) alloy. Starting from the liquid phase, the temperature was reduced to below the thermodynamic transition temperature of $T_0 = 933$ K by continuous cooling at rates of 0.6 and 0.06 K/min and by step-wise cooling in temperature steps of 1 K. After nucleation of the solid phase on the micron-size TiB_2 particles in the liquid alloy, pronounced fluctuations in the Bragg peak intensity of the growing crystallites are observed during solidification. These fluctuations have been analyzed by a time correlation function to extract the frequency and correlation time of the fluctuations. The deduced correlation time and oscillation frequency strongly depend on the cooling rate. The correlation time increases and the oscillation frequency decreases for decreasing cooling rate. For step-wise cooling a monotonic increase in correlation time is observed for decreasing temperatures demonstrating a slowdown of the dynamics during the liquid to solid phase transformation.

6.2.1 Introduction

The understanding and control of the microscopic structure evolution during the liquid to solid phase transformation in aluminum alloys is of major importance in the modern production process of tailor-made aluminum for specific applications. Accurate investigations of the liquid structure in the neighborhood of liquid-solid phase transformation can provide useful information about the influence of the process parameters on the solidification behavior during the production process, such as cooling rate and the effect of impurities or added particles [1,2]. A significant improvement of the mechanical properties of aluminum can be obtained by the addition of small amounts of TiB_2 particles and excess titanium due to a drastic refinement of the average grain size [3]. The micrometer size TiB_2 particles enhance the nucleation rate of solid grains below the solidification temperature. The subsequent growth of nuclei is controlled by the diffusion of solute excess titanium and latent heat. A better understanding of the effects of solute titanium and added TiB_2 particles on the liquid-solid phase transformation of aluminum alloys is therefore highly desirable.

The present paper describes the neutron diffraction measurements on the temporal fluctuations in the evolution of Bragg-peak intensity during the solidification of an Al-0.3Ti-0.02B (wt.%) alloy for cooling rates of 0.06 and 0.6 K/min and for step-wise cooling. The corresponding atomic composition of this system is Al-0.16Ti-0.05B (at.%). Preliminary kinetic results of liquid structure factor and the evolution of the solid phase fraction during liquid-solid phase transformation of the same alloy have been reported elsewhere [4]. The observed temporal fluctuations can be the consequence of the ripening process between the evolving crystals in the liquid that ultimately controls the growth kinetics of these crystals. The frequency and correlation times of these temporal fluctuations during the liquid-solid phase

transformation are investigated in order to obtain information on the influence of added grain refining particles on the ordering process during solidification.

6.2.2 Experimental

The sample used in this study was an Al-0.3Ti-0.02B (wt.%) alloy prepared from an Al-5Ti-0.2B (wt.%) commercial master alloy (KBM AFFILIPS). The particle size distribution of the TiB₂ precipitates in the Al-0.3Ti-0.02B alloy was determined by optical microscopy and showed particle sizes in the range from 0.6 to 2.2 μm with a maximum around 1.2 μm. The Al-0.3Ti-0.02B alloy sample with a mass of 10.6 g was placed in a cylindrical single-crystalline sapphire container with a height of 60 mm, an inner diameter of 10 mm, and a wall thickness of 1 mm.

The in-situ neutron diffraction measurements were performed on the high-flux powder diffractometer D20 at the Institute Laue-Langevin (ILL). A neutron beam with a wavelength of $\lambda = 0.82 \text{ \AA}$ and a beam height of 41 mm was used for all neutron diffraction experiments. For the high-temperature neutron diffraction measurements a dedicated vacuum furnace (7×10^{-4} mbar) was used with a vanadium heater element and a temperature stability of about 1 K. The required temperature stability ($\Delta T < 40$ mK) for our experiments was achieved with a specially designed furnace insert [4].

In order to study the solidification process of the liquid aluminum alloy three thermal treatments of Fig. 6.9 were applied.

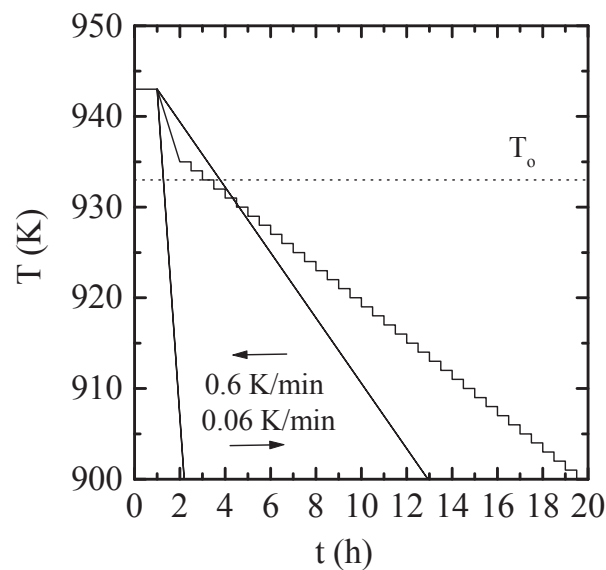


Figure 6.9 Temperature profiles for solidification experiments for Al-0.3Ti-0.02B alloy with cooling rate of 0.06 and 0.6 K/min and with step-wise cooling.

In all cases the Al-0.3Ti-0.02B alloy was heated to a temperature of $T = 943 \text{ K}$ for one hour to obtain a homogenous liquid phase. Subsequently, the temperature was lowered to below the thermodynamic solidification temperature of $T_0 = 933 \text{ K}$ by continuous cooling with rates of 0.6 and 0.06 K/min and by step-wise cooling. For continuous cooling the variations in the measured structure factor were monitored in time steps of 1 min. For step-wise cooling the temperature was lowered to $T = 935 \text{ K}$

followed by a series of temperature steps of 1 K. The structure factor was monitored in time steps of 30 s during a period of 30 min at each temperature.

6.2.3 Results

6.2.3.1 Structure

Fig. 6.10 shows the measured structure factor $S(Q)$ of the Al-0.3Ti-0.02B alloy in the pure liquid and pure solid state. Where $Q = (4\pi/\lambda) \sin(\theta)$ is the wave vector transfer with 2θ as the scattering angle, and λ is the neutron wavelength. The intensity of the solid phase is scaled to the maximum intensity of 111 Bragg peak. The first peak in the liquid structure factor of Al-0.3Ti-0.02B alloy is observed at $Q = 2.68 \text{ \AA}^{-1}$ and has a height of $S(Q) = 2.39$. In addition, a small peak in the liquid structure factor of the Al-0.3Ti-0.02B alloy is observed below the first liquid peak. This additional peak at $Q = 1.95 \text{ \AA}^{-1}$ corresponds to a 001 Bragg reflection of the solid TiB_2 particles with a hexagonal crystal lattice structure in the liquid alloy. During the liquid to solid phase transformation, the liquid peaks in the structure factor gradually decrease while the Bragg peaks from the solid phase with a face-centered cubic lattice structure ($a=4.14 \text{ \AA}$) emerge. The observed relative Bragg peak intensities deviate significantly from the expected powder average indicating the presence of texture.

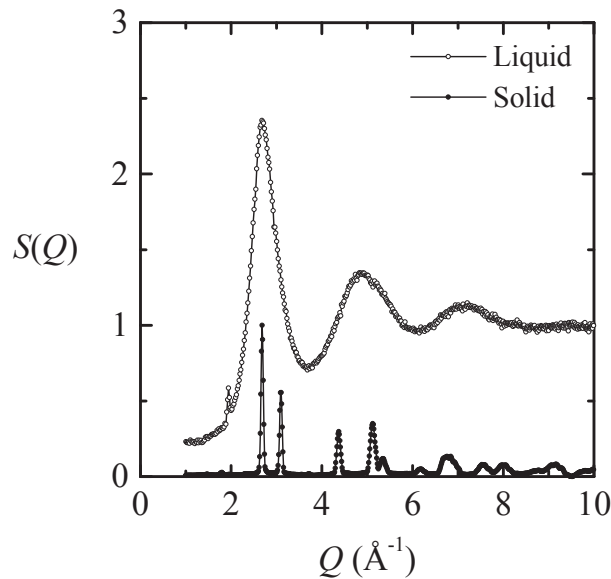


Figure 6.10 Structure factor of the Al-0.3Ti-0.02B alloy, in the liquid (open circles) and in the solid state (solid circles).

In the following discussion the height of the first liquid peak at $Q = 2.68 \text{ \AA}^{-1}$ is used to deduce the value of liquid phase fraction f_L and the corresponding value of solid fraction $f_S = 1 - f_L$. During liquid to solid phase transformation the change in solid fraction f_S is deduced from the normalized variation in the height of first peak in the liquid structure factor $S(Q)$. As the position and the width of the first liquid peak does not change significantly during solidification, this is equivalent to an integration over the first liquid peak. Such an integration would however require a separation of the

contributions of the liquid and the solid phase to the structure factor and is therefore more sensitive to systematic errors.

6.2.3.2 Solidification kinetics

In Fig. 6.11 the solid fraction f_S is compared to the relative variation in the monitored Bragg reflections of the solid phase I_B during the continuous cooling of the Al-0.3Ti-0.02B alloy at a rate of 0.06 K/min. The transformation kinetics of the solid-phase fraction as a function of the cooling rate is discussed in detail in [4]. During the transformation of the Al-0.3Ti-0.02B alloy a remarkable oscillatory growth of Bragg peak intensity is observed for the integrated intensity of the 111, 200, and 311 reflections. It is interesting to note that the oscillations are observed only in the Bragg-peak intensity and not in the solid volume-fraction. Further, there is no direct correlation observed in the fluctuations between the Bragg intensity of the monitored reflections. This oscillatory behavior of Bragg-peak intensity appears to be intrinsic to the material under study.

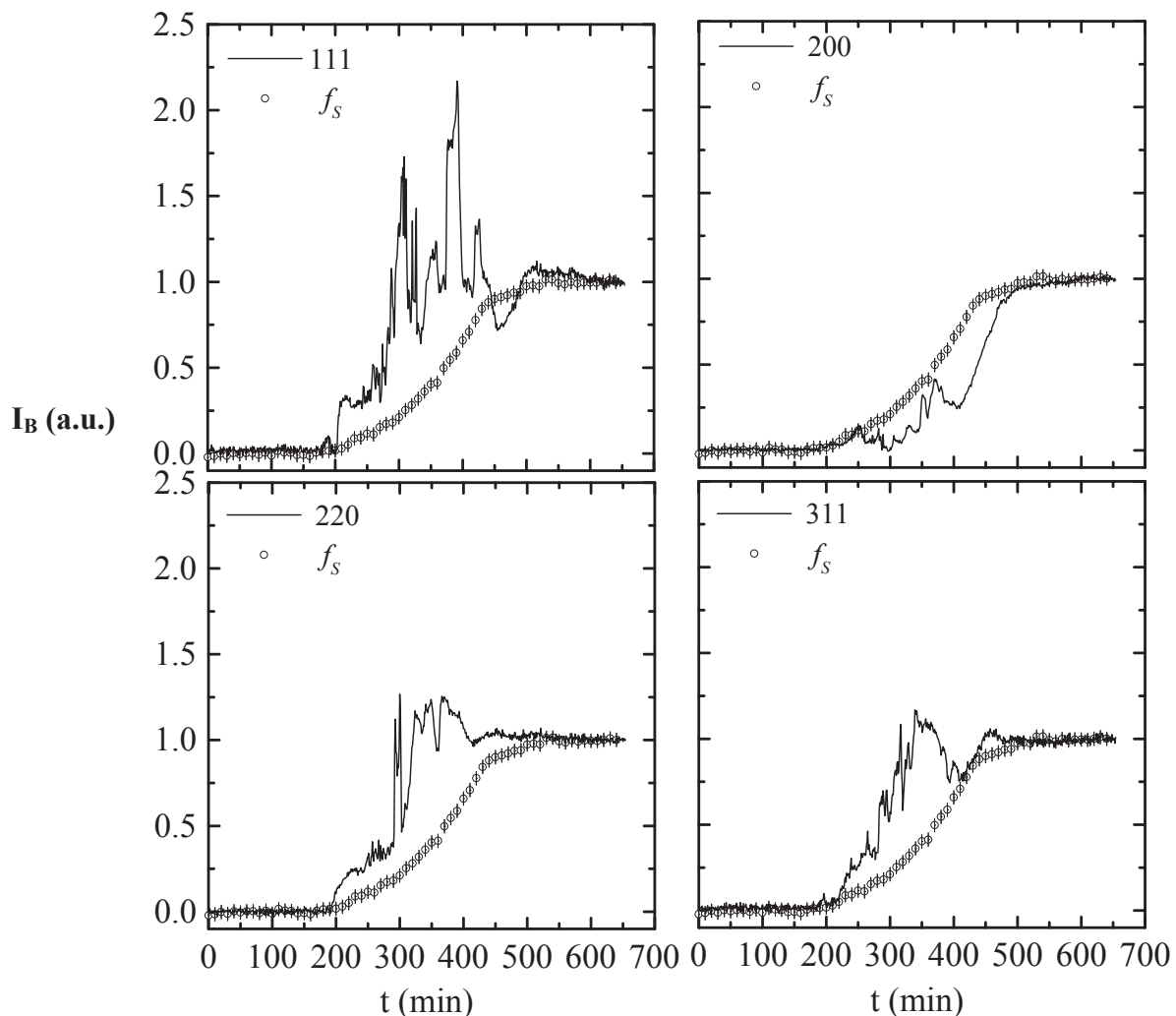


Figure 6.11 Time evolution of the normalized intensities of the main Bragg peaks for the Al-0.3Ti-0.02B alloy (solid line) and solid fraction $f_S = 1 - f_L$ (open circles) at a cooling rate of 0.06 K/min.

In Fig. 6.12 the intensity evolution of Bragg peaks and the corresponding solid fraction f_S is shown for a continuous cooling rate of 0.6 K/min. Again the evolution of the Bragg-peak intensity shows an oscillatory behavior. As expected, the oscillations observed at a cooling rate of 0.6 K/min are however, less pronounced than for the cooling rate of 0.06 K/min.

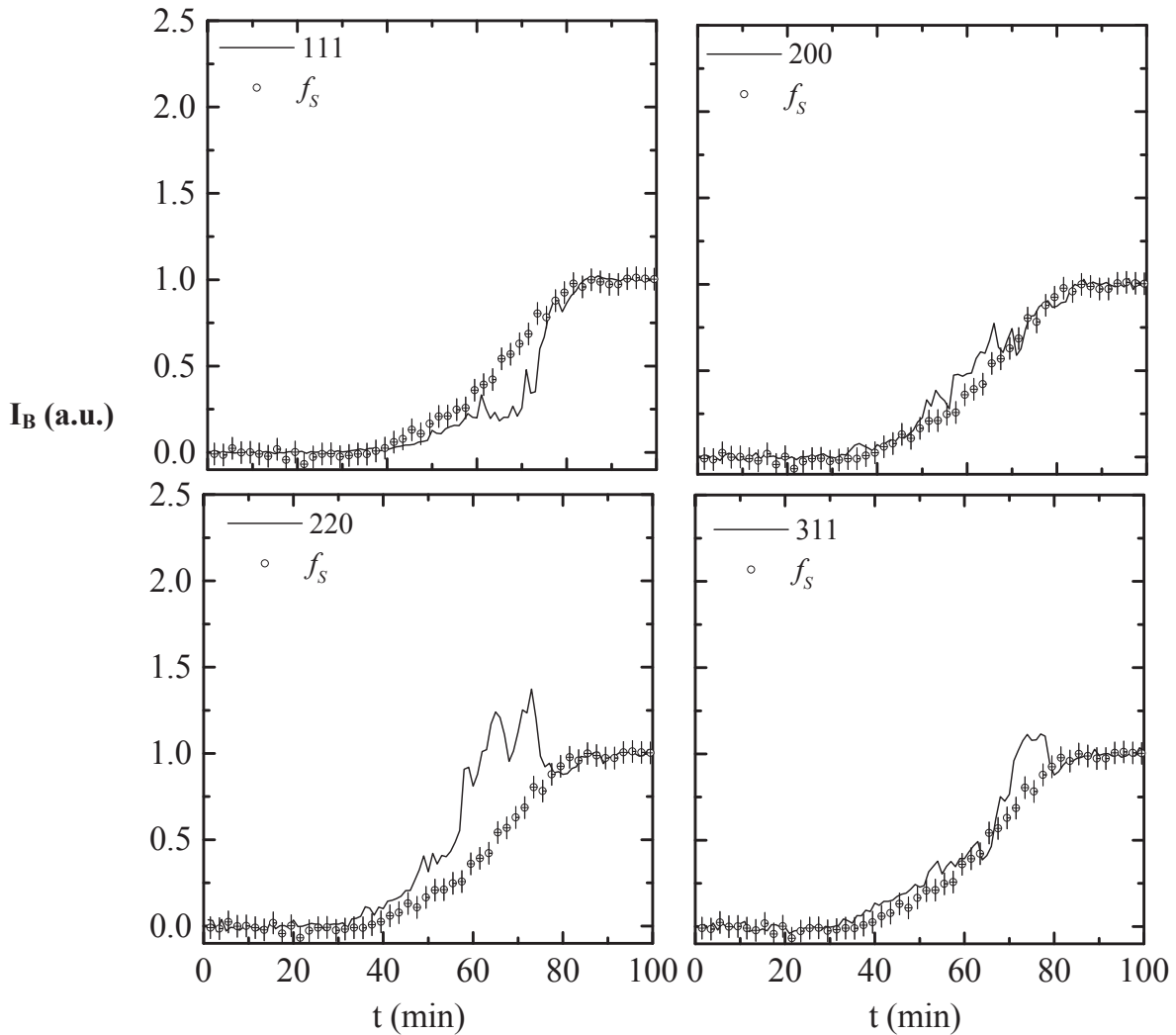


Figure 6.12 Time evolution of the normalized intensities of the main Bragg peaks for the Al-0.3Ti-0.02B alloy (solid line) and solid fraction $f_S = 1 - f_L$ (open circles) at a cooling rate of 0.6 K/min.

6.2.4 Discussion

In order to study the kinetics of the solidification process the Johnson-Mehl-Avrami (JMA) model [5-8] is applied. According to the JMA model the functional form for the ordered volume fraction $f(t)$ as a function of time t is predicted to be

$$f(t) = 1 - \exp\{-k(t - t_0)^n\}, \quad (6.2)$$

where k is the rate constant, t_0 is the incubation time, and n the Avrami exponent. The value of the exponent n is expected to vary between 1 and 4 depending on the nucleation mechanism and the growth dimensionality [9]. In Fig. 6.13 (a), the growth of 111 Bragg-peak intensity and the fit of the experimental data to JMA equation is shown as a function of time for the cooling rate of 0.06 K/min.

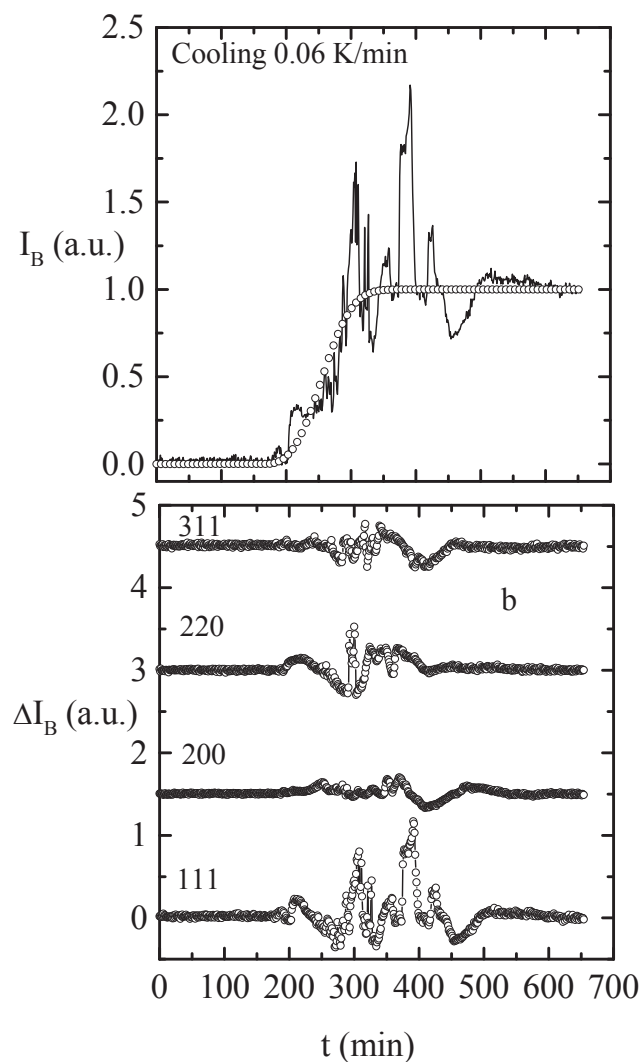


Figure 6.13 Time evolution of (a) the normalized intensity of the 111 Bragg peak for the Al-0.3Ti-0.02B alloy (solid line) at a cooling rate of 0.06 K/min. The open circles indicate a fit to the data with the Johnson-Mehl-Avrami model (see text). (b) the temporal fluctuations in the relative Bragg peaks ($\Delta I_B = I_B - I_{JMA}$) for the Al-0.3Ti-0.02B alloy at a cooling rate of 0.06 K/min.

A reasonable fit to the experimental data was obtained for $n=3$, corresponding to a three-dimensional (3D) grain growth of existing nuclei [4]. Fig. 6.13 (b) shows the temporal fluctuations in the 111, 200, 220, and 311 Bragg peak intensity for cooling rates of 0.06 K/min after subtraction of the fit with the JMA model $\Delta I_B(t) = I_B(t) - I_{JMA}(t)$. During the solidification process the fluctuations in the relative Bragg-peak intensity are significantly larger than the statistical noise in the pure solid and pure liquid phases.

For the time-dependent measurements with a constant sampling time, Δt , the fluctuations in the relative Bragg-peak intensity, $\Delta I_B(t)$, can be analyzed in terms of the normalized time-correlation function [10]:

$$g^{(2)}(\tau) - 1 = \frac{\frac{1}{M} \sum_{i=0}^M [\Delta I_B(t_i) - \langle \Delta I_B \rangle][\Delta I_B(t_i + \tau) - \langle \Delta I_B \rangle]}{\frac{1}{N} \sum_{i=0}^N [\Delta I_B(t_i) - \langle \Delta I_B \rangle]^2} \quad , \quad (6.3)$$

Where τ is the time difference, $\langle \Delta I_B \rangle$ the time-averaged relative Bragg-peak intensity. The values of $N=t_{trans}/\Delta t$ are determined by the ratio between the transformation time t_{trans} and the sampling time Δt . For the continuous cooling experiments $N=656$ and $N=102$ were used for the cooling rates of 0.06 and 0.6 K/min, respectively. For the step wise cooling a constant value of $N=59$ was used for all steps. The sampling time Δt amounts to 1 min for the continuous cooling measurements and 30 s for the step-wise cooling measurements. The value of M vary between 0 and N , according to the relation $M = N - \tau/\Delta t$. The calculated time-correlation function of the relative Bragg peak intensity is shown in Figs. 6.14(a) and 6.15(a) for the cooling rates of 0.06 and 0.6 K/min respectively. The Fourier transform of the time- correlation functions at cooling rates of 0.06 and 0.6 K/min are shown in Fig. 6.14(b) and Fig. 6.15(b). The results of Fourier transforms (FFT) of the time-correlation function clearly indicate that there are pronounced peaks that evidence the existence of non-random oscillations. For a random signal the normalized time-correlation function corresponds to $g^{(2)}(\tau) - 1 = \delta(\tau)$, while for correlated signals it can be described in terms of a series of damped oscillations. In order to model the time-correlation functions we have limited the number of oscillation frequencies to two and assume the following form:

$$g^{(2)}(\tau) - 1 = \exp(-\tau/\tau_c)[A \cos(\omega_1 \tau) + (1-A) \cos(\omega_2 \tau)] \quad , \quad (6.4)$$

Where A is a constant weighing factor, τ_c is the fitted time constant, ω_1 and ω_2 are the oscillation frequencies. The fitted time-correlation function for cooling rates of 0.06 and 0.6 K/min. are shown in Figs. 6.14(a) and 6.15(a). The parameters A , τ_c , ω_1 and ω_2 obtained by fitting the time-correlation function to Eq.(6.4), are listed in Table 1 for all the four Bragg reflection and for cooling rates of 0.06 and 0.6 K/min. The results indicate that the correlation time and oscillation frequencies are of the same order of magnitude for the 111, 200, 220, and 311 Bragg reflections at a given cooling rate but strongly depend on the cooling rate. The damping time increases and the oscillation frequencies decrease for a decreasing the cooling rate.

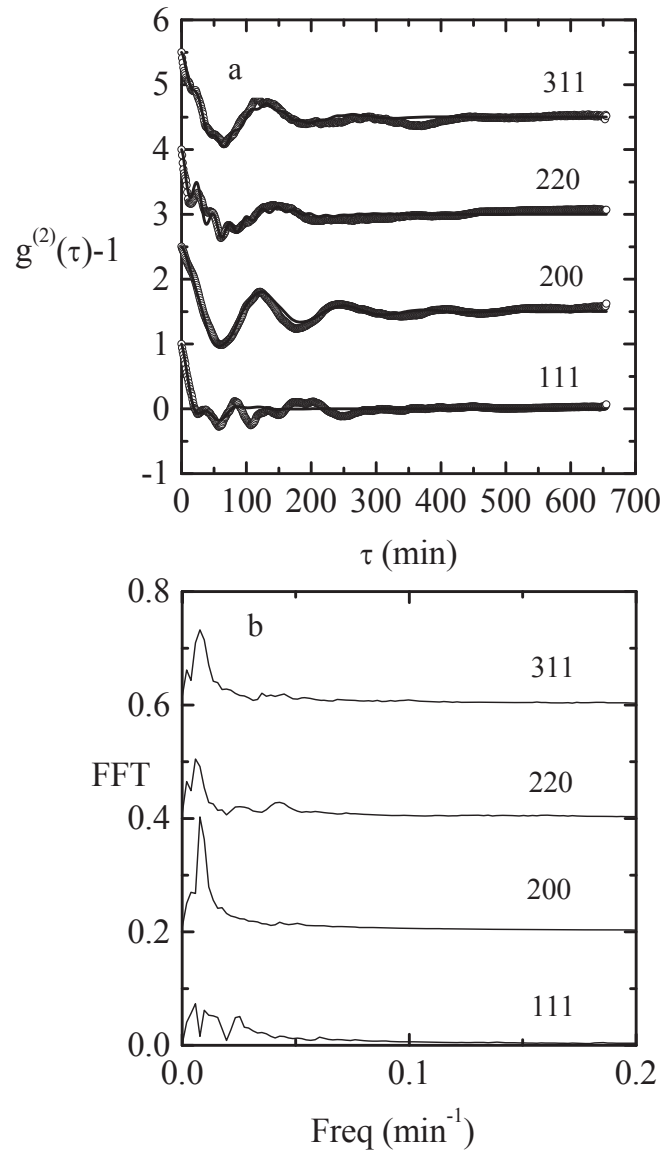


Figure 6.14 Normalized time-correlation function for the 111, 200, 220, and 311 reflections for a cooling rate of 0.06 K/min (a) and its Fourier transform (b). The solid line in (a) is a fit to Eq. (6.4). For clarity each curve is displaced by 1.5 in (a) and 0.2 in (b) compared to immediate lower curve.

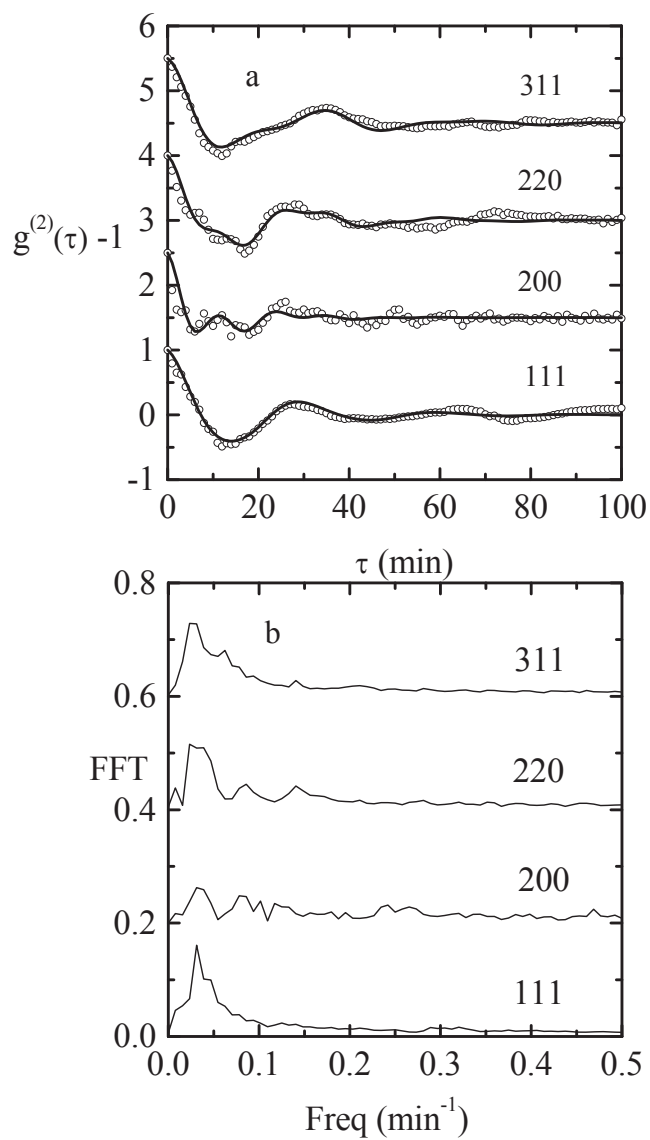


Figure 6.15 Normalized time-correlation function for the 111, 200, 220, and 311 reflections for a cooling rate of 0.6 K/min (a) and its Fourier transform (b). The solid line in (a) is a fit to Eq. (6.4). For clarity curve for each reflection is displaced by 1.5 in (a) and 0.2 in (b) compared to immediate lower curve.

Table 6.3 Time constants τ_c (a), oscillation frequency ω_1 and ω_2 (b) and amplitude A (c) for the temporal fluctuations in the Bragg peak intensity of the 111, 200, 220, and 311 crystal reflections of the Al-0.3Ti-0.02B alloy at two different cooling rates. The parameters were obtained from a fit of the correlation function of the normalized variations in the Bragg-peak intensity to Eq. (6.4).

(a)

Cooling rate (K/min)	τ_c (min)			
	111	200	220	311
0.06	35(2)	105(2)	69(2)	84(2)
0.60	19(1)	12(1)	20(1)	23(1)

(b)

Cooling rate (K/min)	Frequency (min^{-1})	111	200	220	311
		ω_1	0.056(1)	0.050(2)	0.040(4)
	ω_2	0.151(2)	0.198(5)	0.25(1)	0.24(2)
0.60	ω_1	0.208(2)	0.21(1)	0.21(1)	0.189(2)
	ω_2	0.45(4)	0.53(1)	0.52(2)	0.34(1)

(c)

Cooling rate (K/min)	A			
	111	200	220	311
0.06	0.68(1)	0.96(1)	0.70(1)	0.87(1)
0.60	0.94(2)	0.50(4)	0.77(3)	0.70(2)

The time correlation functions were also determined for the step-wise cooling measurements of Fig. 6.9 at each of the constant temperatures. At each temperature the Bragg-peak intensity was monitored for 30 min at a sampling rate of 30 s. Fig. 6.16 shows the change in solid fraction f_s and the corresponding normalized Bragg-peak intensity I_B for the 111 reflection, as a function of temperature. As observed for continuous cooling, pronounced oscillations are observed in time correlation function at constant temperatures during stepwise cooling. These oscillations can be fitted with a damped periodic function with a single frequency in Eq.(6.4) and $A=1$. The fitted temperature dependent correlation time τ_c and oscillation frequency ω are given in Fig. 6.17. The correlation time is found to increase for decreasing temperature with the maximum value of 152 min at a temperature of $T = 906$ K.

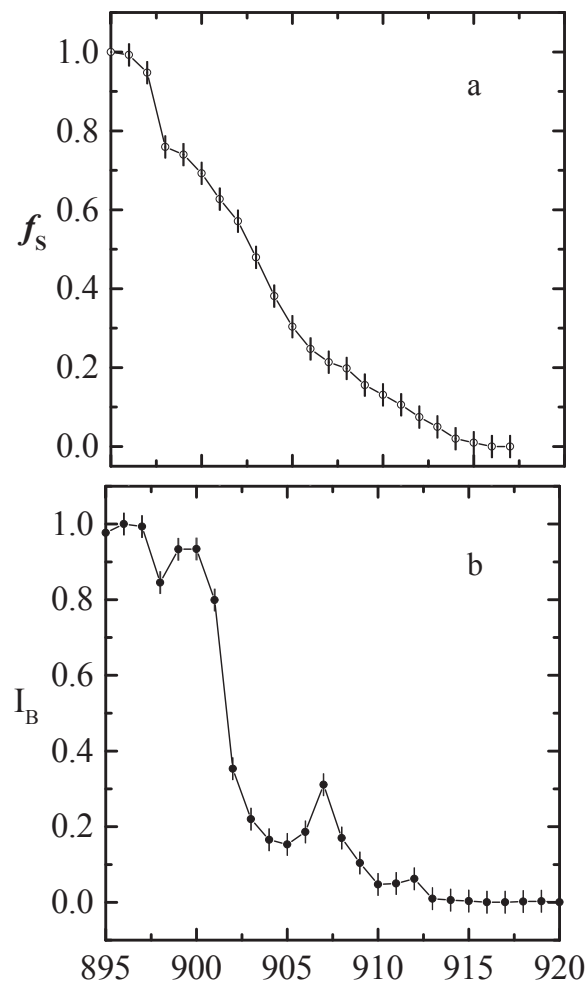


Figure 6.16 The solid fraction f_s (a) and the Bragg-peak intensity of the 111 reflection (b) as a function of temperature during step-wise cooling.

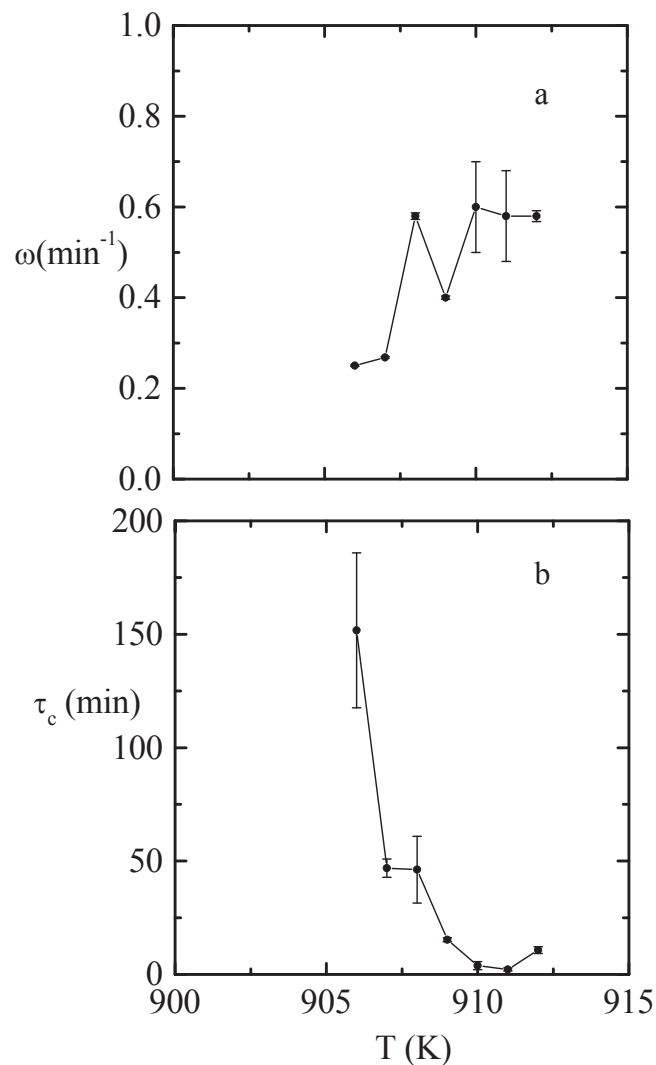


Figure 6.17 The oscillation frequency ω (a) and the time constant τ_c (b), determined from the normalized time-correlation function as a function of temperature for the 111 Bragg-peak, during stepwise cooling.

The physical origin of these quasi-periodic, temporal fluctuations in the Bragg-peak intensity, is a matter of some speculation. There are three different mechanisms that can in principle be responsible for the observed time fluctuations: crystallite motion, Ostwald ripening and growth fluctuations.

The first scenario about the interpretation for the observed temporal oscillations in the Bragg-peak intensity arises from a limited number of grains in the irradiated sample volume. In the absence of a true powder average, the fluctuations in the Bragg peak intensity may be caused by the random motion of solid grains in the liquid. This interpretation seems unlikely due to the quasi-periodic nature of oscillations and the limited mobility of relatively massive grains. For the current beam size of $1 \times 4.1 \text{ cm}^2$, sample diameter of 1 cm, and an estimated grain size of $640 \text{ }\mu\text{m}$ and $460 \text{ }\mu\text{m}$ in solid material for cooling rates of 0.06 and 0.6 K/min, one would expect to see the scattering from the order of 10^5 grains. Estimates from the absolute value of the 111 Bragg-peak intensity suggests an average number of $N \approx 3.0 \times 10^2$ and

1.8×10^3 grains in reflection for cooling rates of 0.06 and 0.6 K/min, respectively. Then assuming finite size effects, the intensity fluctuations will be of the order of $1/\sqrt{N}$, which is too small compared to observed oscillations. Therefore this process does not explain the quasi-periodic nature nor the amplitude of observed intensity fluctuations.

A ripening process is expected to play a significant role for the slow cooling rates applied in our experiment. Each of the final crystallites in the Al-0.3Ti-0.02B alloy contains a large number of TiB₂ nucleating particles. This may indicate that during the growth of the crystallites nucleated by the grain refiners a significant interaction among the crystallites through the Ostwald ripening takes place so as to reduce the system interface energy. During this process a grain can grow at the expense of some of its neighbors, although at the same time it may be consumed by other neighbors, maintaining the local equilibrium. This can result in the quasi-periodic intensity fluctuations of Bragg peaks to which they are reflecting. This continues until the grain size distribution is relaxing to its steady state. As the solidification proceeds and the average crystallites grow in size this process is expected to slow down as observed in the step-wise cooling experiments shown in Fig. 6.17.

The last scenario corresponds to growth fluctuations and can be caused by local fluctuations in temperature (or alternatively in alloy concentration). During the crystallite growth latent heat is released leading to local temperature variations that can subsequently slow down the growth rate. Although this process can be responsible for fluctuations in the increase of the Bragg peak intensity it is less likely that it can lead to temporary decreases as experimentally observed.

We therefore consider the second scenario of Ostwald ripening as the most plausible mechanism responsible for temporal growth variations, which provides a qualitative explanation of the non-random oscillations observed during solidification of the Al-0.3Ti-0.02B alloy.

6.2.5 Conclusions

We have presented experimental data on the crystallization dynamics during the liquid-solid phase transformation in an Al-0.3Ti-0.02B alloy, as a function of cooling rate and temperature. It is found that oscillations in the Bragg-peak intensities are observed during the liquid-solid phase transformation, which have a non-random character. The average correlation time and the oscillation frequency is found to be dependent on the cooling rate. The time constant increases and the oscillation frequency decreases for a decreasing cooling rate. The origin of these oscillations seems likely to be the ripening interaction among the evolving crystals that ultimately controls the grain growth. Stepwise cooling measurements further indicate a slow down in the crystallization dynamics for decreasing temperatures, suggesting that the ripening process saturates as the crystals grow in size below the transition temperature.

Acknowledgements

We thank the Institute Laue-Langevin for the beam time to perform these neutron diffraction experiments. This work was financed in part by the Netherlands Foundation for Fundamental Research of Matter (FOM) and the Netherlands Institute for Metals Research (NIMR).

References

- [1] R. F. Shannon, M. G. Glavicic, M. A. Singh, J. Macromol. Sci. B 33 (1994) 357.
- [2] C. M. Allen, K. A. Q. O'Reilly, B. Cantor, P. V. Evans, Mat. Sci. Eng. A 226-228 (1997) 784.
- [3] M. Easton, D. Stjohn, Met. Mater. Trans. A 30 (1999) 1625.
- [4] N. Iqbal, N. H. van Dijk, V. W. J. Verhoeven, W. Montfrooij, T. Hansen, L. Katgerman, G. J. Kearley, Acta. Mater. 51 (2003) 4497.
- [5] J. Johnson, R. Mehl, Trans. A.I.M.E. 135 (1939) 416.
- [6] M. Avrami, J. Chem. Phys. 7 (1939) 1103.
- [7] M. Avrami, J. Chem. Phys. 8 (1940) 212.
- [8] M. Avrami, J. Chem. Phys. 9 (1941) 177.
- [9] D. W. Henderson, J. Thermal. Anal. 15 (1979) 325.
- [10] H. Z. Cummins and E. R. Pike, *Photon Correlation Spectroscopy and Velocimetry*, Plenum, New York, 1977.

6.3 The role of solute titanium and TiB₂ particles in the liquid-solid phase transformation of aluminum alloys

*N. Iqbal, N. H. van Dijk, T. Hansen, L. Katgerman, and G. J. Kearley;
Materials Science and Eng. A 386 (2004) 20*

Abstract

The nucleation and growth kinetics of α -Al grains in the systems Al-0.1Ti and Al-0.15TiB₂ wt.% (weight percent) have been studied by time-resolved neutron diffraction measurements during the liquid-solid phase transformation for continuous cooling. The time evolution of the static structure factor $S(Q)$ has been monitored for different cooling rates. The evolution of the solid fraction f_s for both samples during the transformation is determined from the normalized variation of the height of first peak in the liquid structure factor. The transformation kinetics is analyzed in terms of the Johnson-Mehl-Avrami model, and compared for both samples. The time evolution of Bragg peaks emerging after the nucleation of the solid phase is monitored. Our results reveal that the TiB₂ particles in pure aluminum are not the effective nucleation sites for α -Al grains during solidification. However, the presence of solute titanium in the Al-0.1Ti alloy is found to change the growth rate of crystallization during solidification. In the early stages of the phase transformation in Al-0.1Ti alloy, pronounced oscillations in the Bragg peaks intensity are observed. These observations are discussed in the light of the present grain refinement theories.

6.3.1 Introduction

The liquid to solid phase transformation has a vital influence on the macroscopic properties of aluminum alloys. A significant improvement of the mechanical properties of aluminum can be obtained by the addition of small amounts of Al-Ti-B master alloys [1,2]. These alloys contain microscopic TiB₂ and TiAl₃ nucleating particles. Experiences indicate that the Al-Ti-B alloys are effective grain refiners but similar alloys containing only TiB₂ or TiAl₃ particles are much less effective. Various theories regarding the grain refining mechanisms of Al-Ti-B refiners are proposed [3-8], such as the particle theory, the phase diagram theory, the duplex nucleation theory and the peritectic hulk theory. Although the idea that TiB₂ particles combined with solute titanium play central role in the transformation process, seems to be gaining wider acceptance [2,8], a complete understanding and general consensus of mechanism(s) involved is still lacking. In order to obtain a better understanding of the grain refining mechanism(s) it is necessary to study the time evolution of the liquid to solid phase transformation kinetics of these aluminum alloys, in-situ, containing TiB₂ nucleant particles and solute Ti, separately and both together.

We have previously reported the transformation kinetics of the liquid to solid phase transformation in pure aluminum and in a Al-0.3Ti-0.02B (wt. %) alloy containing both TiB₂ nucleant particles and solute Ti [9]. In the present paper the transformation kinetics and the effectiveness for grain refinement of both TiB₂ particles and of solute titanium in aluminum is studied separately, by time-dependent neutron diffraction measurements during the solidification of Al-0.15TiB₂ (wt. %) and Al-0.1Ti (wt.%) alloys for different continuous cooling rates. A big advantage of

neutrons is that the bulk sample can be studied *in-situ*, because of large penetration length for neutrons into the sample.

6.3.2 Materials and method

6.3.2.1 Sample preparation

The studied samples were laboratory prepared from high purity aluminum, titanium and TiB₂ particles. The pure aluminum (99.999 %) and titanium (99.99 %) were purchased from Goodfellows. The TiB₂ (99.99 %) powder with a particle size distribution ranging from 3 to 6 μm with a maximum around 4.4 micrometer was purchased from Advanced Ceramics.

The Al-0.15TiB₂ (wt. %) sample was prepared by putting aluminum lumps with a total mass of 35 gram and with the added TiB₂ particles into an aluminum oxide crucible. The sample was heated to the temperature of $T = 1023$ K. After holding at this temperature for 30 minutes, the crucible was removed from the furnace and the liquid alloy was homogenized by stirring using an aluminum oxide rod. After solidification the sample was remelted and the above mentioned process was repeated three times to ensure that the TiB₂ particles were homogeneously distributed in the Al-0.15TiB₂ (wt. %) sample. The solid sample was then cut into cylinders with a diameter of 9 mm.

In order to prepare the Al-0.1Ti (wt. %) sample, a different route was adopted. First, Al-1Ti (wt. %) master alloy samples, of 5 gram each, were prepared by melting together the appropriate amounts of aluminum and titanium in an electric arc furnace in a high purity argon atmosphere. The molten samples were stirred by using the arc flame for homogenization. Then the samples were solidified, rotated by changing the top and bottom positions, and remelted. This process was repeated five times to ensure that titanium is homogeneously distributed in the sample. Having prepared the Al-1Ti (wt. %) master alloy samples, the Al-0.1 Ti (wt. %) sample was prepared by melting it together with an appropriate amount of high purity aluminum, by the method described for the Al-0.15TiB₂ sample.

The differential thermal analysis (DTA) measurements were performed on these samples, with sample dimensions $2 \times 2 \times 2$ mm³, so as to make a true estimate of transition temperatures. The results revealed that for the slow cooling rate of 0.5 K/min, the liquid to solid transformation starts at $T_s = 932.1$ K, and the transformation completes at $T_f = 929.1$ K for the Al-0.15TiB₂ alloy. Whereas for the Al-0.1Ti alloy, the transformation starts at $T_s = 933.6$ K, and the transformation is completes at $T_f = 929.2$ K for the cooling rate of 0.5 K/min.

6.3.2.2 Experimental method

In-situ neutron diffraction measurements were performed at the high-flux powder diffractometer D20 at the Institute Laue-Langevin (ILL). The Al-0.15TiB₂ and Al-0.1Ti alloy samples with a mass of 10 g were placed in a cylindrical single-crystalline sapphire container with a height of 60 mm, an inner diameter of 10 mm, and a wall thickness of 1 mm. A monochromatic neutron beam with wavelength of 0.94 Å and a beam height of 41 mm was used for all neutron diffraction experiments. For the high temperature neutron diffraction measurements a dedicated vacuum furnace (4×10^{-5} mbar) was used with a vanadium heater element and a temperature

stability of about 1 K. In order to achieve the temperature stability required for our solidification experiments ($\Delta T < 50$ mK), a specially designed furnace insert was used [9].

6.3.3 Results and discussion

6.3.3.1 Liquid structure factor

In Fig. 6.18 the measured liquid structure factor, $S(Q)$, as a function of the wave-vector transfer, Q , is shown for the Al-0.15TiB₂ and Al-0.1Ti alloy samples at a temperature of $T = 943$ K. The observed structure factor is in agreement with previous neutron [9-11] and X-ray diffraction [12,13] studies of liquid aluminum in the vicinity of the solidification temperature. The first liquid peak for both samples is observed at $Q = 2.68 \text{ \AA}^{-1}$ with a height of $S(Q) = 2.39$ for liquid Al-0.15TiB₂ alloy and $S(Q) = 2.56$ for liquid Al-0.1Ti, respectively. The previously studied samples of pure aluminum and Al-0.3Ti-0.02B (wt. %) alloy show a height of the first liquid peak at $Q = 2.68 \text{ \AA}^{-1}$ with $S(Q) = 2.44$ and 2.39 , respectively. The measured structure factor of liquid Al-0.15TiB₂ and Al-0.1Ti alloy closely resembles the curve of pure aluminum [9] indicating a weak influence of the alloying elements on the short-range order in the liquid.

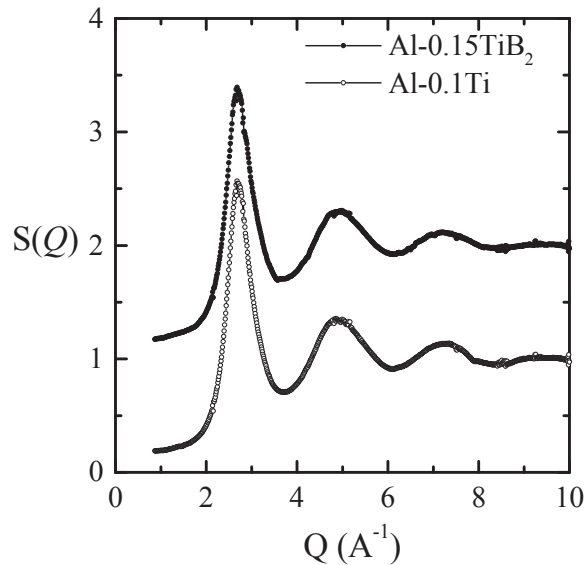


Figure 6.18 Liquid structure factor $S(Q)$ as a function of the wave-vector transfer Q for the Al-0.15TiB₂ (solid circles) and the Al-0.1Ti alloy (open circles) at a temperature of $T = 943$ K. For clarity $S(Q)$ of the Al-0.1Ti alloy is vertically displaced by 1.

6.3.3.2 Liquid volume fraction

In order to study the influence of TiB₂ particles and solute titanium on the crystallization behaviour of aluminum, systematic time dependent neutron diffraction measurements of the structure factor in Al-0.15TiB₂ and Al-0.1Ti alloys were

performed during solidification. For each of the measurements the sample was heated to a temperature of 943 K for one hour to obtain a homogeneous liquid phase, followed by a continuous cooling with rates of 0.06 and 0.6 K/min for the Al-0.15TiB₂ alloy and 0.06, 0.2 and 0.6 K/min for the Al-0.1Ti alloy. During cooling the structure factor was monitored by neutron diffraction in time steps of 1 min. During the liquid to solid phase transformation the liquid peaks in the structure factor (Fig. 6.18) gradually decrease while the Bragg peaks from the solid phase emerge and grow. As the observed Bragg peak intensity strongly depends on texture in the solid phase, we use the scattering from the liquid phase to determine the liquid and solid volume fractions.

Figs. 6.19 and 6.20 show the behaviour of the liquid volume fraction for the Al-0.15TiB₂ and Al-0.1Ti alloys as a function of temperature for different cooling rates, as determined from the normalized variation in the first maximum of the liquid peak in the structure factor, $S(Q)$, at $Q = 2.68 \text{ \AA}^{-1}$. In Table 6.4 a summary of the experimental transformation temperatures as a function of cooling rate is given for both samples. The values mentioned in table 1 should not be taken as true transition temperatures. As mentioned in the schematic experimental setup [9], the platinum resistance thermometer is placed inside the cylindrical vanadium heating foil. At high temperatures the magnetic field induced by the constant high current through the vanadium foil may cause a weak inductive coupling to the current through platinum resistance thermometer and possibly cause a constant temperature shift in the readout. The real onset temperatures of the transformation should therefore show no significant undercooling as we confirmed in Differential Thermal Analysis (DTA) experiments on smaller samples for low cooling rates. However, once the transformation starts the temperature width of the transformation, shown in Fig. 6.19 and 6.20, closely represent that for the sample under study. These results indicate that for the same cooling rate the transformation extends over a wider temperature range in the Al-0.1Ti alloy compared to that of the Al-0.15TiB₂ alloy. As a consequence, the temperature where half of the liquid volume of the Al-0.15TiB₂ and Al-0.1Ti alloys is transformed to solid ($T_{1/2}$) decreases by 12 K and 19 K, respectively, for a tenfold increase in cooling rate. Compared to the pure aluminum sample [9], the liquid/solid phase transformation of both the Al-0.15TiB₂ and the Al-0.1Ti alloy occurs over a wider temperature range regardless of the cooling rate.

Table 6.4 Transformation temperatures of the Al-0.15TiB₂ and the Al-0.1Ti alloys at different cooling rates, where T_s is the transformation start temperature, T_f the transformation finish temperature, and $T_{1/2}$ the temperature halfway the transformation. In addition, the temperature width of the transformation $\Delta T = T_s - T_f$ and the average undercooling $T_o - T_{1/2}$ with respect to the crystallization temperature of $T_o = 933 \text{ K}$ are listed.

Sample	Cooling rate (K/min)	T_s (K)	T_f (K)	$T_{1/2}$ (K)	ΔT (K)	$T_o - T_{1/2}$ (K)
Al-0.15TiB ₂	0.06	923	915	918	8	15
	0.60	919	895	906	24	27
Al-0.1Ti	0.06	923	910	912	13	21
	0.20	920	898	902	22	31
	0.60	915	884	893	31	40

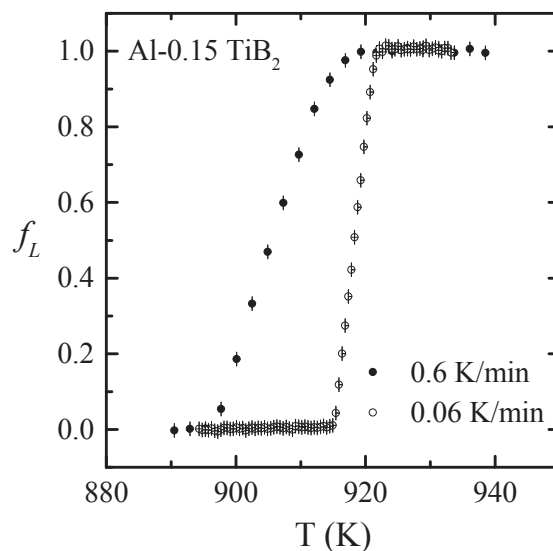


Figure 6.19 Liquid volume fraction f_L of the Al-0.15TiB₂ alloy as a function of temperature for cooling rates of 0.06 K/min (open circles) and 0.6 K/min (solid circles). The liquid volume fraction f_L is deduced from the normalized variation in the first liquid peak in $S(Q)$ at $Q = 2.68 \text{ \AA}^{-1}$.

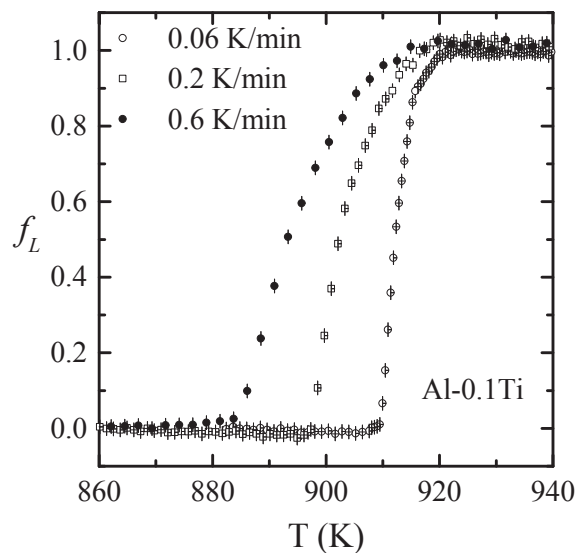


Figure 6.20 Liquid volume fraction f_L of the Al-0.1Ti alloy as a function of temperature for cooling rates of 0.06 K/min (open circles), 0.2 K/min (open squares) and 0.6 K/min (solid circles). The liquid volume fraction f_L is deduced from the normalized variation in the first liquid peak in $S(Q)$ at $Q = 2.68 \text{ \AA}^{-1}$.

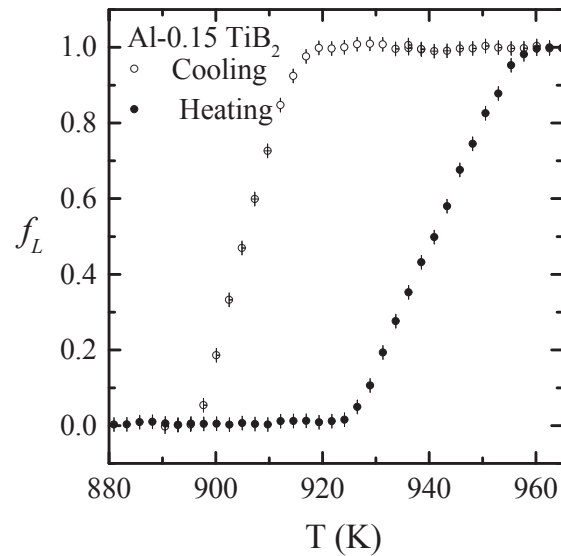


Figure 6.21 Liquid volume fraction f_L of the Al-0.15TiB₂ alloy as a function of temperature for cooling (open circles) and heating (solid circles) at a cooling rate of 0.6 K/min. The liquid volume fraction f_L is deduced from the normalized variation in the first liquid peak in $S(Q)$ at $Q = 2.68 \text{ \AA}^{-1}$.

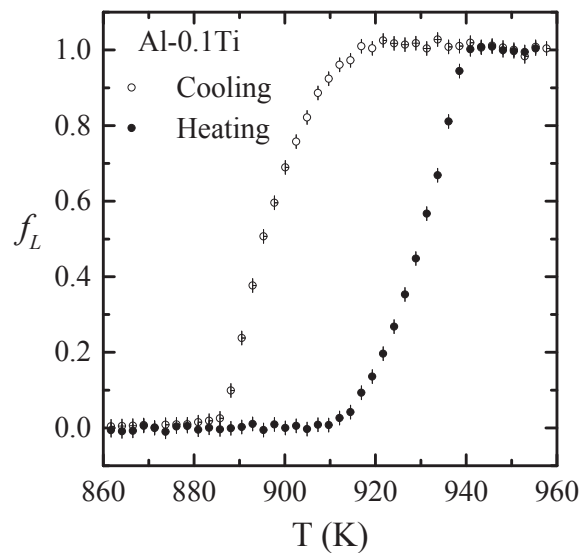


Figure 6.22 Liquid volume fraction f_L of the Al-0.1Ti alloy as a function of temperature for cooling (open circles) and heating (solid circles) at a cooling rate of 0.6 K/min. The liquid volume fraction f_L is deduced from the normalized variation in the first liquid peak in $S(Q)$ at $Q = 2.68 \text{ \AA}^{-1}$.

As expected for a phase transformation that involves latent heat, the melting/freezing transition exhibits thermal hysteresis [14]. In Figs. 6.21 and 6.22 this thermal hysteresis is demonstrated in the combined heating and cooling experiments on the liquid volume fraction of the Al-0.15TiB₂ and Al-0.1Ti alloy for a heating/cooling rate of 0.6 K/min. The thermal hysteresis of the transformation temperature halfway the transformation of both samples is $\Delta T_{1/2} = 33.6$ K. The corresponding hysteresis in time amounts to $\Delta t_{1/2} = 56$ min. The observed thermal hysteresis is far too large to be caused by a weak thermal link between the sample and the thermometer, as for our furnace insert [9] the estimated response time for thermal equilibrium is about 2 min, giving rise to thermal hysteresis of about 4 min during heating/cooling cycle, which is significantly lower than the observed thermal hysteresis in samples investigated.

6.3.3.3 Transformation kinetics

The crystallization kinetics during isothermal phase transformations has been widely studied using the Johnson-Mehl-Avrami (JMA) model [15-18], with examples in glasses [19,20], gels [21,22], polymers [23], steels [24], and metal alloys [25,26]. According to this model the crystallization fraction, f , can be described as a function of time, t , by the following equation:

$$f(t) = 1 - \exp\{-k(t - t_0)^n\}, \quad (6.5)$$

where k is the rate constant, t_0 is the incubation time, and n the Avrami exponent. The value of the exponent, n , is expected to vary between 1 and 4 depending on the nucleation mechanism and the growth dimensionality [27]. For our continuous cooling experiments the time-dependent undercooling and the release of latent heat during the transformation can lead to a complicated variation in local temperature as a function of time. As a consequence the growth rate may show a significant time dependence. Given these limitations we feel that the application of the JMA model can give qualitative information on (1) the nucleation process and (2) the relative growth rates. For continuous cooling the transformation time, t , in the JMA equation can be set to zero at the time the temperature falls below the crystallization temperature, $T_0 = 933$ K [9, 23]. Under the assumption that the transformation kinetics depends on the transformation time and is independent of temperature, we can fit the experimental data to the JMA model of Eq. (6.5). Provided that there is no change in the nucleation and growth mechanism during the phase transformation, the Avrami exponent, n , is expected to be constant [28] and was found to be $n \approx 3$ for the liquid to solid phase transformation in pure aluminum and in the Al-0.3Ti-0.02B alloy for cooling rates of 0.6 and 0.06 K/min [9].

In Figs. 6.23 and 6.24, the solid volume fraction, $f_S(t) = 1 - f_L(t)$, deduced from the liquid fraction is shown as a function of time for the Al-0.15TiB₂ and Al-0.1Ti alloys for cooling rates of 0.06 and 0.6 K/min. The results of a fit of the JMA equation for fixed values of n and t_0 to the experimental data are listed in Table 6.5 and effectively probes the grain density times the average growth rate. The corresponding fitted curves are shown in Figs. 6.23 and 6.24. The results indicate that the rate constant, k , for the Al-0.1Ti alloy is an order of magnitude lower than that of the Al-0.15TiB₂ alloy. The fully solidified Al-0.15TiB₂ and Al-0.1Ti samples were also investigated under optical microscope. A relatively large grain size was observed for both samples indicating the absence of a significant grain refinement. The variation in rate constant k for these samples reflects a difference in average growth rate caused by

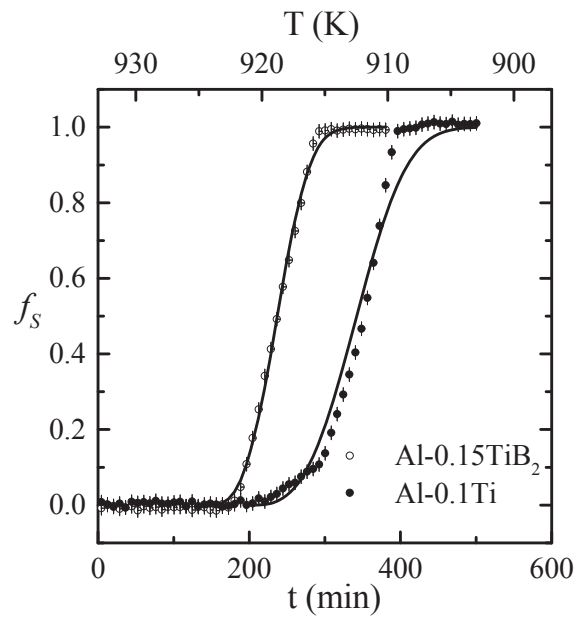


Figure 6.23 Time evolution of the solid volume fraction $f_s = 1 - f_L$ for the Al-0.15TiB₂ (open circles) and the Al-0.1Ti alloy (solid circles) at a cooling rate of 0.06 K/min. The solid line indicates a fit to the data with the Johnson-Mehl-Avrami model (see text).

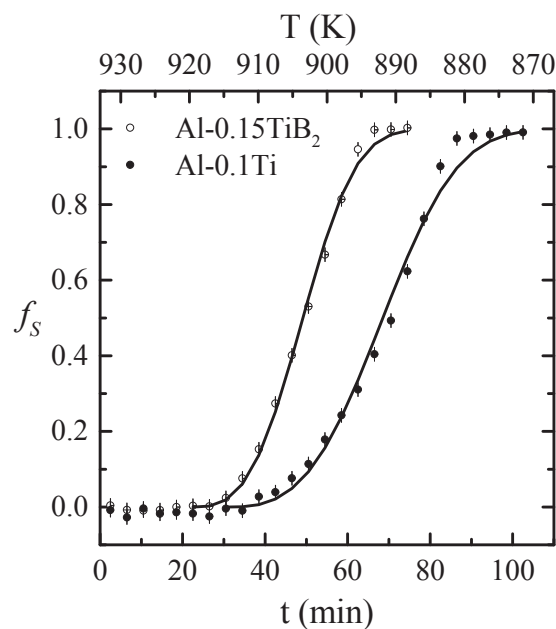


Figure 6.24 Time evolution of the solid volume fraction $f_s = 1 - f_L$ for the Al-0.15TiB₂ (open circles) and the Al-0.1Ti alloy (solid circles) at a cooling rate of 0.6 K/min. The solid line indicates a fit to the data with the Johnson-Mehl-Avrami model (see text).

Table 6.5 Transformation parameters of the Al-0.15TiB₂ and the Al-0.1Ti alloys at different cooling rates obtained from a fit of the experimental liquid volume fraction to the JMA model, where n is the Avrami exponent, k is the rate constant, t_0 is the transformation start time, and $t_{1/2} - t_0 = [\ln(2)/k]^{1/n}$ is the time halfway the transformation after the start of the transformation. The time when the temperature falls below the crystallization temperature $T_0 = 933$ K is chosen as $t = 0$.

Sample	Cooling rate (K/min)	n	k (min ^{-n)}	t_0 (min)	$t_{1/2} - t_0$ (min)
Al-0.15TiB ₂	0.06	3.1	$9.4(3) \times 10^{-7}$	160	75.3
	0.60	3.1	$2.0(7) \times 10^{-5}$	22	28.3
Al-0.1Ti	0.06	3.1	$1.4(7) \times 10^{-7}$	200	138
	0.20	3.1	$8.1(4) \times 10^{-7}$	70	79
	0.60	3.1	$8.4(3) \times 10^{-6}$	30	37.3

the solute titanium in Al-0.1Ti alloy rather than a difference in nucleated grain density in these samples. By increasing the cooling rate, the rate constant, k , increases for both samples. The variation in rate constant for different cooling rates suggests that the average growth rate is enhanced for higher cooling rates due the larger value of the maximum undercooling during the slow transformations under (quasi) equilibrium conditions. The values of rate constant for the Al-0.15TiB₂ alloy at cooling rates of 0.06 K/min and 0.6 K/min are found to be close to those observed for pure aluminum [9] indicating that the TiB₂ particles in pure aluminum does not significantly change its transformation kinetics during solidification. Our observations are in agreement with the results reported by Mohanty *et al.* [29, 30] for the grain refinement process of aluminum in the presence of TiB₂ particles of diameter about 5 μ m and at various solute titanium concentrations. In the absence of solute titanium, no grain refinement was observed. Thus the results obtained from the present neutron diffraction measurements support the theory that TiB₂ particles in pure aluminum are not the effective nucleation sites for the α -Al grains during solidification. The observed value of $t_{1/2}$ for the Al-0.15TiB₂ alloy is lower than that of the Al-0.1Ti alloy for both cooling rates, confirming the relatively slow crystallization during the solidification of the Al-0.1Ti alloy.

6.3.3.4 Intensity fluctuations

Fig. 6.25, shows the time evolution of the solid fraction and the corresponding Bragg peak intensity from the (220) reflection of the α -Al (fcc) grains in the Al-0.15TiB₂ alloy during solidification with a cooling rate of 0.6 K/min. The observed liquid to solid phase transformation is continuous and no anomalous behavior is observed. However, during the early stages of liquid to solid phase transformation of Al-0.1Ti alloy, the variations in the Bragg peak intensity from the nucleating crystallites were observed. These variations in the Bragg peak intensity are found to be present in all the observed Bragg reflections and for different cooling rates. Fig. 6.26 shows the time evolution of the (311) Bragg reflection in the Al-0.1Ti alloy for cooling rates of 0.06, 0.2 and 0.6 K/min respectively. The observed behavior is quite similar to that of previously reported results for the solidification of the Al-0.3Ti-0.02B alloy [9, 31]. However, for the solidification of the Al-0.3Ti-0.02B alloy, these

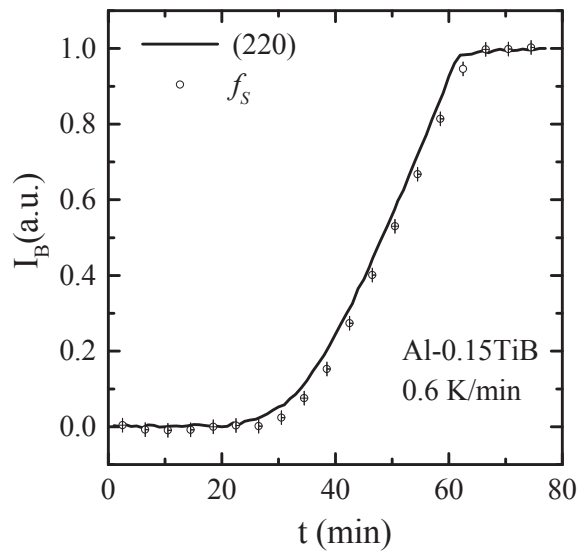


Figure 6.25 Normalized integrated Bragg peak intensity I_B for the (220) reflection of the Al-0.1TiB₂ as a function of the time t for a cooling rate of 0.6 K/min. For comparison the time evolution of the solid volume fraction $f_S = 1 - f_L$ deduced from the variation in the first liquid peak in $S(Q)$ is shown.

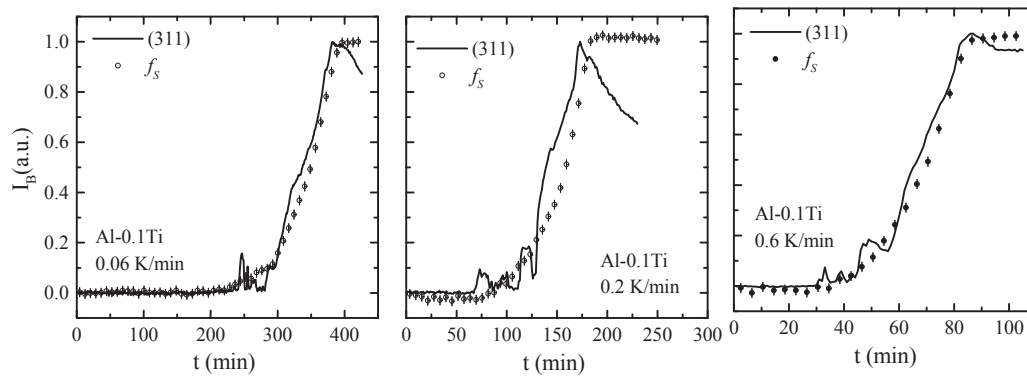


Figure 6.26 Normalized integrated Bragg peak intensity I_B for the (311) reflection of the Al-0.1Ti alloy as a function of the time t for a cooling rate of 0.06, 0.2 and 0.6 K/min. For comparison the time evolution of the solid volume fraction $f_S = 1 - f_L$, deduced from the variation in the first liquid peak in $S(Q)$, is shown.

time-dependent Bragg-peak intensity fluctuations were present during the whole liquid to solid phase transformation process. For the Al-0.1Ti alloy the intensity fluctuations were only observed during the early stage of the solidification process (for $f_s < 0.20$) at all cooling rates. When the solidification is complete, a change in Bragg peak intensity is observed, which is probably due to coarsening of the solid grains at high temperature.

The observed fluctuations in Bragg peak intensity, only at the start of the solidification process in the Al-0.1Ti alloy, limits our ability to analyze the possible dynamics of phase transformation during solidification. These fluctuations in Bragg peak intensity are probable due to the motion of few individual crystallites that are formed at the start of the solidification process. Easton and StJohn [2] have proposed that at the beginning of solidification, the driving force for nucleation is usually thermal undercooling in the melt at the sample container wall and then the titanium partitioning between the solid-liquid interface leads to constitutional undercooling immediately ahead of the growing solid, with in which the nucleant particles become activated for nucleation. In such a case the grains produced during the early crystallization process in Al-0.1Ti alloy, will be bound with the container surface and their motion is not probable. Therefore it appears that in the beginning of the solidification of the Al-0.1Ti alloy, the nucleation starts in the liquid aluminum, away from the container wall. This is possible only if there exist some effective nucleation sites inside the melt. As no impurity particles are expected in the Al-0.1Ti alloy because of the high purity of the starting materials used, then it is probable, as predicted by the duplex nucleation theory [29], that the formation of a TiAl_3 phase takes place even at concentrations of titanium below the peritectic composition < 0.15 wt.% Ti. In such a case as TiAl_3 is an effective nucleation site for α -Al grains, it can activate the crystallization process in the aluminum melt, away from the container wall and the motion of these crystallites can give rise to the observed intensity fluctuations. This observation supports the hypothesis that when both TiB_2 particles and the solute titanium is present in liquid aluminum, even at the hypoperitectic composition, a layer of TiAl_3 coats TiB_2 particles, thus making it effective nucleation site, during the grain refinement process in aluminum and is needed for epitaxial growth of nucleating grains of aluminum. However, further investigations are necessary to validate this theory.

6.3.4 Conclusions

This paper presents the structural and kinetic features of the crystallization kinetics in Al-0.15 TiB_2 and Al-0.1Ti alloys as a function of cooling rate during continuous cooling. The results obtained from these measurements support the theory that TiB_2 particles in pure aluminum are not the effective nucleation sites for the α -Al grains in liquid aluminum during solidification. The presence of solute titanium in aluminum causes a significant change in the growth kinetics of aluminum during solidification. The crystallization behavior of Al-0.1Ti alloy, during solidification, indicates the possible formation of TiAl_3 phase responsible for the nucleation of aluminum grains.

Acknowledgements

We gratefully acknowledge the technical assistance by Y.K. Huang from the University of Amsterdam, for the preparation of Al-1Ti master alloys. Thanks are due to the Institute Laue-Langevin for the beam time provided to perform these neutron

diffraction experiments. This work was financed in part by the Netherlands Foundation for Fundamental Research of Matter (FOM) and the Netherlands Institute for Metals Research (NIMR).

References

- [1] M. Easton, D. StJohn, *Met. Mater. Trans.* A30 (1999) 1613.
- [2] M. Easton, D. StJohn, *Met. Mater. Trans.* A30 (1999) 1625..
- [3] A. Cibula, *J. of the Institute of Metals* 80 (1951) 1.
- [4] A. Marcantonio, L. F. Mondolfo, *Metal. Trans.* 2 (1971) 465.
- [5] I. Maxwell, and A. Hellawell, *Acta Metal.* 23 (1974) 229.
- [6] L. Backerud, *Light Metal Age.* 41 (1983) 6.
- [7] G. K. Sigworth, *Metal. Trans.* A15 (1984) 277.
- [8] A. L. Greer, A. M. Bunn, A. Tronche, P. V. Evans, and D. J. Bristow, *Acta. Mater.* 48 (2000) 2823.
- [9] N. Iqbal, N. H. van Dijk, V. W. J. Verhoeven, W. Montfroofij, T. Hansen, L. Katgerman, and G. J. Kearley, *Acta. Mater.* 51 (2003) 4497.
- [10] S. Takeda, Y. Kawakita, M. Inu, K. Maruyama, S. Tamaki, and Y. Waseda, *J. Non-Crys. Sol.* 205-207 (1996) 365.
- [11] S. Takeda, S. Harada, S. Tamaki, and Y. Waseda, *J. Phys. Soc. Jpn.* 60 (1991) 2241.
- [12] Y. Waseda, *The structure of Non-Crystalline Materials*, (McGraw-Hill, New York, 1980).
- [13] IAMP database of SCM-LIQ, Tohoku University.
URL: <http://www.iamp.tohoku.ac.jp/database/scm/LIQ/sq.html>
- [14] A. B. Herhold, H. E. King, and E. B. Sirota, *J. Chem. Phys.* 116 (2002) 9036.
- [15] J. Johnson, R. Mehl, *Trans. A.I.M.E.* 135 (1939) 416.
- [16] M. Avrami, *J. Chem. Phys.* 7 (1939) 1103.
- [17] M. Avrami, *J. Chem. Phys.* 8 (1940) 212.
- [18] M. Avrami, *M. J. Chem. Phys.* 9 (1941) 177.
- [19] Y. M. Sung, S. Kim, *J. Mater. Sci.* 35 (2000) 4293.
- [120] A. F. Gualtieri, E. Mazzucato, C. C. Tang, and R. Cernik, *J. Mater. Sci. Forum*, 312 (2000) 224.
- [21] A. M. Fogg, S. J. Price, J. J. Francis, S. O' Brien, and D. O'Hare, *J. Mater. Chem.* 10 (2000) 2355.
- [22] J. Malek, *Thermochem. Acta* 355 (2000) 239.
- [23] P. Supaphol, *J. Appl. Pol. Sci.* 78 (2000) 338.
- [24] D. V. Louzguine, A. Inoue, *J. Mater. Sci.* 35 (2000) 4159.
- [25] J. K. Lee, G. Choi, D. H. Kim, and W. T. Kim, *Appl. Phys. Lett.* 77 (2000) 978.
- [26] C. A. C. Imbert, and H. MacQueen, *J. Mater. Sci. Technol.* 16 (2000) 532.
- [27] D. W. Henderson, *J. Thermal. Anal.* 15 (1979) 325.
- [28] D. A. Porter, K. E. Easterling, *Phase Transformations in Metals and Alloys* (Chapman & Hall, London, 1993)
- [29] P. S. Mohanty, J. E. Gruzleski, *Acta. Metall. Mater.* 43 (1995) 2001.
- [30] P. S. Mohanty, F. H. Samuel, and J. E. Gruzleski, *Metall. Mater. Trans.* 26B (1995) 103.
- [31] N. Iqbal, N. H. van Dijk, V. W. J. Verhoeven, T. Hansen, L. Katgerman, and G. J. Kearley, *Mater. Science and Eng. A* 367 (2004) 82.

6.4 SANS investigations on the solidification of aluminum alloys

*N. Iqbal, N. H. van Dijk, C. D. Dewhurst, L. Katgerman, and G. J. Kearley;
Physica B 350 (2004) 1011*

Abstract

Small-angle neutron scattering (SANS) measurements have been carried out on pure Al and on Al-0.3Ti-0.02B (wt.%) alloy during solidification with different cooling rates. The experimental data have been fitted to the Porod law $(d\Sigma/d\Omega)(Q) = K_p Q^{-4}$, where the increase in Porod constant K_p during solidification is expected to be proportional to the specific surface S_V of the grain boundaries. For increasing cooling rates the specific surface of the grain boundaries is found to increase for both samples, indicating a decrease in grain size. The presence of TiB₂ grain refiners in the Al-0.3Ti-0.02B alloy further reduces the grain size compared to pure aluminum at a given cooling rate.

6.4.1 Introduction

The process of crystal nucleation and growth in liquid aluminum alloys during solidification plays an important role in the mechanical properties of the solid phase. These mechanical properties can be significantly improved by a decrease in the average grain size. This grain refinement is generally achieved by the addition of micron-size TiB₂ particles to the melt, which act as a substrate for heterogeneous nucleation of solid aluminum grains upon solidification. The average grain size can be reduced further by excess titanium in the melt, leading to a reduced grain-growth velocity [1-4]. In this paper, we present small-angle neutron scattering (SANS) experiments for both the pure aluminum and aluminum containing grain refiners with composition Al-0.3Ti-0.02B (wt.%) to estimate the grain size during solidification for different cooling rates. The advantage of SANS is that a relatively large sample volume can be studied *in situ*.

6.4.2 Experimental

The samples used in this study were 99.999 % pure aluminum (Goodfellow) and an Al-0.3Ti-0.02B (wt.%) alloy prepared from an Al-5Ti-0.2B (wt.%) commercial master alloy (KBM AFFILIPS). The particle size distribution of TiB₂ precipitates in the Al-0.3Ti-0.02B alloy was determined by optical microscopy and showed a particle size distribution in the range from 0.6 to 2.2 μm with a maximum around 1.2 μm and the number density $3 \times 10^8 \text{ \#/cm}^3$. The samples were placed in a cylindrical single-crystalline sapphire container with a height of 22 mm, an inner diameter of 10 mm, and a wall thickness of 1 mm. The *in-situ* SANS measurements with fixed neutron wavelength of $\lambda = 10.0 \text{ \AA}$ ($\Delta\lambda/\lambda = 10 \%$) were performed on D11 at the Institute Laue-Langevin.

In order to achieve a higher temperature stability ($\Delta T < 100 \text{ mK}$) for our solidification experiments, a furnace insert consisting of a nickel cylinder with a mass of 252 gm was placed around the sample in a standard radiation furnace under vacuum.

6.4.3 Results and discussion

The influence of grain refiners on the solidification behavior of aluminum was studied by systematic time-dependent SANS measurements on pure aluminum and an Al-0.3Ti-0.02B alloy. For each of the measurements the sample was heated to a temperature of 943 K for one hour to obtain a homogeneous liquid phase, followed by a continuous cooling with rates ranging from 0.3 to 14 K/min. During the continuous cooling the scattered intensity was continuously monitored in time steps of 30 sec. During the liquid to solid phase transformation the scattered intensity gradually increased, but depended on the cooling rate and sample composition.

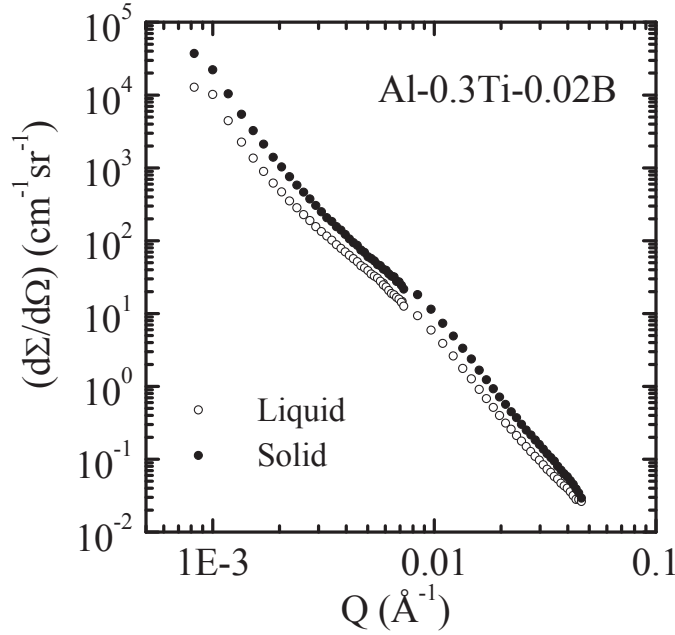


Figure 6.27. Macroscopic differential scattering cross section $(d\Sigma/d\Omega)(Q)$ as a function of wave vector transfer Q of the liquid (open circles) and solid (solid circles) Al-0.3Ti-0.02B alloy for a cooling rate of 0.3 K/min.

In Fig. 6.27 the macroscopic differential scattering cross-section $(d\Sigma/d\Omega)(Q)$ of the liquid Al-0.3Ti-0.02B sample as a function of wave-vector transfer, Q , is compared to that of the sample solidified at a cooling rate of 0.3 K/min. The scattering intensity in Fig. 6.27 has been corrected for the scattering of the empty sapphire container. The wave-vector transfer $Q = (4\pi/\lambda) \sin(\theta)$ is directly related to the scattering angle 2θ . The relatively strong scattering observed in the liquid state is expected to originate predominantly from the TiB_2 particles in the melt. A weak increase in intensity is observed in the solid state compared to the liquid state. The observed change in intensity due to grain boundaries, evolved during solidification can be described by an additional contribution to the measured intensity $\Delta(d\Sigma/d\Omega)(Q)$ such that

$$\Delta\left(\frac{d\Sigma}{d\Omega}\right)(Q) = \left(\frac{d\Sigma}{d\Omega}\right)_{\text{Solid}}(Q) - \frac{(\rho_{\text{Solid}} - \rho_{\text{TiB}_2})^2}{(\rho_{\text{Liquid}} - \rho_{\text{TiB}_2})^2} \left(\frac{d\Sigma}{d\Omega}\right)_{\text{liquid}}(Q) \quad (6.6)$$

Where $(\rho_{\text{Solid}} - \rho_{\text{TiB}_2})^2 / (\rho_{\text{Liquid}} - \rho_{\text{TiB}_2})^2$ accounts for the relative change in scattered intensity caused by the variation in contrast between scattering length density of the

aluminum matrix and the TiB_2 particles as the aluminum density changes during solidification in the Al-0.3Ti-0.02B alloy. When the structural inhomogeneities in the material are relatively large ($QR \gg 1$), the scattering cross-section of the sample can be described by Porod law [5]

$$\Delta\left(\frac{d\Sigma}{d\Omega}\right)(Q) = K_p Q^{-4} + B \quad (6.7)$$

where K_p is the Porod constant and B is the (incoherent) background. In the following we have assumed that B is negligible in the Q range of interest.

The difference in scattering cross-section $\Delta(d\Sigma/d\Omega)(Q)$ between the solid and the liquid state for pure aluminum and that of Al-0.3Ti-0.02B, is studied as a function of Q and for different cooling rates. For increasing cooling rate, a significant increase in scattered intensity is observed which can be analyzed in terms of a fit to the Porod law. This difference in scattering cross-section as a function of cooling rate and the corresponding Porod fit for Al-0.3Ti-0.02B is shown in fig. 6.28.

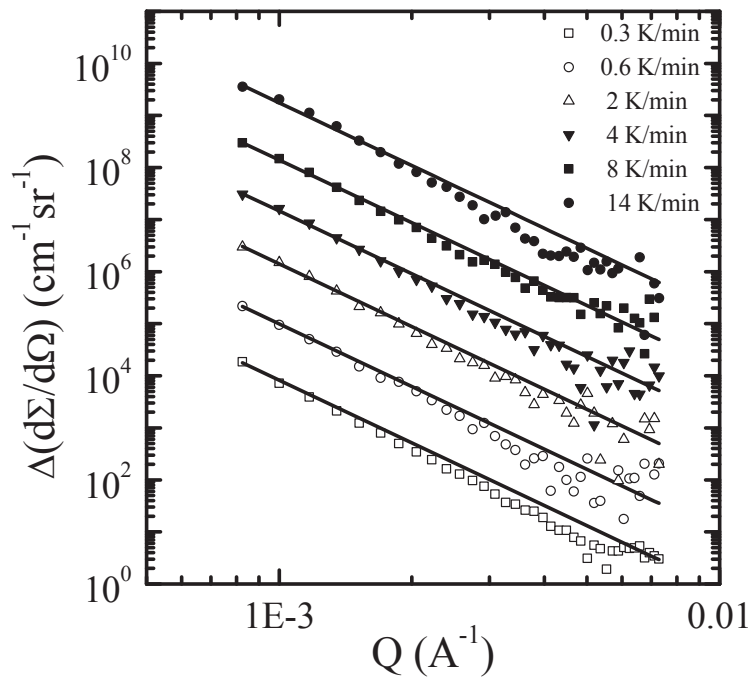


Figure 6.28 Difference of macroscopic differential scattering cross section $\Delta(d\Sigma/d\Omega)(Q)$ between the liquid and the solid phase of Al-0.3Ti-0.02B alloy for different cooling rates.

The calculated Porod constants both for pure aluminum and Al-0.3Ti-0.02B are shown in Fig. 6.29 (a), as a function of cooling rate. The derived Porod constant was found to increase for increasing cooling rates. The Porod constant is defined as $K_p = 2\pi(\Delta\rho)^2 S_v$, where S_v is the specific surface area of grain boundaries and $\Delta\rho$ is the contrast in scattering length density between the grain boundary and the solid aluminum grain. For the difference in scattering between the solid phase and the liquid phase, K_p is expected to be proportional to the specific surface of the grain

boundaries and describes the decrease in grain size with increasing cooling rate. The solid lines are a fit to the Porod law. For clarity the curves for higher cooling rates are multiplied by 10, compared to immediate lower cooling rate. Assuming the solid aluminum grains to be spherical with radius R , $S_v=3/R$. Due to uncertainty in $\Delta\rho$ the microscopic grain structure for the last measured solid aluminum and Al-0.3Ti-0.02B sample, was also investigated by optical microscopy. The average grain size of pure aluminum for a cooling rate of 14 K/min is about 2 mm and that of Al-0.3Ti-0.02B, measured for a cooling rate of 0.3 K/min is about 460 μm . By combining the SANS data on the variation in Porod constant as a function of cooling rate with the metallographic measurements, the average grain size of solid aluminum and Al-0.3Ti-0.02B alloy as a function of cooling rate is determined, as shown in Fig. 6.29 (b). The fits to the experimental data yield information about the change in average grain size in the solid aluminum, with and without grain refiners and as a function of cooling rate. The time resolved small angle neutron scattering measurements were also carried out during the liquid to solid phase transformation. The results of these measurements will be presented in future.

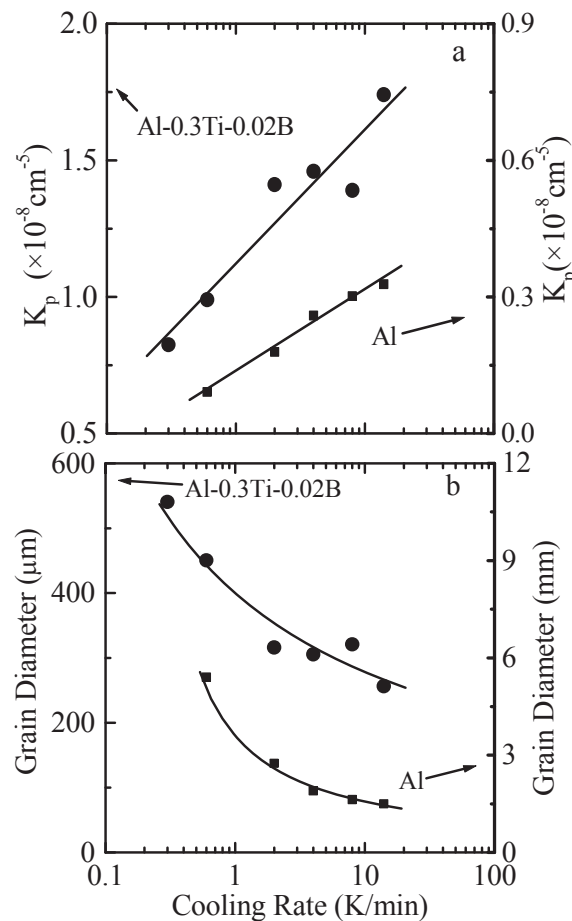


Figure 6.29 (a) Calculated Porod constant K_p for Al-0.3Ti-0.02B alloy (circle) and pure aluminum (square) and (b) the corresponding grain diameter as a function of cooling rate. The size of the symbol is equal to the size of error bar.

Acknowledgement:

We thank the Institute Laue-Langevin for the beam time. This work has been funded by NIMR and FOM (The Netherlands).

References

- [1] M. Easton and D. Stjohn, *Met. Mater. Trans. A* 30 (1999) 1613.
- [2] M. Easton and D. Stjohn, *Met. Mater. Trans. A* 30 (1999) 1625.
- [3] N. Iqbal, N. H. van Dijk, V. W. J. Verhoeven, T. Hansen, L. Katgerman and G. J. Kearley, *Proc. 6th Int. ESAFORM Conf. On Material Forming*, European Scientific Association for Material Forming (2003), p. 411.
- [4] N. Iqbal, N. H. van Dijk, V. W. J. Verhoeven, T. Hansen, W. Montfroiij , L. Katgerman , and G. J. Kearley, *Acta. Mater.* 51 (2003) 4497.
- [5] G. Porod, *Z. Kolloid.* 124 (1951) 83.

Chapter 7

Three dimensional X-ray diffraction for grain nucleation and growth

7.1 Microscopic view on grain nucleation and growth kinetics during solidification of aluminum alloys.

N. Iqbal, N. H. van Dijk, S. E. Offerman, M. Moret, L. Katgerman, and G. J. Kearley, Mater. Res. Soc. Symp. Proc., Vol.840 (2005) Q7.12.

Abstract

X-ray diffraction with hard X-rays ($E = 70$ keV) was used to investigate the grain nucleation and grain growth during solidification of a grain refined Al-0.3Ti-0.02B (wt.%) alloy. The investigations showed for the first time the nucleation profile during solidification and how nucleation rate increases with cooling rate. The results indicate that the nucleation process is complete for solid fraction below 30 %, irrespective of the cooling rate. This is explained in terms of the release of latent heat during solidification. The growth of individual aluminum grains during solidification is experimentally observed and compared to model predictions for the diffusion limited grain growth. The experimental results are only in agreement with the theory in the first stage of the transformation. The difference between the experiment and the theory is discussed qualitatively.

7.1.1 Introduction

Al-Ti-B master alloys have been used commercially for the grain refinement of aluminum alloys for over last 30 years. These master alloys contain micrometer size TiB_2 and $TiAl_3$ particles together with solute titanium. When added to molten aluminum alloys these particles enhance the nucleation of α -aluminum grains while the partitioning of solute titanium at the solid-liquid interface controls the grain growth during solidification. This grain refinement process results in a reduced grain size and improved mechanical properties of the final solid product [1]. Despite intensive study, a rigorous mechanism explaining the grain refinement of aluminum alloys by Al-Ti-B master alloys remains a matter of controversy [2,3]. It is observed that as few as 1 % of the particles added to the melt nucleate the aluminum grains. The remaining particles are of no inherent value to the final product, however the agglomeration of these particles may induce defects resulting in poor surface properties of the solidified material. The prevailing aim is therefore to understand the nucleation kinetics and growth of individual grains during solidification of these grain refined aluminum alloys. This can help to develop more efficient grain refiners, to control the microscopic structure during solidification, and improve the mechanical properties of the solidified material.

7.1.2 Experimental

Time dependent X-ray diffraction measurements were carried out during the solidification of an Al-0.3Ti-0.02B (wt.%) alloy. The investigated sample was prepared from an Al-5Ti-0.2B (wt.%) commercial master alloy (KBM AFFILIPS). The sample was kept molten for six hours to let the large size particles sink to the bottom so that the settling of TiB_2 particles does not play a significant role during the X-ray diffraction experiments. The bottom part was removed and the remaining sample was homogenised. The chemical composition of the sample material was analysed using X-Ray Fluorescence Spectrometer (XRF). The results showed that the Al-0.3Ti-0.02B sample contained 0.2 wt.% iron as the main impurity. The particle size of the TiB_2 nucleants in the Al-0.3Ti-0.02B alloy was then determined by optical microscopy and showed a particle size distribution in the range from 0.6 to 2.2 μm with a maximum around 1.2 μm .

The investigated sample was a cylindrical rod with a diameter of 5 mm and a height of 10 mm. The X-ray diffraction experiments were performed on the 3 Dimensional X-ray diffraction microscope [4, 5] of the instrument ID11 at the European Synchrotron Radiation Facility (ESRF). A schematic layout of the experimental setup is shown in figure 7.1. A monochromatic X-ray beam with an energy of 70 keV and a photon flux of $\sim 1.3 \times 10^{11}$ cps was used. Two different beam sizes of $200 \times 200 \mu\text{m}^2$ and $300 \times 300 \mu\text{m}^2$ were applied. Images of the diffracted beam were acquired in transmission geometry by a CCD camera.

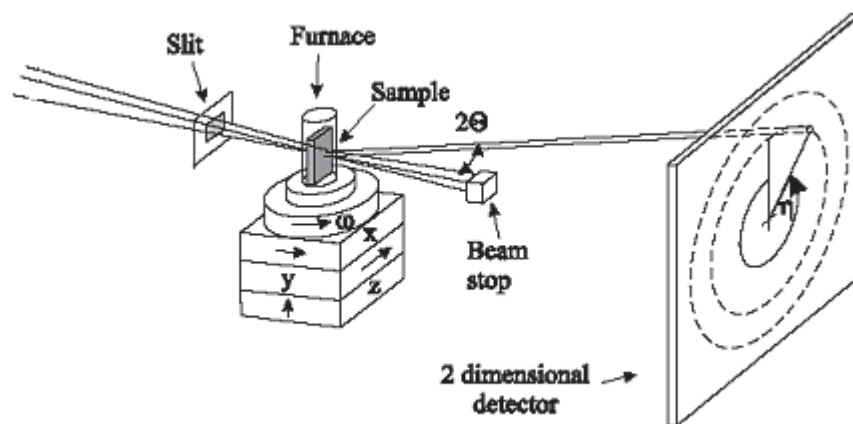


Figure 7.1 Schematic layout of the experimental X-ray diffraction set-up. A monochromatic beam of hard X-rays defined by slits illuminates the sample mounted in a vacuum furnace. The diffracted intensity, scattered over an angle 2θ , is monitored by a two dimensional detector while the sample is rotated over an angle ω around the vertical axis. The direct beam is shielded from the detector by a beam stop.

The samples were placed in a cylindrical container of a glassy carbon with height of 25 mm, an inner diameter of 5 mm, and a wall thickness of 1 mm. The sample container was placed into a Quartz tube that was vertically aligned inside an X-ray transparent furnace. The furnace is fixed to a rotation table enabling sample rotations around the vertical axis. Operated in vacuum the experiments involved continuous cooling of molten samples, from 973 K to 800 K, with different cooling

rates ranging from 1 K/min to 40 K/min. The molten samples were held at 973 K for 30 minutes prior to the continuous cooling.

For illustration, raw images acquired during the liquid to solid phase transformation of the investigated sample at a cooling rate of 40 K/min are shown in Figure 7.2. The illumination time for each displayed diffraction pattern is 1 sec using the beam size of $300 \times 300 \mu\text{m}^2$. The time interval between consecutive diffraction patterns is 14 sec. The diffraction pattern from the molten sample (a) displays the two characteristic liquid rings L_1 and L_2 associated with the short-range order in the molten aluminum. The amount of grain refiners present in the aluminum alloy is found to cause no significant change in the short-range order of the liquid aluminum. The subsequent diffraction patterns during cooling comprises of diffraction spots from aluminum grains, which nucleate in the beginning and grow till virtually no intensity is left in the liquid rings, indicating that the phase transformation is complete.

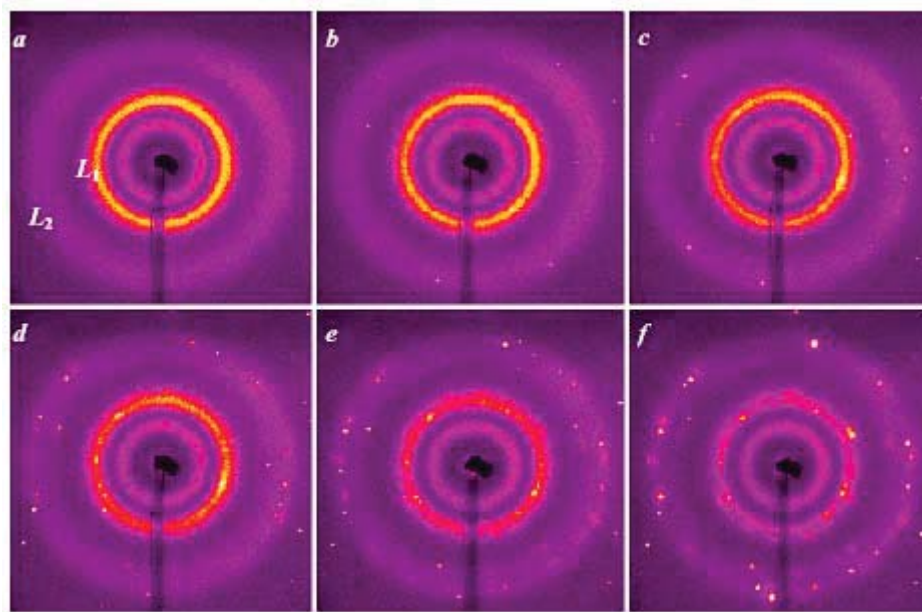


Figure 7.2 X-ray diffraction patterns of the Al-0.3Ti-0.02B alloy showing the liquid to solid (a to f) phase transformation during solidification at a cooling rate of 40 K/min. The two broad outer rings L_1 and L_2 in (a) correspond to first and second peak in the liquid structure factor of molten aluminum before solidification. The inner most ring with a constant intensity during the phase transformation is due to the diffuse scattering from the glassy structure of the quartz tube of the furnace. The bright spots originate from diffraction of individual grains.

The measuring procedure aimed to determine both the nucleation rate and the size of the grains, by measuring the number and the integrated intensity of the diffraction spots. In order to measure the nucleation rate of α -aluminum grains, the beam size was set to $200 \times 200 \mu\text{m}^2$, thereby defining a gauge volume of $V_{\text{gauge}} = 200 \times 200 \times 5000 \mu\text{m}^3$, and the sample was rotated over $\Delta\omega = 1$ degree during exposure. So-called validation tests were made after every exposure by increasing the beam size to $300 \times 300 \mu\text{m}^2$. With these settings subsequent exposures were recorded during the entire continuous cooling with a time resolution of 7 seconds. By comparing the integrated intensities of the diffraction spots for two different beam sizes, we tested whether the associated grain nucleated in the illuminated gauge volume and did not

grew into the gauge volume from its neighbourhood. The time of nucleation of a grain corresponds to the moment when the integrated intensity of a reflection from a single grain I_g is $I_g > I_b + 2\sigma$, where I_b is the background intensity and σ the corresponding standard deviation in the background intensity. By counting number of diffraction spots during solidification, the nucleation rate was obtained.

In order to measure the growth of individual grains a slightly different route was adopted. The same beam sizes of $200 \times 200 \mu\text{m}^2$ and $300 \times 300 \mu\text{m}^2$ were used alternatively to take four consecutive exposures. During each exposure the sample was rotated over $\Delta\omega = 1$ degree, covering a complete oscillation of 3 degrees for each beam size. The diffraction spots that were found to be fully illuminated in the two central exposures were taken as valid spots.

7.1.3 Results and discussion

7.1.3.1 Nucleation rate

The experimental nucleation rate of the aluminum grains and the corresponding change in the solid fraction f_s during solidification, at different cooling rates, is shown in figure 7.3. The solid phase fraction f_s is estimated from the

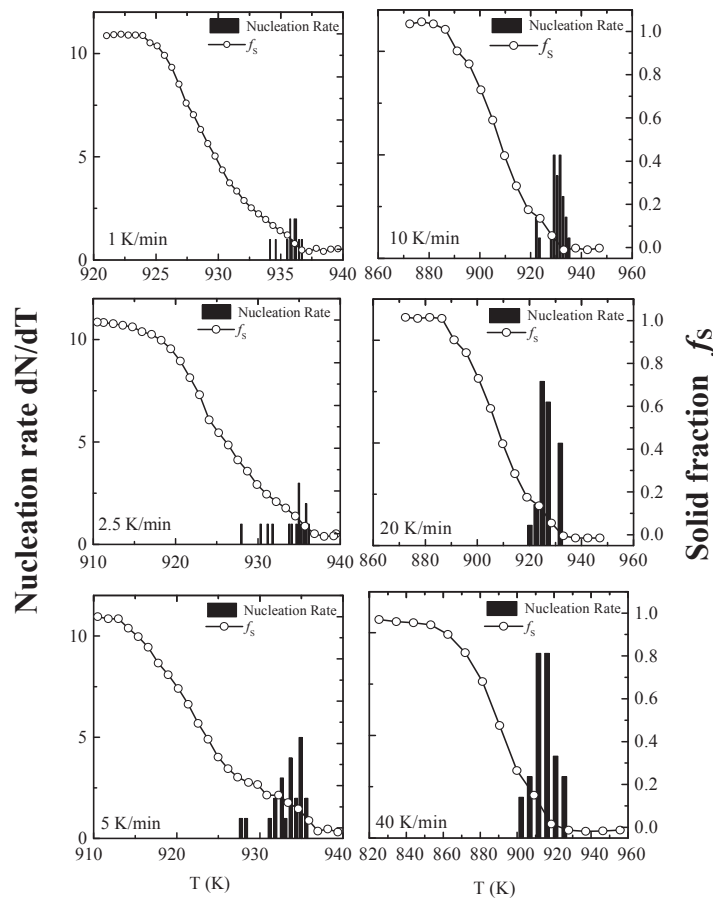


Figure 7.3 The experimental nucleation rate dN/dt and the solid fraction f_s as a function of temperature during solidification of the Al-0.3Ti-0.02B (wt.%) alloy at cooling rates ranging from 1 to 40 K/min.

normalized variation in the intensity of the first liquid peak [6, 7].

The number of aluminum nuclei is found to increase rapidly during solidification once the critical undercooling ΔT needed to activate grain nucleation on the surface of grain refining particles is reached. The undercooling ΔT corresponds to the difference between the melting temperature and the freezing temperature. The total number of nucleated grains is found to be much less than the nucleating TiB_2 particles in the liquid. It is long suggested that the critical undercooling varies for different added particles, as the nucleation efficiency of a particle strongly depends on its size and the interaction between its surface and the melt, called wetting [8]. The results indicate that the nucleation rate increases with cooling rate. The higher undercooling observed for increasing cooling rates, makes it possible that relatively less effective particles activate grain nucleation. It is interesting to note that for all cooling rates, the nucleation process is complete for solid fractions of $f_s \leq 0.3$. The growth of nucleated grains leads to a significant release of latent heat [9]. This limits the undercooling ΔT available to activate later nucleation events as the transformation proceeds. Thus the results indicate that the effectiveness of grain refining particles strongly depends on the spectrum of undercoolings at which the grain nucleation occurs.

7.1.3.2 Grain growth

The kinetics of grain growth is equally important for grain refinement. The grain growth depends on the solute partitioning at the grain boundaries and is controlled by the long-range solute diffusion. The grain volume V_g of the observed diffraction spots (Fig. 7.2), is related to the integrated intensity I_g by the following equation [10, 11],

$$I_g = \Phi_0 r_0^2 \frac{\lambda^3 |F_{hkl}|^2 V_g(t)}{\Delta\omega |\sin \eta| v^2} L_g P T_r \exp(-2M). \quad (7.1)$$

where Φ_0 is the incident flux of photons, F_{hkl} is the structure factor of $\{hkl\}$ reflection, λ is the photon wavelength, $\Delta\omega$ is the angular range over which the grain is rotated, v is the volume of the unit cell, P is the polarization factor, T_r is the transmission factor, L_g the lorentz factor, η is the angle shown in figure 7.1, and r_0 is the Thomson scattering length. The growth behaviour of two aluminum grains during solidification at a cooling rate of 1K/min is shown in Figure 7.4. The solid line represents the theoretical prediction for the diffusion-controlled growth of aluminum grains during solidification, given by [12, 13]:

$$R(t) = \lambda_s \sqrt{D_s(t-t_0)}, \quad (7.2)$$

where $R(t)$ is the radius of the spherical grain at time t , λ_s is the kinetic parameter that originates from partitioning of solute titanium during solidification [13], and $D_s \approx 5 \mu\text{m}^2/\text{sec}$ [14] is the diffusion coefficient of solute titanium in liquid aluminum. The experimental curves are in agreement with the theory only in the beginning of the phase transformation. The results show that the aluminum grain, once nucleated, grows rapidly in the beginning while the growth rate decreases gradually as the

transformation proceeds. This decrease in growth rate can qualitatively be explained by the release of latent heat and the segregation of solute iron during the phase transformation.

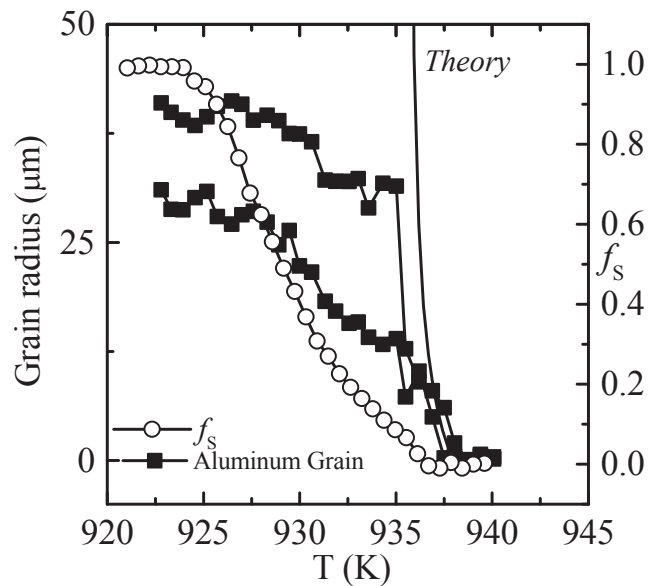


Figure 7.4 The radius of individual aluminum grains (■) and the evolution of the solid fraction f_s (○) as a function of temperature during solidification at a cooling rate of 1 K/min. The solid line indicates the model calculation of Equation 7.2, for diffusion-controlled grain growth.

The grain, once nucleated it requires certain undercooling to grow, though less than that needed for nucleation. As observed in figure 7.3, the release of latent heat stops the nucleation process for $f_s \approx 0.2$. This evolution of latent heat removes the undercooling and reduces the grain growth. In addition, the segregation of iron during the phase transformation is important. The partition coefficient k_{Fe} of iron in aluminum is $k_{Fe} = 0.02$ [2]. Once the transformation starts, the iron concentration gradually increases in the liquid at the solid/liquid interface of the growing grain during solidification. For an aluminum grain to grow, iron needs to diffuse away from the interface into the liquid. Thus as the transformation proceeds this becomes a rate-limiting factor and leads to the growth retardation.

7.1.4 Conclusions

The experimental results show for the first time how the nucleation process evolves within the bulk of the melt during solidification of aluminum alloys. Despite the presence of efficient nucleating particles and increasing cooling rates, the release of latent heat is found to be important. It strongly limits the nucleation rate as well as grain growth during solidification.

Acknowledgments

This work was financially supported in part by the Foundation for Fundamental Research on Matter (FOM) of the Netherlands Organisation for

Scientific Research (NWO) and the Netherlands Institute for Metals Research (NIMR). We are thankful to the European Synchrotron Radiation Facility (ESRF) for providing beam time to perform these experiments. Special thanks to G. Vaughan and A. Götz for assistance in using beamline ID11.

References

- [1] D. G. McCartney, *Int. Mater. Rev.* 34, 247 (1989).
- [2] M. Easton and D. StJohn, *Met. Mater. Trans.* A30, 1613 (1999).
- [3] M. Easton and D. StJohn, *Met. Mater. Trans.* A30, 1625 (1999).
- [4] H. F. Poulsen, S. Garbe, T. Lorentzen, D. J. Jensen, F. W. Poulsen, N. H. Andersen, T. Frello, R. Feidenhans, and H. Graafsma, *J. Synchrotron Rad.* 4, 147 (1997).
- [5] H. F. Poulsen, *Three Dimensional X-Ray Diffraction Microscopy, Mapping Polycrystals and Their Dynamics*, (Springer Tracts in Modern Physics, Vol. 2005).
- [6] N. Iqbal, N. H. van Dijk, V. W. J. Verhoeven, W. Montfroiij, T. Hansen, L. Katgerman, and G. J. Kearley, *Acta. Mater.* 51, 4497 (2003).
- [7] N. Iqbal, N. H. van Dijk, V. W. J. Verhoeven, T. Hansen, L. Katgerman, and G. J. Kearley, *Mater. Sci. And Engg. A* 367, 82 (2004).
- [8] A. C. Zettlemoyer, In: *Nucleation*, (Marcel Dekker Inc., New York, 1969).
- [9] I. Maxwell and A. Hellawell, *Acta Metall.* 23, 229 (1975).
- [10] J. Als-Nielsen and D. McMorrow, In: *Elements of Modern X-ray Physics*, (Wiley, West Sussex, 2001).
- [11] B. E. Warren, In: *X-ray Diffraction*, (Dover Publications, New York, 1990).
- [12] H. B. Aaron, D. Fainstein, and G. R. Kotler, *J. Appl. Phys.* 41, 4405 (1970).
- [13] A. L. Greer, A. M. Bunn, A. Tronche, P. V. Evans, and D. J. Bristow, *Acta. Mater.* 48, 2823 (2000).
- [14] G. S. Ershov, A. A. Kasatkin, and A.A. Golubev, *Russian Metallurgy* 2, 62 (1978).

7.2 Evolution of the metastable TiAl_3 phase

The appearance of few diffraction spots prior to nucleation of aluminum grains is observed during slow cooling of the liquid Al-0.3Ti-0.02B alloy. The scattering angles corresponding to these diffraction spots fit to those of the tetragonal structure (space group $I4/mmm$) of TiAl_3 phase with unit cell dimensions $a = 3.84 \text{ \AA}$, $c = 8.58 \text{ \AA}$. The TiAl_3 grains appear prior to solidification of aluminum and grow in size until the solidification starts. The evolution of the aluminum solid fraction and the radius of the TiAl_3 grains during continuous cooling at slow cooling rates of 1 and 2.5 K/min is shown in figure 7.5.

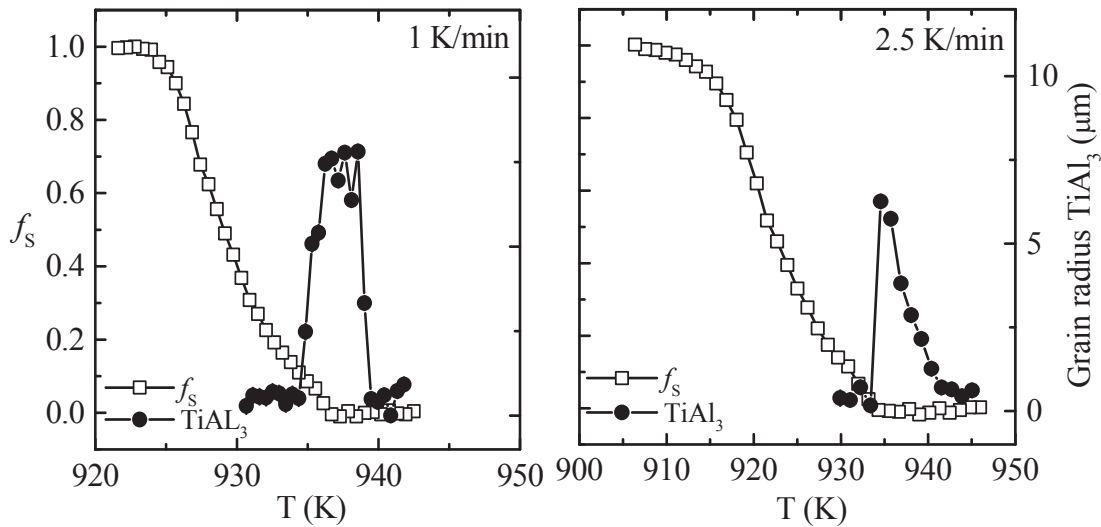


Figure 7.5 Evolution of the solid fraction of aluminum (\square) and the radius of TiAl_3 grains (\bullet) during the liquid to solid phase transformation of the Al-0.3Ti-0.02B alloy at slow cooling rates of 1 and 2.5 K/min.

Upon nucleation of α -aluminum grains during continuous cooling, the TiAl_3 grains cease to grow and their radius decreases with a further decrease in temperature. According to the Al-Ti phase diagram, the TiAl_3 is a stable phase in this hyperperitectic aluminum alloy, above the melting temperature. However such observation of the evolution of a TiAl_3 phase with in the melt has not been reported earlier.

The role played by the TiAl_3 phase in the nucleation of α -aluminum during solidification of grain refined aluminum alloys has been a matter of speculations. The TiAl_3 substrate is considered to be a better nucleation site for aluminum grains than the TiB_2 particles, and hence, responsible for grain refinement. Previously Mohanty et al. have confirmed this mechanism and reported the existence of TiAl_3 layer sandwiched between the TiB_2 surface and the aluminum grains, in grain refined aluminum alloys. Our experimental observations support those reported by Mohanty et al. It suggests that the surface of TiB_2 particles, nucleate TiAl_3 grains prior to the solidification of aluminum. However these TiAl_3 grains exhibit a metastable behavior. The TiAl_3 grains dissolve upon solidification of aluminum and most probably nucleate the aluminum grains through the peritectic reaction

7.3 Real-time observation of grain nucleation and growth during solidification of aluminum alloys

N. Iqbal, N. H. van Dijk, S. E. Offerman, M. Moret, L. Katgerman, and G. J. Kearley, Acta Mater. (Article in press).

Abstract

The crystallisation kinetics of liquid aluminum-titanium alloys with microscopic TiB_2 particles added to refine the grain size in the solidified material was studied by X-ray diffraction measurements at a synchrotron source. Real-time observation of the formation and growth of individual grains reveals the central role played by the added TiB_2 particles during solidification. Prior to the main transformation, weak reflections of a metastable TiAl_3 phase were detected. This observation finally pinpoints the highly debated mechanism responsible for enhanced grain nucleation in Al-Ti-B alloys.

7.3.1 Introduction

Liquid-to-solid phase transformations often form an essential step in the processing of polycrystalline materials. A detailed understanding of this phenomenon is of both fundamental interest and technological importance for the formation of many polycrystalline materials. During solidification two processes can be identified: grain nucleation and subsequent grain growth [1]. At the time of nucleation a small cluster of the solid phase, which fluctuates in size, reaches a dimension that can no longer remelt. During grain growth the stable nuclei increase in size until the material is completely solidified.

The current understanding of grain nucleation is still limited due to the experimental difficulty of monitoring the formation of relatively small nuclei in the bulk of the material and the computation resources needed to evaluate the stability of the fluctuating clusters in the melt. Recent advances in this field are laser confocal microscopy experiments [2] and numerical simulations [3] on the crystallisation behaviour of colloids. For liquid metals few experimental techniques are available to probe the nucleation and growth of individual grains within the melt. The recent development of X-ray diffraction microscopes at synchrotron sources with high-energy X rays has created the opportunity to study individual grains in the bulk of a material [4-6]. In a recent study [7] this technique was used to probe both nucleation and growth of individual grains for a solid-state phase transformation within the bulk of a steel sample. The present X-ray diffraction study represents the first determination of the nucleation and growth behaviour of individual grains within the melt during solidification of a metal. The relatively high viscosity of the liquid metal with minimal grain rotations allowed us to monitor the complete growth of individual grains floating in the melt.

The mechanical properties of polycrystalline materials depend critically on the average grain size, which often improve as the average grain size is reduced. Generally, grain refinement in metals can be achieved by adding micron-sized particles to the melt [8]. These particles are thought to cause an enhanced nucleation of the solid grains on the surface of the added particles. The mechanism underlying this process of grain refinement with added particles is however, still unclear [9-11].

In aluminum alloys with added TiB_2 particles it was found that grain refinement is only effective if a small concentration of solute titanium is added to the melt. However, for these small concentrations of solute titanium no additional phases, which could assist the nucleation of aluminum grains on the added particles, are expected to form according to the phase diagram. This controversy has led to a wide variety of models proposed to explain the influence of the solute titanium on the grain nucleation in these alloys. In this study we demonstrate that a metastable phase plays a key role in the enhanced grain nucleation in liquid aluminum alloys. We directly observe that grain nucleation only occurs in the first stage of the transformation and that the grain growth initially follows the model prediction for diffusion-controlled growth without interactions between the grains.

7.3.2 Experimental

7.3.2.1 Sample preparation

The aluminum alloys were prepared from pure Al (99.999%) and Ti (99.99%) from Goodfellow, and TiB_2 (99.99%) from GE Advanced Ceramics. The Al and Ti were melted in the appropriate ratios in an arc furnace under high purity argon, solidified and remolten for 5 times to obtain a homogeneous alloy. The solute concentration of 0.097(5) wt.% Ti in the alloy was determined by X-ray fluorescence spectroscopy. The TiB_2 particles with a size distribution between 3 and 6 μm and a maximum around 4.4 μm were then added to the reheated liquid metals and homogeneously distributed by stirring to prepare solid mixtures for the X-ray diffraction experiments. As the high purity TiB_2 particles were not heated before entering the melt we expect oxidation to be minimal. The relatively small size of the TiB_2 particles leads to a minimal effect of settling during the experiment.

7.3.2.2 Experimental procedure

X-ray diffraction measurements were performed using the three dimensional X-ray diffraction microscope (3DXRD) at beam line ID11 of the European Synchrotron Radiation Facility in transmission geometry. The experimental set-up is shown in Figure 7.6. A monochromatic X-ray beam with an energy of 70 keV (wavelength of 0.177 Å) and a beam size of $200 \times 200 \mu\text{m}^2$ illuminated the 5 mm diameter of the sample (with a height of 10 mm) that was mounted in a glassy carbon container within the vacuum furnace. A continuous sample rotation of 1° around around the vertical axis (perpendicular to the beam) gives rise to a diffraction pattern on the two-dimensional detector that is placed behind the sample. This pattern gives direct information on both the liquid and solid phases during the solidification process.

In order to probe grain nucleation during solidification the beam size was enhanced from $200 \times 200 \mu\text{m}^2$ to $300 \times 300 \mu\text{m}^2$ on each alternate exposure in order to check that the grains nucleated in the smaller central beam. Reflections that first appeared during exposure with the larger beam were discarded as nucleation events because they cannot be distinguished from grains that nucleated outside the illuminated sample volume and grew into it.

In order to probe the grain radius of individual grains it is essential that the total grain volume is illuminated and the complete integrated intensity of the reflection is recorded. During the X-ray diffraction measurements four subsequent

exposures were collected while the sample was continuously rotated around the vertical axis by 1° per exposure. In order to determine whether the complete integrated intensity was observed in one of the two central exposures, the intensity was compared to those of the two neighbouring rotation intervals. On alternate sets of exposures the beam size was enhanced from $200 \times 200 \mu\text{m}^2$ to $300 \times 300 \mu\text{m}^2$ to check that the total grain volume was illuminated by the smaller central beam. Only grains that fulfilled both conditions were considered [4]. The absolute size of the grain was determined by an internal calibration of the Bragg intensity to the intensity of the first peak in the liquid structure factor.

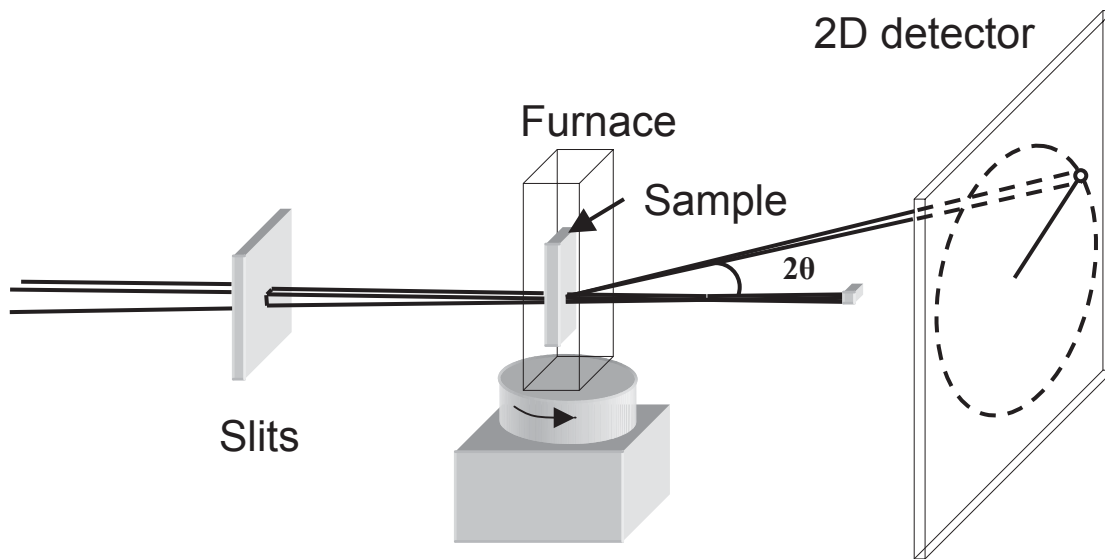


Figure 7.6 Schematic outline of the experimental X-ray diffraction set-up. A monochromatic beam of hard X-rays defined by slits illuminates the sample mounted in a vacuum furnace. The diffracted intensity, scattered over an angle 2θ , is monitored by a two dimensional detector while the sample is rotated over an angle ω around the vertical axis. The direct beam is shielded from the detector by a beam stop.

7.3 Results and discussion

7.3.3.1 X-ray diffraction patterns

Figure 7.7 shows the diffraction pattern of an aluminum alloy with solute titanium and added TiB_2 particles at three stages during continuous cooling. In the liquid phase (Fig. 7.7a) two broad rings indicate the maxima in the liquid structure factor resulting from short-range order of the aluminum atoms. In the mixed phase (Fig. 7.7b) the intensity of the broad rings is reduced, and a limited number of diffraction spots from the solid grains is observed at the diffraction angles corresponding to reflections of the face-centred cubic lattice structure of aluminum. In the solid phase (Fig. 7.7c) the broad rings of the liquid phase are absent and the diffraction spots show an increase in number and intensity. According to standard diffraction theory the number of spots detected is proportional to the number of illuminated grains and the intensity of each

spot is proportional to the volume of the grain from which it originates. The liquid phase fraction f_l , and consequently also the solid phase fraction $f_s = 1 - f_l$, can be determined accurately by scaling the intensity variation of the first diffuse ring of the liquid pattern at a part of the ring in which no diffraction spots of the solid phase appear. By repeated acquisition of images, the nucleation and growth of individual grains were studied with a typical time resolution of 8 s.

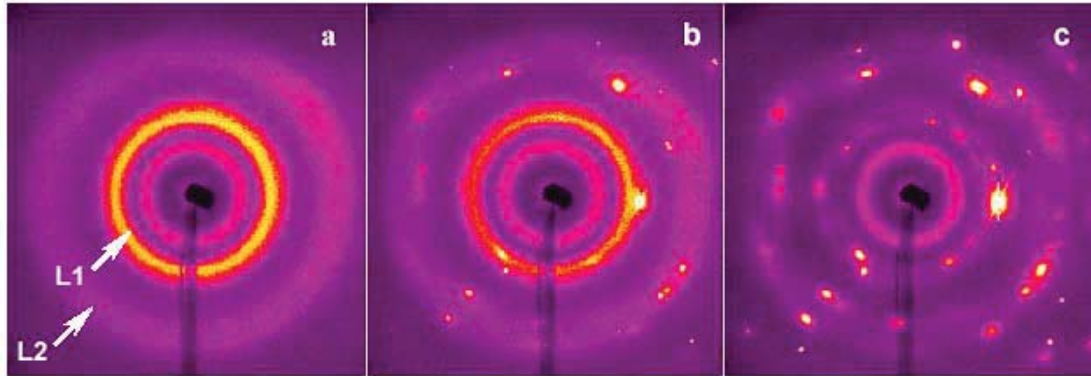


Figure 7.7 X-ray diffraction patterns of the aluminum alloy with solute titanium (0.1 wt.%) and added TiB_2 particles (0.1 wt.%) at different stages of the solidification process. The data were collected during cooling from 973 K at a rate of 1 K/min. (a) In the liquid phase the two broad outer rings are due to the first (L1) and second (L2) maximum in the liquid structure factor. (b) In the mixed phase additional bright spots are Bragg reflections from nucleated grains at the scattering angles of the aluminum lattice structure. (c) In the solid phase the diffraction spots have increased in number and intensity while the diffuse scattering of the liquid phase has vanished. The diffuse innermost ring arises from the quartz windows of the vacuum furnace.

7.3.3.2 Grain nucleation

The aluminum alloys were kept for 30 min at 973 K (about 40 K above the melting temperature of aluminum) in order to form a homogeneous liquid phase, and were subsequently cooled at a rate of 1 and 10 K/min. In Figure 7.8 the number of nucleated grains and the solid phase fraction is shown as a function of time for three aluminum alloys at different cooling rates. By counting the number of diffraction spots as a function of time, the evolution of the number of aluminum grains in reflection was obtained (for grains with a radius above the detection limit of about 2 μm for the main aluminum reflections). From all reflections on the detector only the grains that nucleated in the illuminated sample volume were considered and the grains that grew into it were discarded. The observed number of grains that fulfil the Bragg condition is proportional to the grain density (within a relative statistical uncertainty of $1/\sqrt{N}$). The corresponding solid phase fraction was determined from the scaled intensity at the first ring in the diffraction pattern of the liquid phase. When the final number of reflecting grains in Figure 7.8 is compared for the different alloys, significantly more are found for the alloy containing both solute titanium and added

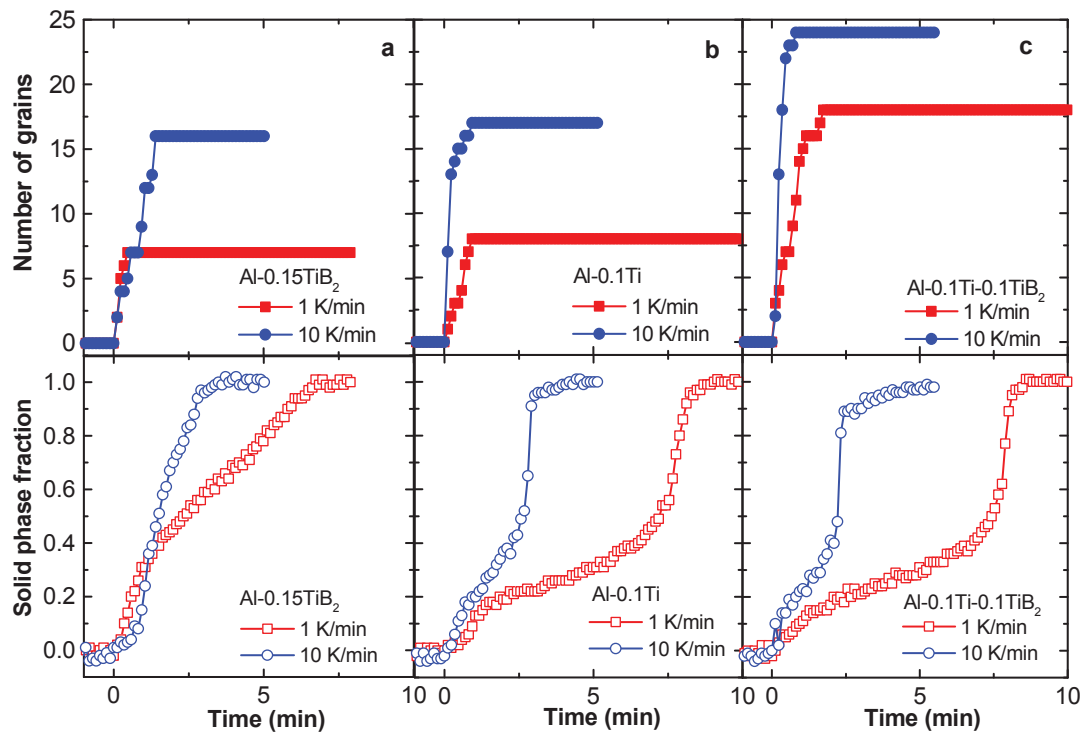


Figure 7.8 Grain nucleation and solid phase fraction of three aluminum alloys as a function of time for different cooling rates. X-ray diffraction patterns were monitored as a function of time for aluminum alloys with (a) added TiB_2 particles (0.15 wt.%), (b) solute titanium (0.1 wt.%), and (c) both solute titanium (0.1 wt.%) and added TiB_2 particles (0.1 wt.%) during cooling from 973 K with a cooling rate of 1 and 10 K/min. The upper frames show the total number of nucleated grains in reflection (after validation that they nucleated in the illuminated sample volume). The lower frames show the corresponding solid phase fraction deduced from the scaled intensity variation in the first maximum of the liquid structure factor. The time, $t = 0$ min, corresponds to the onset of the solidification.

microscopic TiB₂ particles. This clearly confirms that grain refinement is only effective when both solute titanium and added microscopic TiB₂ particles are present [9-11]. Further, our measurements in Figure 7.8 demonstrate that the nucleation process is limited to the initial stage of the solidification and is complete at a solid phase fraction of about 20% for all samples. This remarkable observation indicates that the energy barrier for nucleation increases strongly after a considerable fraction of the solid phase fraction has been formed. According to the classical nucleation theory [12] the energy barrier for nucleation on a substrate ΔG^* corresponds to:

$$\Delta G^* = \left(\frac{16\pi}{3} \right) \left(\frac{\sigma^3}{\Delta G_v^2} \right) F(\theta), \quad (7.3)$$

where σ is the energy of the new interface, $\Delta G_v \approx L\Delta T/T_m$ is the driving force of the nucleation, L is the latent heat, ΔT the undercooling below the liquidus temperature T_m , and $F(\theta) = (2 + \cos\theta)(1 - \cos\theta)^2/4$ is a function of the wetting angle, θ , between the solid phase and the substrate. The increase in the nucleation barrier during solidification is caused by an increase in the local sample temperature as latent heat is released [13]. For all samples the number of nuclei formed increases with cooling rate indicating that the maximum undercooling reached during solidification increases for higher cooling rates. As grain nucleation requires a minimum amount of undercooling to be effective, most potential nucleation sites become inactive when the temperature rises due to the release of latent heat from the previously nucleated grains. As a consequence, only a small fraction of the TiB₂ particles, which is controlled by the maximum undercooling and the wetting angle, actually nucleates a grain during the transformation. From the data in Fig. 7.8 we can further conclude, in agreement with previous studies [9-11], that an effective wetting of the TiB₂ substrate is only observed when solute titanium is present. The retarded growth caused by the diffusion of solute titanium is often thought to play an important role in the grain refinement as there is more time for nucleation events to occur [10,13]. Although a retarded grain growth in the presence of solute titanium indeed delays a recalescence and thereby increases the maximum undercooling reached for aluminum alloys with added TiB₂ particles, the grain nucleation was not found to extend over significantly longer times. Apparently, the enhanced grain nucleation is predominantly caused by the improved wetting of the TiB₂ substrate in the presence of solute titanium and to a lesser extent by a retarded growth.

7.3.3.3 Grain growth

The growth behaviour of individual aluminum grains during solidification was determined by monitoring the intensity of the diffraction spots continuously. In Figure 7.9 the overall growth kinetics of the individual grains is shown for the alloys containing solute titanium with and without added TiB₂ particles. The individual growth curves show a close resemblance to the behaviour of the solid fraction. The observed growth behaviour of the individual grains is controlled by the diffusion of solute titanium and the release of latent heat. As titanium has a strong affinity for the solid phase, its concentration in the melt decreases as the solidification proceeds. For diffusion-controlled growth of non-interacting grains, the grain radius R as a function of time t is given by [14]:

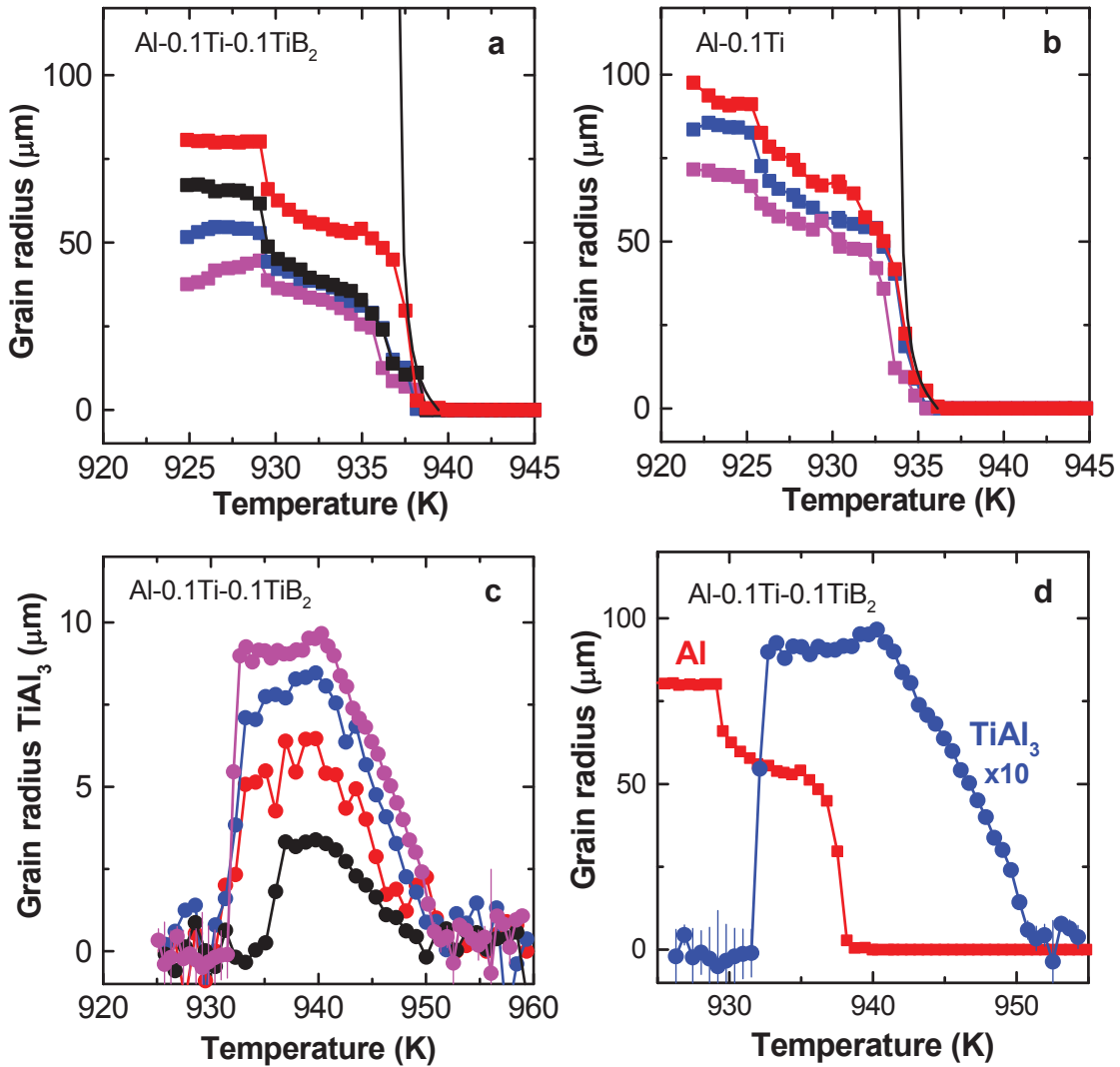


Figure 7.9 Grain growth of individual aluminum and metastable TiAl₃ grains as a function of temperature for two aluminum alloys. The grain radius of individual aluminum grains is shown as a function of temperature during continuous cooling (1 K/min) from 973 K in (a) for the alloy with both solute titanium (0.1 wt.%) and added TiB₂ particles (0.1 wt.%) and in (b) for the alloy with only solute titanium (0.1 wt.%). The grain radius was deduced by assuming a spherical geometry. Solid lines indicate the model calculation for diffusion-controlled growth. The grain radius of individual TiAl₃ grains in the aluminum alloy with solute titanium and added TiB₂ particles is shown in (c) and compared to the growth of an individual aluminum grain in (d). The TiAl₃ grains nucleate about 10 K above the experimental onset of nucleataion for aluminum grains, and become unstable when solid aluminum has formed.

$$R(t) = \lambda_s \sqrt{D_s (t - t_s)}, \quad (7.4)$$

where λ_s is a parameter that is determined from the titanium solubility in the liquid and the solid phases, D_s is the diffusion constant of solute titanium in the liquid [15], and t_s is the moment of nucleation of the grain. In the growth curves of the individual grains shown in Figure 7.9, three different stages can be distinguished. In the first stage the individual growth curves are consistent with the model prediction for diffusion-controlled growth of non-interacting grains. These observations are the first in-situ confirmation that grain growth within the melt of a liquid metal initially obeys the widely applied model of Equation 7.4. After this stage, the growth rate is reduced by an increase in temperature caused by the release of latent heat (and to a minor extent due to the indirect interaction of the growing grains via overlapping diffusion fields), leading to a reduced growth parameter λ_s . Near the end of the transformation the growth rate rapidly increases when the undercooling increases again during our continuous cooling experiment.

7.3.3.4 Metastable TiAl₃

A careful analysis of the measured diffraction patterns shows the presence of a limited number of weak diffraction spots (at a wave-vector transfer of $Q = 4.0, 4.4, 5.6, \text{ and } 6.3 \text{ \AA}^{-1}$) in the alloy with solute titanium and added TiB₂ particles, which could not be indexed as aluminum grains. The most likely origin of these reflections in our high-purity alloy is the presence of a TiAl₃ phase (the spots then correspond to {105}, {204}, and {323} reflections of the tetragonal structure and to a {320} reflection of the metastable cubic structure). It is remarkable that these reflections (Fig. 7.9c) first appear about 10 K above the experimental solidification temperature of aluminum. At the nucleation temperature of the aluminum grains the intensity of the TiAl₃ reflections start to decrease, and finally vanish near the end of the transformation. The absence of these TiAl₃ reflections in the sample containing solute titanium without the added TiB₂ particles shows that the TiAl₃ phase plays an essential role in the enhanced nucleation process as revealed in Figure 7.8. Apparently, the nucleation of TiAl₃ on the TiB₂ substrate is substantially more effective than the nucleation of aluminum. Indeed, one of the many mechanisms proposed to explain the enhanced nucleation in this system, the duplex nucleation theory [9-11], proposes that the TiB₂ particles need to be coated by a thin layer of TiAl₃ in order to be effective nucleant particles. From earlier measurements it is known that once TiAl₃ is formed it acts as an excellent nucleation site for aluminum [16]. Our present in-situ study shows that the TiB₂ substrates stabilise a TiAl₃ phase in a limited temperature range above the solidification temperature of aluminum. This formation of a TiAl₃ phase in aluminum alloys with a titanium concentration below 0.15 wt.%, where it is considered unstable according to the Al-Ti phase diagram, has long been proposed but was so far not supported by experimental evidence due to the lack of in-situ data [10,11].

7.4 Conclusions

Our present study shows that the TiAl₃ phase is metastable for titanium concentrations below 0.15 wt.%, but only in a small temperature range above the solidification temperature of aluminum. The direct correlation between the

observation of this phase and the enhanced nucleation reveals that the duplex nucleation theory is the mechanism responsible for the grain refinement process in these alloys. After the formation of aluminum grains, the TiAl_3 phase subsequently dissolves at the expense of the more stable solid aluminum-titanium alloy. Our present experiments demonstrate that nucleation and growth of individual grains can be studied during solidification within the bulk of liquid metals. These in-situ experiments open the opportunity to validate the theoretical models widely used to predict the solidification process. This is of crucial importance to many industries that use grain refinement to produce solidified materials with favourable mechanical properties. Further, we identified which of the proposed mechanisms is responsible for the grain refinement process in aluminum alloys with added TiB_2 particles.

Acknowledgements

We acknowledge the European Synchrotron Radiation Facility for provision of synchrotron radiation facilities and we would like to thank G. Vaughan and A. Götz for assistance in using beamline ID11. We thank Y. Huang for assistance with the sample preparation. This work was financially supported in part by the Foundation for Fundamental Research on Matter (FOM) of the Netherlands Organisation for Scientific Research (NWO) and the Netherlands Institute for Metals Research (NIMR).

References

- [1] Christian JW. The theory of transformations in metals and alloys. Oxford: Pergamon, 1981.
- [2] Gasser U, Weeks ER, Schofield A, Pusey PN, Weitz DA. *Science* 2001;292:258.
- [3] Auer S, Frenkel D. *Nature* 2001;409:1020.
- [4] Lauridsen EM, Jensen DJ, Poulsen HF, Lienert U. *Scripta Mater* 2000;43:561.
- [5] Margulies L, Winther G, Poulsen HF. *Science* 2001;292:2392.
- [6] Larson BC, Yang W, Ice GE, Budal JD, Tischler JZ. *Nature* 2002;415:887.
- [7] Offerman SE, van Dijk NH, Sietsma J, Grigull S, Lauridsen EM, Margulies L, Poulsen HF, Rekveldt MTh, van der Zwaag S. *Science* 2002;298:1003.
- [8] McCartney DG. *Int Mater Rev* 1989;34:247.
- [9] Schumacher P, Greer AL, Worth J, Evans PV, Kearns MA, Fisher P, Green AH. *Mater Sci Technol* 1998;14:394.
- [10] Easton M, StJohn D. *Metall Mat Trans A* 1999;30A:1613.
- [11] Easton M, StJohn D. *Metall Mat Trans A* 1999;30A:1625.
- [12] Kelton KF. *Solid State Physics Vol 45*. New York: Academic, 1991, p.75.
- [13] Maxwell I, Hellawell A. *Acta Metall* 1975;23:229.
- [14] Zener C. *J Appl Phys* 1949;20:950.
- [15] Ershov GS, Kasatkin AA, Golubev AA. *Russian Metallurgy* 1978;2:62.
- [16] Greer AL. *Phil Trans R Soc Lond A* 2003;361:479.

7.4 Nucleation and grain growth versus cooling rate

The nucleation rate and the corresponding evolution of the solid fraction, f_s , during solidification of Al-0.15TiB₂, Al-0.1Ti, and Al-0.1Ti-0.1TiB₂ alloys at different cooling rates is presented in figure 7.10, figure 7.11, and figure 7.12, respectively. Clearly the undercooling increases with increasing cooling rate, and consequently result in enhanced nucleation. The comparison of three aluminum alloys shows that at a given cooling rate, the nucleation rate is always higher for the Al-0.1Ti-0.1TiB₂ alloy.

Figure 7.13 shows the growth behaviour of several individual aluminum grains during solidification of the Al-0.1Ti-0.1TiB₂ alloy at cooling rates of 2.5, 5 and 10 K/min. The model prediction for diffusion controlled grain growth is also shown. The observed growth behaviour of individual aluminum grains is similar for all the cooling rates. Again, three different stages for grain growth can be distinguished. It is interesting to note that the grains that nucleate earlier during solidification apparently grow bigger in size for all the cooling rates. The model calculations are in reasonable agreement with the experimental data at slow cooling rates. For higher cooling rates, an increasing undercooling is observed before the nucleation starts. However, the initial growth behaviour exhibit a close resemblance with the model predictions even at higher cooling rates.

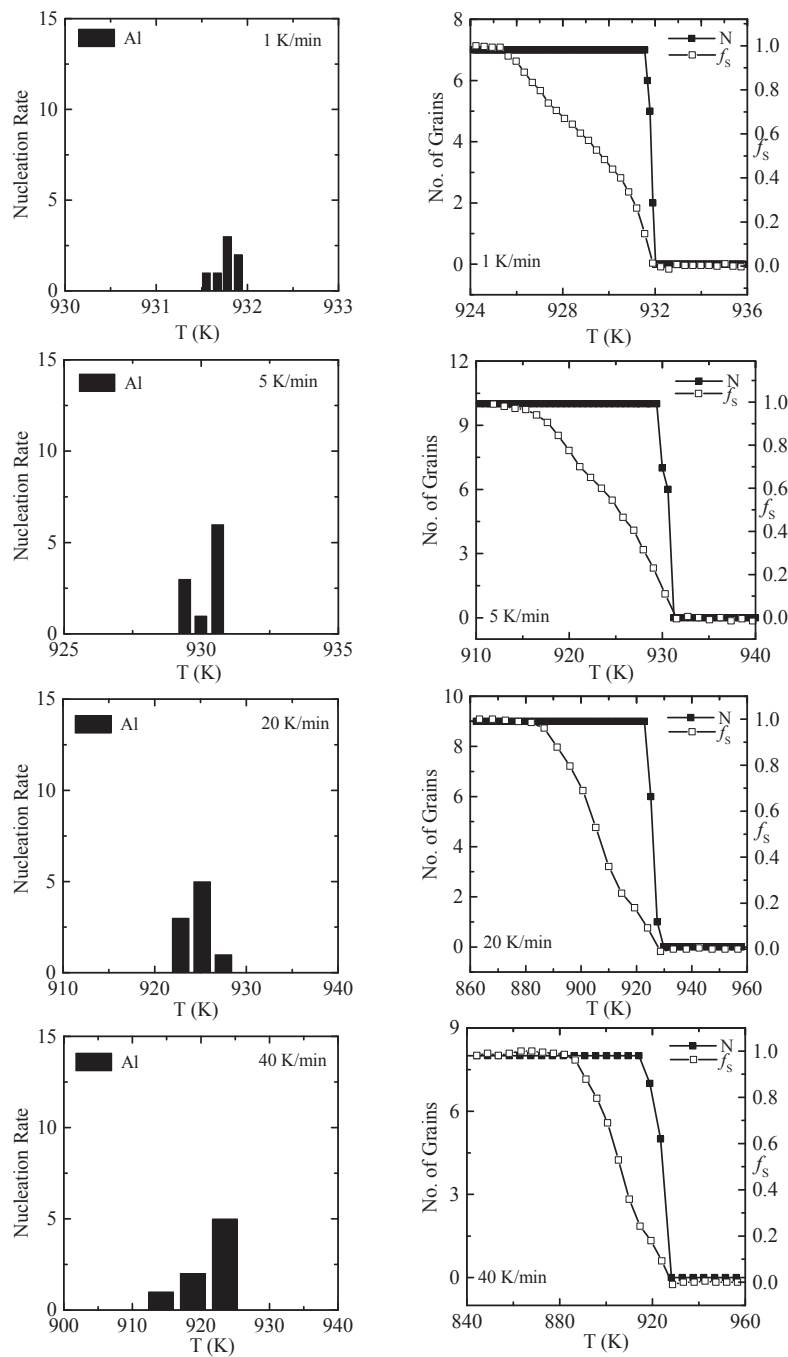


Figure 7.10 The nucleation rate, the number of α -aluminum grains (N) and the corresponding evolution of solid fraction (f_s) as a function of temperature during solidification in the Al-0.15TiB₂ (wt. %) alloys with different cooling rates.

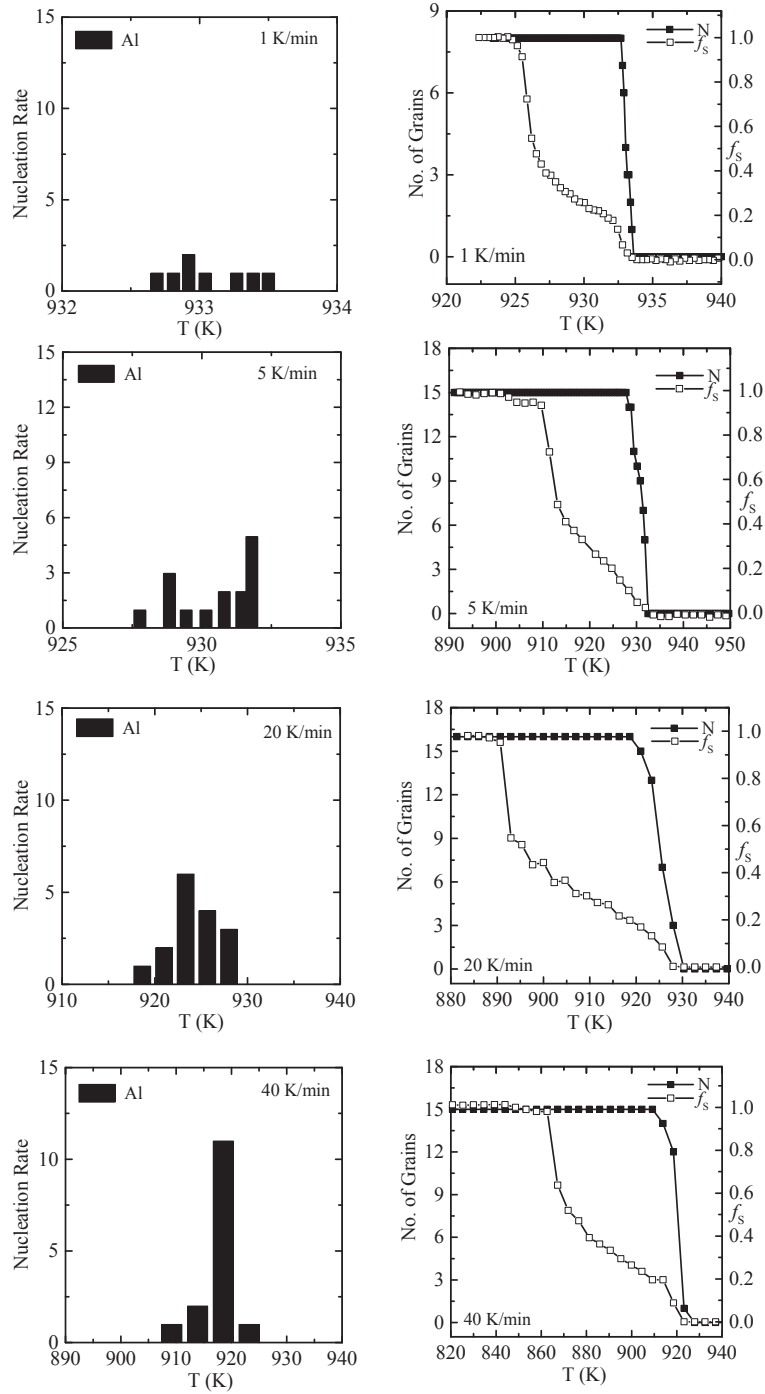


Figure 7.11 The nucleation rate, the number of α -aluminum grains (N) and the corresponding evolution of solid fraction (f_s) as a function of temperature during solidification in the Al-0.1Ti (wt. %) alloys with different cooling rates.

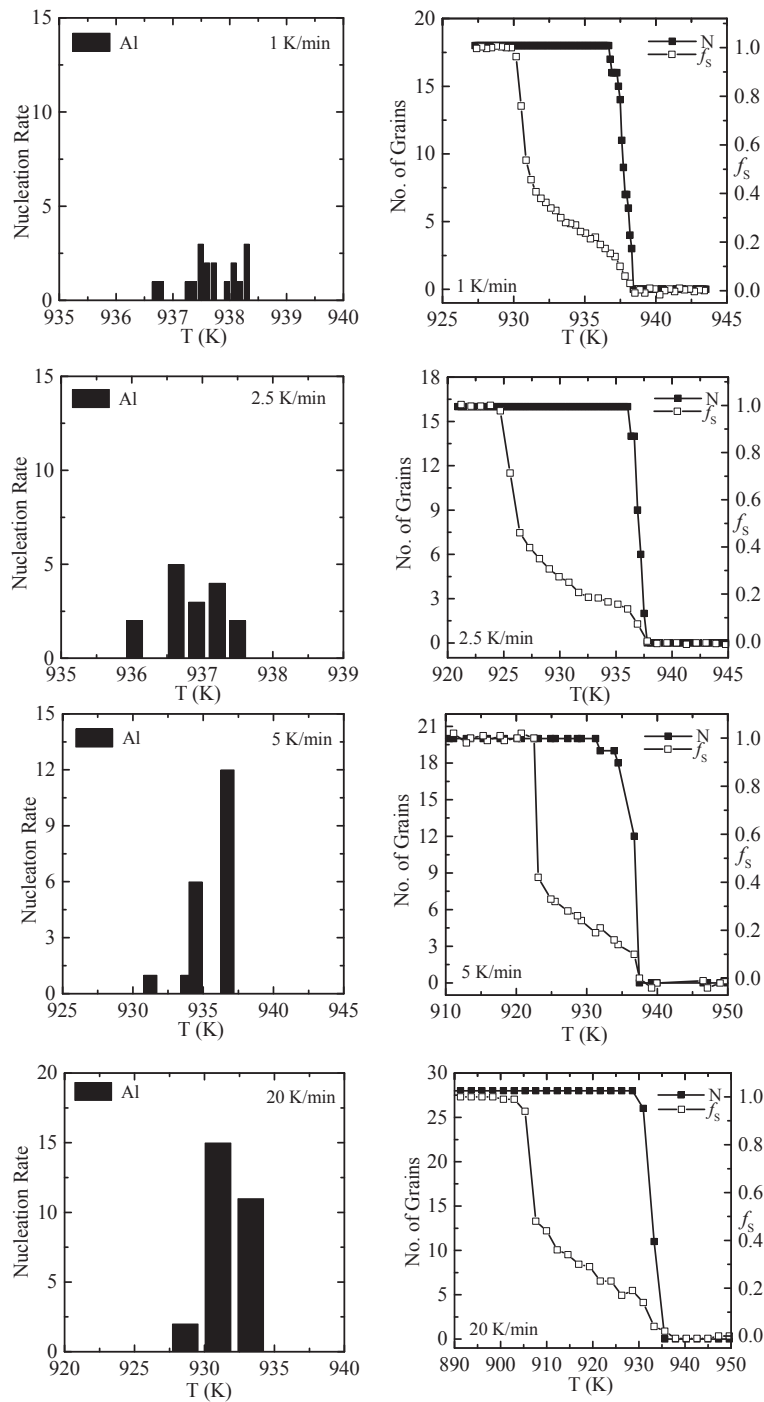


Figure 7.12 The nucleation rate, the number of α -aluminum grains (N) and the corresponding evolution of solid fraction (f_s) as a function of temperature during solidification in the Al-0.1Ti-0.1TiB₂(wt. %) alloys with different cooling rates.

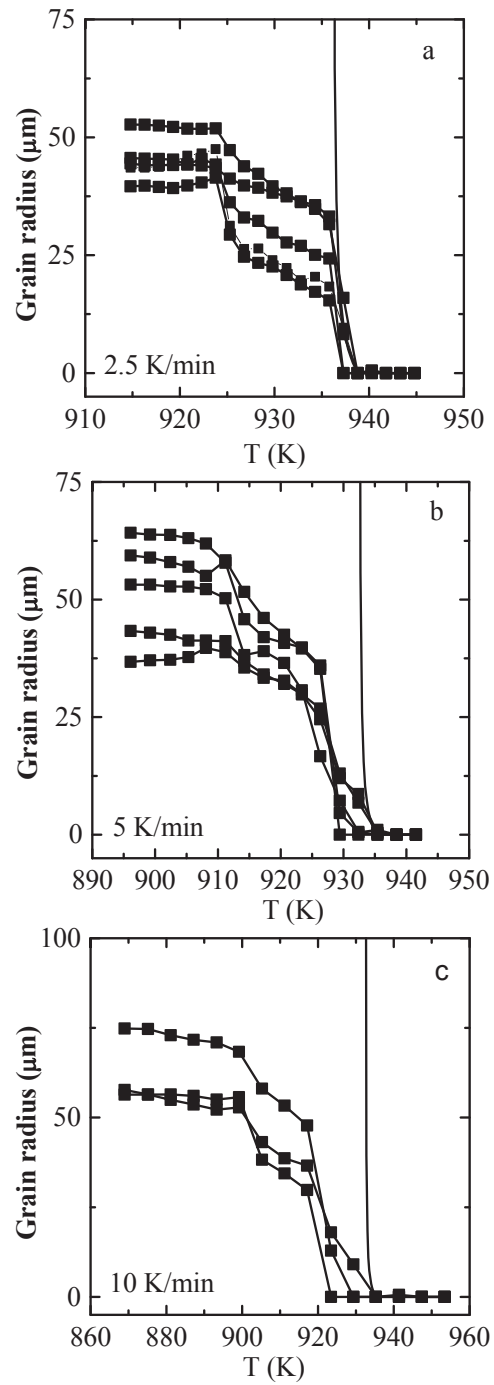


Figure 7.13 The grain radius of individual aluminum grains (■) during solidification of Al-0.1Ti-0.1TiB₂ alloy, as a function of temperature, with continuous cooling at different cooling rate (a) 2.5 K/min (b) 5 K/min and (c) 10 K/min. The solid lines indicate the model calculation for diffusion-controlled grain growth.

Summary

The aluminum alloys are, due to their relatively high strength-to-weight ratio in comparison with other structural materials, attractive candidates for critical applications like fuel-efficient vehicles or aeroplanes. All of these applications predominantly rely on the ability of aluminum alloys to form a homogenous granular structure with a relatively small grain size. A thorough understanding of the nucleation and growth of grains, which occurs during solidification of these alloys, is therefore of obvious importance.

In pure aluminum the nucleation of a new solid phase during the liquid-to-solid phase transformation is activated by a relatively large undercooling of the melt with respect to the transformation temperature. The requirement of this undercooling to activate nucleation manifests itself in a large grain size and an inhomogeneous grain morphology, in the solidified material. However, when a solid surface compatible with the lattice of the forming nucleus is present in the melt, less undercooling is needed to activate nucleation. Therefore generally a small fraction of microscopic TiB_2 particles (grain refiners) are added to aluminum alloys before solidification. It appears that without the addition of a small amount of extra solute titanium in the melt, the surface of these particles does not work as an effective nucleation site. Even then, only about 1% of the particles added to the melt nucleate grains during solidification. The remainder are of no inherent value to the final product. Contrary to that, agglomeration of these particles, can result in casting defects in the solidified material. This study provides a new insight into the nature of grain nucleation and growth during solidification of grain refined aluminum alloys and relate the microstructural features to the grain refiner efficiency.

First, the liquid-to-solid phase transformation is studied by differential thermal analysis of various aluminum alloys with and without added grain refiners. Samples with TiB_2 particles alone in pure aluminum, exhibit a crystallization behaviour that is quite similar to pure aluminum. This reflects a poor nucleation efficiency of the TiB_2 particles. A comparison of crystallization curves of all the investigated samples confirms that the critical undercooling required to activate the nucleation process is always lower for the sample containing both solute titanium and TiB_2 particles. The formation of an additional phase, which most likely corresponds to TiAl_3 , is observed upon solidification of hyperperitectic aluminum-titanium alloy containing TiB_2 particles. Due to its better lattice compatibility with solid aluminum, TiAl_3 is considered to enhance the nucleation of solid aluminum resulting in grain refinement. The close resemblance in crystallization behaviours of hyperperitectic and hypoperitectic grain refined aluminum alloys suggest the existence of same mechanism responsible for grain refinement in both compositions.

Second, the crystallization behaviour of the aluminum alloys is studied during solidification by time dependent neutron diffraction measurements. The liquid structure factor of the aluminum alloy containing solute titanium and added TiB_2 particles closely resembles that of pure aluminum. These observations show that the grain refiners have little influence on the overall short-range order in the liquid

aluminum alloy prior to the solidification process. Directly after the initiation of solidification, anomalous temporal fluctuations are observed in the Bragg-peak intensity of the solid grains during solidification of a commercial purity grain refined aluminum alloy. No such intensity fluctuations are found during solidification of pure aluminum with and without added TiB_2 particles. The possible origin of these fluctuations in the presence of alloying elements is proposed to be the interaction among the growing grains via overlapping diffusion fields. Furthermore, the grain size in pure aluminum and in a grain refined aluminum alloy is measured for different cooling rates, using small-angle neutron scattering. It is shown that the grain size decreases with increasing cooling rate and is always smaller for the grain-refined aluminum alloy compared to pure aluminum, at a given cooling rate.

Finally, the mechanism of nucleation and subsequent growth of individual grains during solidification of various grain refined aluminum alloys is further investigated in detail, using synchrotron radiation. The results indicate that prior to solidification, the formation of a metastable TiAl_3 phase is detected in the aluminum alloys containing both solute titanium and added TiB_2 particles. This TiAl_3 phase is found to appear about 10 K above the solidification temperature of aluminum. However, when the nucleation of aluminum grains starts, the TiAl_3 phase ceases to grow and dissolves with further decrease in temperature. The metastable TiAl_3 phase is not observed during cooling of aluminum alloys containing only solute titanium or added TiB_2 particles. This signifies the essential role played by the TiAl_3 phase to enhance the nucleation of aluminum grains during solidification of grain refined aluminum alloys. The metastable TiAl_3 phase is detected in two crystallographic structures: tetragonal, and cubic. As TiAl_3 has better lattice compatibility with the face-centered cubic structure of solid aluminum, compared to the hexagonal structure of TiB_2 , the TiAl_3 surface provides a better nucleation site for aluminum grains during solidification.

The results indicate that the nucleation process is always limited to the initial stage of the solidification and is complete at a solid phase fraction of about 20 % for all samples. The growth of nucleated grains leads to a significant release of latent heat, which in turn decreases the undercooling and thereby reduces the nucleation rate as the transformation proceeds. This limits the efficiency of grain refiners. The results further indicate that the growth behaviour of individual aluminum grains is predominantly controlled by the diffusion of solute titanium and the release of latent heat. The earlier stage of the grain growth is consistent with the model predictions for diffusion-controlled growth of non-interacting grains. Afterwards the grain growth is controlled by the increase in temperature caused by the release of latent heat.

The conclusion is that the solute titanium plays dual role during solidification of grain refined aluminum alloys containing both solute titanium and added TiB_2 particles. First it helps to nucleate the TiAl_3 phase on the TiB_2 surfaces, which then provides a favourable substrate for the nucleation of aluminum grains upon solidification. Second, the diffusion of solute titanium retards the grain growth and delays the release of latent heat, causing the nucleation process to continue.

Samenvatting

Aluminium legeringen zijn, vanwege hun relatief hoge sterkte-gewichts verhouding in vergelijking met andere materialen, aantrekkelijke kandidaten voor kritische toepassingen zoals brandstofzuinige voertuigen of vliegtuigen. Al deze toepassingen vertrouwen in hoge mate op het vermogen van aluminium legeringen om een homogene kristalstructuur te vormen met een relatief kleine korrelgrootte. Een diepgaand begrip van de kiemen en groeien van korrels, welke plaats vindt tijdens het stollen van deze legeringen, is daarom van evident belang.

In zuiver aluminium wordt het kiemen van een nieuwe vaste fase tijdens de faseovergang van vloeibaar naar vast vaak pas geactiveerd door een relatief grote onderkoeling van de smelt ten opzichte van de overgangstemperatuur. De noodzaak van deze onderkoeling voor het activeren van kiemvorming manifesteert zichzelf in een grote korrelgrootte en een inhomogene korrelstructuur in het gestolde materiaal. Wanneer echter een vast oppervlak aanwezig is in de smelt, welke in overeenstemming is met het rooster van de te vormen kiem, is er een lagere onderkoeling vereist om de kiemvorming te activeren. Hiertoe wordt over het algemeen voor het stollen een kleine hoeveelheid microscopisch kleine TiB_2 deeltjes (korrelverfijners) toegevoegd aan de aluminium legeringen. Gebleken is dat zonder de toevoeging van een kleine hoeveelheid extra opgelost titaan in de smelt het oppervlak van deze deeltjes niet als effectieve kiemplaats fungeren. Zelfs in dat geval blijkt slechts ongeveer 1% van aan de smelt toegevoegde deeltjes het kiemen van een korrel te veroorzaken tijdens het stollen. Het restant is niet van inherente waarde voor het eindproduct. Integendeel, agglomeratie van deze deeltjes kan resulteren in gietfouten in het gestolde materiaal. Deze studie geeft nieuw inzicht in de mechanismen van het kiemen en groeien van korrels tijdens het stollen van korrelverfijnde aluminium legeringen en geven een verband tussen de eigenschappen van de korrelstructuur en de doelmatigheid van de korrelverfijners.

Als eerste is de faseovergang van vloeibaar naar vast bestudeerd met behulp van differentiële thermische analyse aan verschillende aluminium legeringen met en zonder toegevoegde korrelverfijners. De samples met enkel TiB_2 deeltjes in zuiver aluminium vertonen een kristallisatiegedrag dat in sterke mate overeen komt met dat van zuiver aluminium. Dit is een duidelijke indicatie voor de matige kiemefficiëntie van de TiB_2 deeltjes. Een vergelijking van de kristallisatiecurves van alle bestudeerde samples bevestigt dat de kritische onderkoeling die vereist is om het kiemproces te activeren altijd lager is voor de samples die zowel opgelost titaan als TiB_2 deeltjes bevatten. De vorming van een extra fase, die naar alle waarschijnlijkheid overeen komt met $TiAl_3$, is waargenomen gedurende het stollen van hyperperitectische aluminium-titaan legeringen die TiB_2 deeltjes bevatten. Vanwege zijn betere overeenstemming met het rooster van vast aluminium, wordt verondersteld dat $TiAl_3$ het kiemen van vast aluminium bevordert, wat leidt tot korrelverfijning. De nauwe overeenstemming tussen het kristallisatiegedrag van hyperperitectische en hypoperitectische korrelverfijnde aluminium legeringen suggereert dat in beide samenstellingen hetzelfde mechanisme verantwoordelijk is voor korrelverfijning.

Als tweede is het kristallisatiegedrag van de aluminium legeringen tijdens het stollen bestudeerd met tijdsafhankelijke neutronendiffractiemetingen. De vloeistofstructuurfactor van de aluminium legering met opgelost titaan en toegevoegde TiB_2 deeltjes is in nauwe overeenstemming met die van zuiver aluminium. Deze observaties duiden erop dat de korrelverfijners een geringe invloed hebben op de gemiddelde korte-afstand ordening in vloeibare aluminium legering voorafgaand aan het stolproces. Voor een korrelverfijnde aluminium legering met een commerciële zuiverheid zijn er direct na de start van het stollen ongebruikelijke tijdsafhankelijke fluctuaties waargenomen in de intensiteit van de Bragg pieken van de vaste korrels gedurende het stollen. Zulke fluctuaties in de intensiteit zijn niet waargenomen in samples van zuiver aluminium met en zonder toegevoegde TiB_2 deeltjes. De mogelijke oorsprong van deze fluctuaties in de aanwezigheid van legeringselementen is verondersteld te liggen in de interactie tussen de groeiende korrels via de overlappende diffusievelden. Verder is de korrelgrootte in zuiver aluminium en een korrelverfijnde aluminium legering gemeten met behulp van kleine-hoek neutronenverstrooiing voor verschillende afkoelsnelheden. De korrelgrootte vertoont een afname voor toenemende afkoelsnelheden en is voor elke afkoelsnelheid kleiner in de korrelverfijnde aluminium legering dan in het zuivere aluminium.

Tenslotte is het mechanisme van het kiemen en de daaropvolgende groei van korrels tijdens het stollen van verschillende korrelverfijnde aluminium legeringen in detail bestudeerd door middel van synchrotron straling. De uitkomsten tonen aan dat voorafgaand aan het stollen de vorming van een metastabiele $TiAl_3$ is waar te nemen in de aluminium legeringen die zowel opgelost titaan en toegevoegde TiB_2 deeltjes bevatten. Deze $TiAl_3$ fase begint zich ongeveer 10 K boven de stoltemperatuur van aluminium te vormen. Wanneer het kiemen van de aluminiumkorrels echter begint, dan stopt de $TiAl_3$ fase met groeien en lost vervolgens op bij een afnemende temperatuur. De metastabiele $TiAl_3$ is niet waargenomen tijdens het koelen van de aluminium legeringen die alleen opgelost titaan of toegevoegde TiB_2 deeltjes bevatten. Dit duidt op de essentiële rol die de $TiAl_3$ fase speelt bij het bevorderen van het kiemen van aluminium korrels tijdens het stollen van korrelverfijnde aluminium legeringen. De metastabiele $TiAl_3$ fase is waargenomen met twee verschillende roosterstructuren: tetragonaal en kubisch. Aangezien de roosterstructuur van $TiAl_3$ beter overeen stemt met de vlak-gecentreerde kubische structuur van vast aluminium dan de hexagonale roosterstructuur van TiB_2 , voorziet het $TiAl_3$ oppervlak een betere kiemplaats voor aluminiumkorrels tijdens het stollen.

De resultaten laten zien dat het kiemproces in alle gevallen zich beperkt tot het beginstadium van het stollen, beëindigd is bij een volumefractie van ongeveer 20% voor alle samples. De groei van de gekiemde korrels leidt tot het vrij komen van een aanzienlijke hoeveelheid latente warmte, welke vervolgens tot een afname in de onderkoeling leidt, en daardoor een afname in de kiemsnelheid veroorzaakt gedurende een voortschrijdende transformatie. Dit beperkt de doelmatigheid van de korrelverfijners. De resultaten laten zien dat het groeigedrag van individuele aluminiumkorrels voornamelijk wordt gecontroleerd door de diffusie van opgelost titaan en het vrijkomen van latente warmte. Het vroegste stadium van de korrelgroei is in overeenstemming met de modelvoorspellingen voor diffusiegecontroleerde groei van onafhankelijke korrels. Daarna wordt de korrelgroei bepaald door de toename in temperatuur veroorzaakt door het vrij komen van latente warmte.

Geconcludeerd kan worden dat het opgeloste titaan een dubbele rol speelt tijdens het stollen van korrelverfijnde aluminium legeringen die zowel opgelost titaan als toegevoegde TiB_2 deeltjes bevatten. Allereerst helpt het de $TiAl_3$ fase te vormen

op de TiB_2 oppervlakken, welke dan een gunstige ondergrond vormt voor het kiemen van aluminium korrels gedurende het stollen. Ten tweede vertraagt de diffusie van opgelost titaan de korrelgroei, waardoor het vrijkomen van latente warmte wordt uitgesteld en het kiemproces langer kan voortduren.

Acknowledgements

It is almost four and half years that I have spent in the group of Neutron Scattering and Mössbauer Spectroscopy (later named Fundamental Aspects of Materials and Energy), working on the research presented in this thesis. I would like to say that, working in this group was always pleasant and stimulating. I am indebted to many colleagues and friends for their contributions and would like to take this opportunity to thank specially those who have played a significant role in helping me to bring this work to fruition.

First I would like to thank God, who gave me sufficient energy and courage to carry out this research and complete this thesis.

It was a privilege to complete this work under the guidance of my promoters Gordon Kearley and Laurens Katgerman. For me it is difficult to envisage the contents of this thesis without their contributions and advice. I am thankful to them for sharing their knowledge, experience and wisdom, with me.

I would like to express my gratitude to Niels van Dijk, my daily advisor, for his continuous assistance, constructive critics and patience. Special thanks for his help in performing all the experiments using neutrons and X-rays, and to interpret the results, that has played a key role in the success of this research. Without his persistent support and encouragement, this thesis would not have existed.

I owe much gratitude to Peter Verkerk (Late) who proposed this research project and provided me opportunity to work on it, and Wouter Montfrooij who helped me at the start of this project and with the neutron experiments at Studsvik.

I am grateful to Erik Offerman for nice discussions and his help during the 3D XRD experiment. Thanks to Vincent Verhoeven for his contribution, specially developing software for the temperature controller. Further thanks to Piet vander Ende, whose support in the workshop was essential for the fabrication of sample containers and high temperature furnace insert.

The work in this thesis has also greatly benefited from several international collaborations. I am thankful to Robert McGreevy, for providing an opportunity to perform neutron diffraction experiments at Studsvik Neutron Research Laboratory. At the Institute Laue-Langevin in particular I want to thank Thomas Hansen for his assistance with the neutron diffraction experiments on D20, and Charles Dewhurst, for his assistance with the SANS experiments on D11. It has been a great pleasure working with them. The neutron diffraction and small angle neutron scattering measurements we did together form an important part (chapter 6) of this thesis. Another important collaborator was Mona Moret, at beam line ID11 of European Synchrotron Radiation Facility who helped us to perform our 3D XRD experiment, successfully. I would like to thank Nico Geerlofs for his support during the DTA measurements and Lie Zhao for his help regarding thermodynamic calculations using MTDATA. Many thanks to Y. Huang, from the University of Amsterdam, for assistance with the sample preparation.

Further I like to mention Robert, Tim, Lambert, Serdar, Gijs, Alexander, Jerome, Olga, Jeroen, Julia, Iulian, Marnix, and all the other people in Neutron

Scattering and Mössbauer Spectroscopy group who created a nice working atmosphere. Especially, I cannot forget to thank Marianne, who was always willing to help.

I am thankful to Atif, Tariq, Aqib, Tahir, Zeeshan, Shabir, Haroon, Khurram, Majid, Guus, Silvia, Sabine, Tom, George and all my other friends who enriched my spare time during my stay in Delft. Finally I could not imagine to have succeeded without the moral support of my family.

Curriculum Vitae

Naveed Iqbal was born in Faisalabad (Pakistan) on the 25th of April, 1974. He completed his under graduation at the “University of Punjab” in Lahore, where he obtained his BSc-degree in 1994. In the same year he started his study in physics at the Quaid-I-Azam university, in Islamabad, where he completed his MSc in physics in 1996. The same year, he was offered a fellowship by the “Centre for Nuclear Studies”, at the Quaid-I-Azam University, where he obtained his MSc in Nuclear Engineering in 1998. From October 1998 to September 2000, he worked as a research scientist in the Pakistan Institute of Nuclear Science and Technology in Islamabad.

From October 2000 to June 2005, he was a PhD student in the department of Neutron Scattering and Mössbauer Spectroscopy at the Interfaculty Reactor Institute of the Delft University of Technology. In this group he performed an experimental study of grain nucleation and growth kinetics during the liquid to solid phase transformation of aluminum alloys, under the supervision of Prof. dr. G. J. Kearley, Prof. ir. L. Katgerman and Dr. ir. N. H. van Dijk.

List of publications

- “Differential thermal analysis measurements on aluminum alloys for the investigation of the crystallization kinetics during grain refinement”, N. Iqbal, N. H. van Dijk, L. Katgerman, and G. J. Kearley. (*in preparation*).
- “Real-time observation of grain nucleation and growth during solidification of metals”. N. Iqbal, N. H. van Dijk, S. E. Offerman, M. P. Moret, L. Katgerman, and G. J. Kearley, *Acta Mater.* (Article in press).
- “Microscopic View on Grain Nucleation and Growth Kinetics During Solidification of Aluminum Alloys”, N. Iqbal, N. H. van Dijk, S. E. Offerman, M. P. Moret, L. Katgerman, and G. J. Kearley, *Mater. Res. Soc. Symp. Proc. (Boston, USA), Vol.840* (2005) Q7.12.
- “Nucleation kinetics during solidification of aluminum alloys”. N. Iqbal, N. H. van Dijk, S. E. Offerman, M. P. Moret, L. Katgerman, and G. J. Kearley, *J. of non crystalline solids*. (Article submitted).
- “The effect of solute Titanium and TiB_2 particles during liquid to solid phase transformation in aluminum alloys during solidification”. N. Iqbal, N. H. van Dijk, T. Hansen, L. Katgerman, and G. J. Kearley, *Materials Science and Eng. A*, 386 (2004) 20.
- “SANS investigations of grain growth in aluminum alloys during solidification”, N. Iqbal, N. H. van Dijk, C. Dewhurst, L. Katgerman, and G. J. Kearley. *Physica B*. 350 (2004) e1011.
- “Periodic structural fluctuations in aluminum alloys during solidification”, N. Iqbal, N. H. van Dijk, T. Hansen, L. Katgerman, and G. J. Kearley. *Materials Science and Eng. A* 367 (2004) 82.
- “Ordering kinetics in aluminum alloys during solidification”, N. Iqbal, N. H. van Dijk, V. W. J. Verhoeven, T. Hansen, W. Montfrooij, L. Katgerman, and G. J. Kearley, *Acta Mater.* 51 (2003) 4497
- “Structure and dynamics of liquid aluminum alloys during solidification”, N. Iqbal, N. H. van Dijk, V. W. J. Verhoeven, T. Hansen, L. Katgerman and G. J. Kearley, *Proc. 6th Int. ESAFORM Conf. On Material Forming, Salerno, Italy*. European Scientific Association for Material Forming, Nuova Ipsa Editore, Apr. 2003, p. 411.

